4342

MODELING AND OPTIMIZATION OF

BUBBLE MEMORY CIRCUITS

MODELING AND OPTIMIZATION

OF

BUBBLE MEMORY FIELD ACCESS PROPAGATION CIRCUITS

by

WAGUIH S. ISHAK, B.Sc.E.E., B.Sc.Math., M.Eng.

A Thesis

Submitted to the Faculty of Graduate Studies

in Partial Fulfilment of the Requirements

for the Degree

Doctor of Philosophy

McMaster University

April 1978

DOCTOR OF PHILOSOPHY (1978)
(Electrical Engineering)

McMASTER UNIVERSITY
Hamilton, Ontario

TITLE: MODELING AND OPTIMIZATION OF BUBBLE MEMORY FIELD ACCESS PROPAGATION CIRCUITS

AUTHOR: Waguih Shafik Ishak, B.Sc.(E.E.) (Cairo University)
B.Sc.(Math.) (Ain-Shams University)
M.Eng. (McMaster University)

SUPERVISOR: Professor Edward Della Torre

NUMBER OF PAGES: xiii, 153

ABSTRACT

The work presented in this thesis relates to one of the most important problems in the design of high-density, high-speed bubble memory systems. A new approach for the analysis, design and optimization of bubble circuits is developed. This formulation is suited to computer-aided methods of solution.

A micromagnetic approach to the modeling of permalloy bubble circuits is examined. Basic to the approach is the discretization of the circuit into very small regions to simulate the ferromagnetic essence of the permalloy. This method of analysis is very useful in studying submicron bubble circuits. However, the numerical difficulties as well as the excessive computer time required for such analysis led to careful consideration of possible approximations. A continuum model for analyzing field access bubble circuits has, thus, been developed and used to characterize arbitrary shaped permalloy structures. Various propagation circuits, including gap tolerant circuits, and bubble replicators are analyzed and the results compared to experimentally available data.

A model for studying bubble size and position fluctuations is introduced. The model assumes that the bubble domain is circular. However, with slight modifications it can accept general elliptical shapes. For various propagation circuits, the model results are in excellent agreement with experimental measurements in the literature.

An algorithm for bubble circuit optimization is developed and discussed in detail. The problem is formulated as a constrained minimax objective which is suited to nonlinear programming methods of solution. Typical examples of T-I propagation circuits are furnished to illustrate the approach.

ACKNOWLEDGEMENTS

I would like to express my sincere appreciation to my supervisor Dr. E. Della Torre. His expertise in the area of bubble memories was invaluable in the development of this work. Special thanks are due to Dr. W. Kinsner for his expert guidance, discussions and encouragement. I would also like to thank Dr. D. Thompson for his continuing interest in the work.

Special thanks are also due to Dr. C. Hegedüs and Mr. T. Blake for stimulating discussions. The interest and continual encouragement of Dr. C.K. Campbell is greatefully acknowledged. I am very grateful to Drs. J.W. Bandler and H.L. Abdel-Malek for stimulating discussions and helpful advice in the optimization problem.

Appreciation is expressed to the National Research Council of Canada and McMaster University for financial support.

The competence and reliability of Miss Pat Dillon, of the Word Processing Center, who typed this thesis and did countless corrections, is very much appreciated. Thanks are also due to Mr. G. Kappel for his excellent drawings.

TABLE OF CONTENTS

CHAPTER			PAGE
1	INTRODUCTION		1
2	MAGNETIC BUBBLES, BUBBLE CIRCUITS AND CIRCUIT MODELING: A REVIEW		6
	2.1	Introduction	6
	2.2	Bubble Domains	7
	2.3	Bubble Materials	7
	2.4	Bubble Circuits	10
		2.4.1 Bubble Generation	11
		2.4.2 Bubble Detection	11
		2.4.3 Bubble Annihilation	14
		2.4.4 Bubble Replication	14
		2.4.5 Bubble Propagation	15
	2.5	The Modeling Problem	18
	2.6	Micromagnetic Models	19
	2.7	Domain Models	21
	2.8	Continuum Models	23
	2.9	Analytical Models	25
	2.10	Conclusions	26
3	NEW APPROACHES TO BUBBLE CIRCUIT MODELING		27
	3.1	Introduction	27
	3.2	Statement of the Problem	27
	3.3	Energy Analysis	30
	3.4	A Micromagnetic Model	33

TABLE OF CONTENTS (continued)

CHAPTER			PAGE
3	NEW APPROACHES TO BUBBLE CIRCUIT MODELING (continued)		
		3.4.1 Computation of the Applied Field	36
		3.4.2 Computation of the Demagnetizing Field	40
		3.4.3 Computation of the Exchange Field	42
		3.4.4 The Micromagnetic Algorithm	43
		3.4.5 Discussion	44
	3.5	A Continuum Model	46
		3.5.1 Introduction	46
		3.5.2 The Magnetization Algorithm	50
		3.5.3 Discussion	52
	3.6	Examples	54
	3.7	Conclusions	65
4	ANALYSIS OF PROPAGATION CIRCUITS AND BUBBLE SIZE FLUCTUATIONS		66
	4.1	Introduction	66
	4.2	The Potential Well	67
	4.3	Analysis of Bubble Circuits	68
		4.3.1 Rectangular Bars	68
		4.3.2 Chevron Circuits	74
		4.3.3 Half-Disk Circuits	77
		4.3.4 Bubble Replicators	83
	4.4	Bubble Size Fluctuations	83
	4.5	The Bubble Size Fluctuation Algorithm	88
		4.5.1 Introduction	88
		4.5.2 Computation of the Collapse and Run-out Fields	89
		4.5.3 Computation of the New Bubble Diameter	93
	4.6	Examples	95
	4.7	Conclusions	99

TABLE OF CONTENTS (continued)

CHAPTER		PAGE
5	BUBBLE CIRCUIT OPTIMIZATION	100
	5.1 Introduction	100
	5.2 Qualitative Analysis	101
	5.3 Circuit Parameters	102
	5.4 The Optimization Problem	105
	5.5 Approximation and Method of Solution	106
	5.6 Examples	110
	5.6.1 Spacer Effect	110
	5.6.2 Bubble Height Effect	112
	5.7 Discussion	113
	5.8 Conclusions	115
6	CONCLUSIONS	117
APPENDIX		
A	RELATIONSHIPS BETWEEN SI AND CGS UNITS	120
B	COMPUTATION OF THE DEMAGNETIZING FACTORS	121
C	THE EXCHANGE ENERGY	128
D	M-H APPROXIMATIONS	132
REFERENCES		138
AUTHOR INDEX		144
SUBJECT INDEX		148

LIST OF FIGURES

FIGURE		PAGE
2.1	A cylindrical bubble domain in a uniaxial thin film. The bubble is stabilized by the external bias field.	8
2.2	Bubble circuits: (a) a nucleate generator (Nelson, Chen and Geusic 1973), (b) a magnetoresistive detector (Strauss 1971), (c) an MP detector (Ishak, Kinsner, and Della Torre 1975) and (d) a bubble replicator (Bobeck, Bonyhard and Geusic 1975).	12
2.3	Bubble domains attracted to the ends of permalloy overlays and underlays by an in-plane field H_T.	16
2.4	Bubble propagation circuits: (a) T-I circuit (Perneski 1969), (b) Y-I circuit (Danylchuk 1971) and (c) asymmetric half-disk circuit (Bonyhard and Smith 1976).	17
2.5	A magnetic body (a) in the demagnetized state responds to an applied field H_A by (b) a domain wall motion where the domains whose magnetization are closest to H_A grow at the expense of the other domains until (c) the whole body becomes a single domain and then (d) a magnetization rotation occurs to make M_s parallel to H_A.	20
2.6	Domains and domain walls in rectangular permalloy bars. (a) two longitudinal domains per bar (Della Torre and Kinsner 1973) and (b) a closure domain configuration (Khaiyer 1976).	22
3.1	A rectangular permalloy bar of dimensions $\ell \times w \times t$ in the x-y plane. The z-axis is perpendicular to the bar plane. The applied field and magnetization at point P, whose position vector is $\underset{\sim}{r}_P$, are $\underset{\sim}{H}_A(\underset{\sim}{r}_P)$ and $\underset{\sim}{M}(\underset{\sim}{r}_P)$, respectively.	29
3.2	A discretization mesh of N points placed over a permalloy bar in the x-y plane. (a) the cell dimensions are Δx and Δy and (b) at point i, the total local field $\underset{\sim}{H}_L(\underset{\sim}{r}_i)$ is inclined at an angle $\theta_L(\underset{\sim}{r}_i)$ to the x-axis.	37
3.3	The coordinate system used to compute the radial component of the bubble's stray field at a point P(r,z).	39

FIGURE		PAGE
3.4	The coordinate system used to compute the demagnetizing field at a field point i due to the magnetization at a source point j.	41
3.5	Effect of the under-relaxation factor on the number of iterations required in the magnetization algorithm.	53
3.6	Demagnetizing factor distributions of a rectangular permalloy bar of dimensions 15 x 3 x 0.4 μm (shown in the inset). Solid lines refer to cubic spline interpolation (see (3.46) and (3.47)) and dashed lines to linear interpolation (George and Hughes 1976a).	55
3.7	The magnetization distributions in a rectangular permalloy bar of dimensions 7.5 x 1.5 x 0.3 μm: (a) x-component of the magnetization as a function of H_T, (b) x-component as a function of y and the demagnetizing factors and (c) y-component of the magnetization as a function of y.	56
3.8	Effect of the bubble position on the magnetization distribution along the center line of a rectangular permalloy bar of dimensions 7.5 x 1.5 x 0.3 μm. The maximum magnetization occurs at the bubble perimeter.	58
3.9	The x-component of the demagnetizing field and the magnetization distribution along the center line of a rectangular permalloy bar of dimensions 7.5 x 1.5 x 0.3 μm (a) for two bubble positions and (b) y-component of the magnetization as a function of y.	59
3.10	Comparison between the results of the magnetization algorithm and the results of models of other workers.	60
3.11	The demagnetizing factor distribution at five different cross-sections in a symmetric half-disk (see the inset).	62
3.12	The y-component of the demagnetizing field and the magnetization distribution at two different cross-sections in two periods of asymmetric half-disk circuit in the presence of a bubble and an in-plane field.	63
4.1	The potential well distribution along the center line of a rectangular permalloy bar of dimensions 7.5 x 1.5 x 0.3 μm for two different in-plane field values in the positive x-directions.	69

LIST OF FIGURES (continued)

FIGURE		PAGE
4.2	Comparison between the results of the present model and the results of George and Hughes (1976b) for a rectangular permalloy bar of dimensions 15 x 3 x 0.4 μm.	71
4.3	Two-dimensional potential well profile for a rectangular permalloy bar of dimensions 15 x 3 x 0.4 μm. The contours labelled P and E correspond to H_z = -800 A/m and 0 A/m, respectively.	72
4.4	Effect of bubble diameter on the potential well depth along the center line of a rectangular permalloy bar of dimensions 7.5 x 1.5 x 0.3 μm.	73
4.5	The potential well profile along the bubble path in a 90^{o} symmetric chevron for six in-plane orientations. The bubble hardly moves from point 1 (see the inset) to point 2 until $\theta > 60^{o}$.	75
4.6	The potential well profile along the bubble path in a 90^{o} asymmetric chevron for seven in-plane field orientations. The potential well gradients for $0 < \theta < 90^{o}$ are larger than those of Fig. 4.5.	76
4.7	Two-dimensional potential well profile for a symmetric half-disk of 14 μm period and 2 μm gap. The points M refer to the location of the minimum potential well depth, where the center of a bubble (d = 2 μm, h = 3 μm) will be located.	78
4.8	Two-dimensional potential well profile for an asymmetric half-disk circuit of 14 μm period and 2 μm gap. The points M refer to the minimum potential well depth, where the center of a bubble (d = 2 μm, h = 3 μm) will be located.	79
4.9	The potential well profile along the bubble path in a two period symmetric half-disk circuit (see the inset) for four in-plane field orientations. The bubble stretches across the gap when H_T is in the negative y-direction.	81
4.10	The potential well profile along the bubble path in a two period symmetric half-disk circuit (see the inset) for four in-plane field orientations. The well depth across the gap is smoother than that in Fig. 4.9.	82

LIST OF FIGURES (continued)

FIGURE		PAGE
4.11	"Sideways" replicator (Bonyhard, Chen and Smith 1976). The bubble stretches under the copper loop and is split into two bubbles when I is applied. One bubble goes back to the minor loop and the other to the major loop.	84
4.12	The potential well distribution in a "sideways" replicator for two in-plane field orientations.	85
4.13	The radial stability function $S_o(a)$ as a function of the bubble's aspect ratio (Thiele 1969). The points A, B and C illustrate the steps of the inverse bubble function algorithm of Subsection 4.5.2.	92
4.14	The T-I propagation circuit used by Kryder, Ahn and Powers (1975) to propagate 2 μm diameter bubbles in amorphous films.	96
4.15	Comparison between the results of the bubble size fluctuation algorithm and the experimental data of Jones and Enoch (1974).	98
5.1	A typical T-I propagation circuit. X refers to the bubble path. Permalloy, bubble and external parameters are shown.	103
5.2	Optimized potential well profiles for the T-I circuit of Fig. 4.14.	114
B.1	Various kinds of singularities that appear in the computation of the demagnetizing field: (a) interior, (b) 90^o corner, (c) 270^o corner, (d) x-edge and (e) y-edge singularities. Region S is singular and N is nonsingular.	125
B.2	The discretization mesh used to compute the contribution of a singular corner point to the demagnetizing field.	126
C.1	A (a) unit vector inclined at angle θ to the x-axis and (b) a mesh of points centered around point (m, n).	130
D.1	The M-H_A and the M-H_L relations. When OD and OA are sheared to the left by an amount sufficient to make OD vertical, OA will then give the M-H_L relation.	133
D.2	Linear-arctan and parabolic-arctan M-H_L approximations.	135
D.3	Approximating arctan (x) by a simpler function.	136

LIST OF TABLES

TABLE		PAGE
3.1	Comparison between the computer time and memory requirements for the present model and the model of George and Hughes (1976a).	64
4.1	Results of the bubble size fluctuation algorithm for the T-I propagation circuit of Fig. 4.14.	97
5.1	Factors affecting the upper and the lower bounds on the parameters of Fig. 5.1.	104
5.2	Comparison between the actual potential well depth and the quadratic polynomial approximation for the circuit of Fig. 4.14.	108
5.3(a)	Results of the optimization procedure for the T-I circuit of Fig. 4.14 (spacer effect).	111
5.3(b)	Results of the optimization procedure for the T-I circuit of Fig. 4.14 (bubble height effect).	112
5.4	Minimum in-plane propagation field for the T-I circuit of Fig. 4.14.	115
A.1	Relationships between SI and CGS units.	120

CHAPTER 1

INTRODUCTION

The problem of modeling and analysis of magnetic bubble field access devices and, in particular, circuits used for bubble propagation is the subject of this thesis. A secondary objective is to introduce a new optimization procedure for the design of bubble propagation circuits.

For the reader who is unfamiliar with these circuits, Chapter 2 presents a brief review of magnetic bubbles, bubble materials and bubble circuits. The definition of the problem of propagation circuit modeling is introduced. Micromagnetic modeling, domain modeling and continuum modeling techniques are discussed and a unified review of the existing models is also given.

One of the basic functions necessary for the operation of a serially accessed bubble memory system is the ability to manipulate the stored data. This is done by moving the bits of information (the presence or absence of bubbles), along certain propagation tracks within the memory. Since bubble domains are stabilized by an external fixed bias field, it is possible to move them by introducing a traveling local perturbation of the bias field, that is a traveling potential well. It is the role of the bubble propagation circuits to provide such perturbations. The use of permalloy features magnetized by a rotating transverse magnetic field has thus far proven to be the most reliable propagation method. Propagation structures built of permalloy are called field access circuits.

To date, the design of field access propagation circuits for bubble memory and logic applications (Smith 1974, O'Dell 1974, Bobeck and Della Torre 1975 and Chang 1975) has largely been a cut-and-try process, relying almost exclusively on intuition and experience. The questions of which factors determine the minimum rotating field required for propagation, the value of this minimum field and the optimum permalloy geometry for an operating device have not been adequately answered.

At present, when designing a means for propagating bubbles, one is faced with a large number of different circuits. Within just the framework of field access circuits there are still a bewilderingly large number of different circuits, such as: T-I (Perneski 1969), Y-I (Danylchuk 1971), Chevrons (Bobeck, Fischer and Smith 1972), X-I (Parzefall, Littwin and Metzdorf 1973), parallel-bars (Della Torre and Kinsner 1973), channel-bars (Della Torre and Kinsner 1975), half-disks (Bonyhard and Smith 1976 and Gergis, George and Kobayashi 1976) and asymmetric chevrons (Bobeck and Danylchuk 1977), to name a few.

The important characteristics for a good propagation structure are: good margins, compatibility with the design of other functions in the memory system and the capability of propagating bubbles at high speed. The bias field margin (the range of bias field over which the bubble does not strip-out or collapse) depends on the rotating propagation field amplitude, the permalloy shape and the bubble domain parameters (diameter, height and saturation magnetization). Since along the propagation track (bubble path) the bias field margin varies from point to point, the overall circuit margin is determined by the smallest bias field margin. The smallest bias field margin occurs at critical points in the propagation circuits such as the gaps between the T and the I elements in T-I circuits and along the arms of the Y elements in Y-I circuits. Therefore, a good design of a propagation circuit should guarantee that the bubble will move reliably past critical points, that is the margins are adequate at these points.

In order to be able to optimize field access structures, an efficient and accurate model for analysis of arbitrary permalloy shapes, under the influence of general applied fields, is required. This model should be capable of analyzing the higher density bubble memory systems that are increasingly being used.

The work presented in this thesis includes new approaches for modeling of field access bubble circuits and, particularly, bubble propagation circuits. Moreover, it provides a novel procedure for optimization of propagation structures. In particular, Chapter 3 presents new micromagnetic and continuum models for the analysis of bubble propagation circuits. These models are general enough to be applied to arbitrary shapes of permalloy overlays. Comparison to results of other models is also given.

The analysis of Chapter 3 is used to study the propagation characteristics of various bubble propagating circuits and the results of this analysis are presented in Chapter 4. The potential well distribution of rectangular bars, symmetric and asymmetric half-disks and asymmetric chevrons are given in Chapter 4. In addition, a new algorithm for the analysis of bubble size fluctuations in propagation circuits is developed where an iterative technique is used to compute the stable bubble-permalloy configuration. This is essential for studying the dynamics of bubble circuits. Comparison to experimentally available data (Jones and Enoch 1974) is also included.

A novel procedure for propagation circuit optimization is given in Chapter 5. A discussion of the effect of circuit parameters on the circuit behavior is included. The potential well produced by the permalloy is modeled using a quadratic polynomial approximation technique (Abdel-Malek 1977). The optimization problem is, then, formulated and solved (Bandler and Sinha 1977). A typical T-I propagating circuit is analyzed using this procedure and the results are compared to experimental data (Kryder, Ahn and Powers 1975).

Appendices are included to supplement the text with specific material. These include a summary for conversion between RMKS and CGS units, the computation of the demagnetizing factors of permalloy circuits, the computation of exchange energy and a summary of useful M-H approximations.

The following are the original contributions claimed for this work:

(1) The formulation of a new micromagnetic model for the study of submicron bubble circuits.

(2) The formulation and implementation of a continuum model for

analysis of arbitrary shaped field access bubble propagation circuits in which the permalloy nonlinear characteristics are included.

(3) The analysis of gap tolerant propagation structures and replicate/transfer gates.

(4) An improved algorithm for studying the stability of bubble domains in uniaxial magnetic materials.

(5) An algorithm for computing the fluctuations in bubble size and bubble center position.

(6) The formulation of a novel algorithm for bubble circuit optimization.

CHAPTER 2

MAGNETIC BUBBLES, BUBBLE CIRCUITS AND CIRCUIT MODELING: A REVIEW

2.1 Introduction

It has now been a decade since the first paper on device applications of magnetic bubbles appeared in a technical journal (Bobeck 1967). Advances in bubble physics, devices, materials and memory systems in that decade have been impressive. Storage in bubble memories is nonvolatile and requires no stand-by power. The insensitivity of this solid-state memory to shock, vibration and radiation makes it very attractive for applications in which the memory is subject to severe operating conditions (Chang 1975).

To date, the design of bubble domain field access bubble circuits is performed by fabricating a device and testing it. If it does not perform adequately, a small change is made in the design and it is refabricated. The process is repeated until satisfactory performance is achieved. This approach is time consuming and expensive. It is desirable, therefore, to develop a model which accurately characterizes and analyzes bubble circuits and which can be used for the design of these circuits.

This Chapter gives a brief review of bubble domain materials and circuits. A review of the main approaches for modeling of field access bubble circuits is also presented. Several books (Smith 1974, O'Dell 1974, Bobeck and Della Torre 1975 and Chang 1975) provide supplemental reading for the interested reader.

2.2 Bubble Domains

Figure 2.1 shows the configuration of a bubble domain in a thin magnetic film. It is a cylindrical region in a platelet (thin film) with magnetization perpendicular to the film plane and opposite to that in the surrounding region. This configuration can be achieved only if the bubble supporting film possesses certain magnetic properties such as: uniaxial magnetic anisotropy, to orient the magnetization perpendicular to the film plane, and magnetization sufficiently small, to prevent the demagnetizing field from forcing the magnetization into the film plane. See Bobeck and Della Torre (1975) and Chang (1975). A bias field must be applied antiparallel to the bubble magnetization to prevent the bubble from running into a serpentine domain.

2.3 Bubble Materials

Successful design of high-density, high-speed bubble devices depends on the availability of a material capable of supporting sufficiently small and highly mobile domains. The storage density, data rate, stability and temperature sensitivity of bubble devices are determined by the materials parameters. These parameters and their units are:

h; material thickness (m),

M_B; material saturation magnetization (A/m),

K_u; uniaxial anisotropy constant (J/m^3),

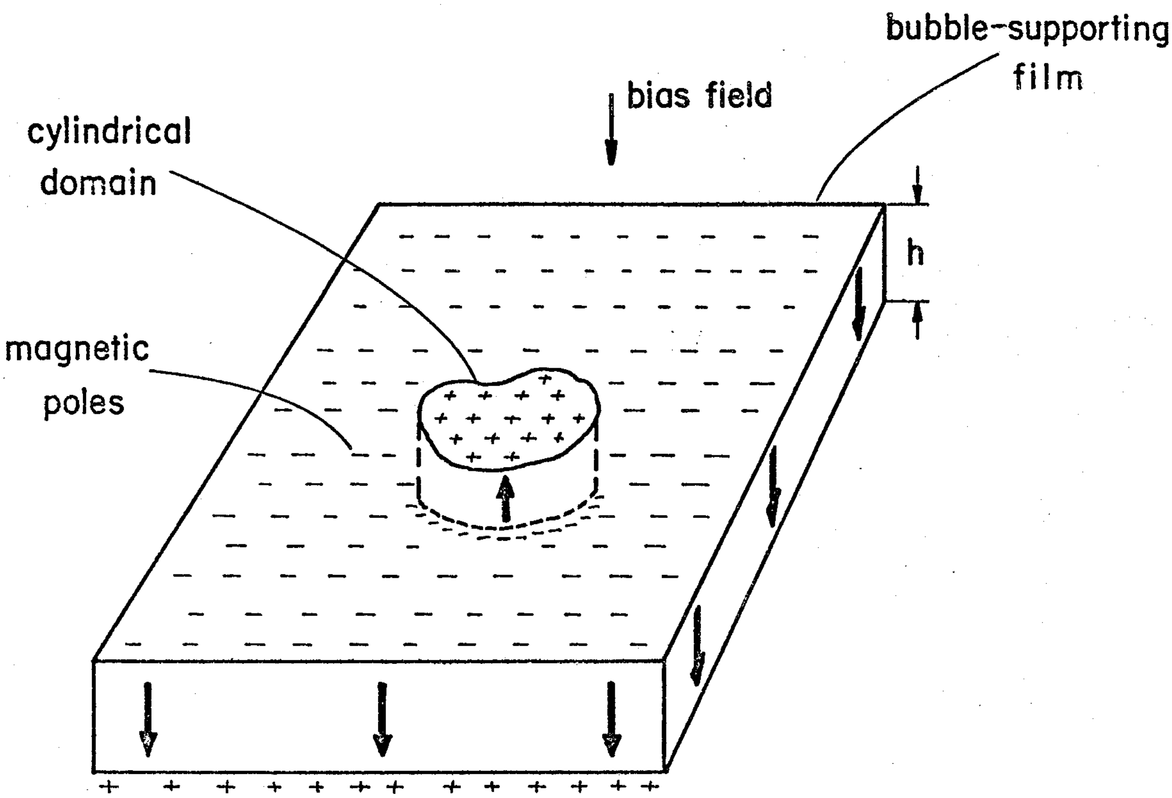

Figure 2.1 A cylindrical bubble domain in a uniaxial thin film. The bubble is stabilized by the external bias field.

A_{ex}; exchange constant (J/m) and

μ_w; domain wall mobility (m^2/A s).

A material characteristic length

$$\ell_m = \frac{4\sqrt{A_{ex}\ K_u}}{\mu_o\ M_B^2} \tag{2.1}$$

conveniently characterizes materials as to the range of bubble domain sizes they can support. According to Thiele (1969), the optimum film thickness

$$h = 4\ \ell_m \tag{2.2}$$

results in the smallest stable domain diameter

$$d = 8\ \ell_m \tag{2.3}$$

at a bias field

$$H_B \simeq 0.3\ M_B. \tag{2.4}$$

The quality factor

$$Q = \frac{2K_u}{\mu_o\ M_B^2}\ , \tag{2.5}$$

where μ_o is the permeability of free space, is a measure of the stiffness of the magnetization. Experience has shown that for most useful bubble materials, Q should be in the range of 3 to 10 (Bobeck, Bonyhard and Geusic 1975). The material parameters h, M_B, K_u, A_{ex}, and μ_w can be adjusted by tailoring the material composition.

At present, the best materials available are single-crystal garnet films in the form: $(X)_3\ Fe_5\ O_{12}$ where X is a combination of rare earths or Yttrium. The bubble size can be adjusted by varying the magnetization of the garnet. This is achieved by using solid solutions instead of one rare earth and by substitution of nonmagnetic ions (Ga or $A\ell$) into the iron ions (Nielsen 1971). Garnet films are grown by liquid-phase epitaxy (LPE) techniques on nonmagnetic substrates such as gadolinium gallium garnet (GGG). This process is described in detail by Blank and Nielsen (1972). For example, a 3 μm thick garnet ($Sm_{0.4}$ $Y_{2.6}$ $Fe_{3.8}$ $Ga_{1.2}$ O_{12}) on a substrate (Gd_3 Ga_5 O_{12}) can support 3 μm diameter bubbles yielding a storage density of 0.6×10^{10} bits/m^2 (with four bubble diameters separation). To achieve a data rate of 0.1 M bit/s, the 3 μm bubbles must have a mobility of at least 0.016 m^2/A s.

Other bubble materials are under consideration. The most promising of these are the amorphous magnetic films (Chaudhari, Cuomo and Gambino 1973). These films (typically GdCoMo) are made by low-temperature sputtering processes on noncrystalline substrates and are capable of supporting submicron diameter bubbles.

2.4 Bubble Circuits

Storage of binary information in a bubble memory system can be achieved by various methods such as: presence or absence of a bubble at a given site or by two different domain wall configurations (bubble lattice file). A memory system must have not only the ability to store information, but also provide access capability for reading and writing at a selected storage location. Therefore, in a memory system one must be able to perform the following functions: introduce new data (generate bubbles), read data (detect bubbles), remove data (annihilate bubbles) and access data (propagate bubbles). In some cases, it is advantageous to detect replicas rather than the original of the stored data and hence a fifth function, namely bubble replication, is useful (Bobeck and Della Torre 1975).

2.4.1 Bubble Generation

In the early days of bubble technology, bubble generation was accomplished primarily by replication of a bubble from a rotating seed bubble attached to a permalloy circular disk (Perneski 1969). Such disk generators have the disadvantage of requiring initialization (creation of the seed bubble). The most commonly used method of bubble generation is based on nucleate generators (Nelson, Chen and Geusic 1973). In this method a hairpin conductor loop is pulsed with an adequate current pulse to produce a bubble domain. See Fig. 2.2(a). This bubble is then propagated away, and if so desired, another bubble may be generated on the next propagate cycle. Excellent operating margins and low generating currents are obtained by locally annealing the bubble material just under the hairpin conductor loop.

2.4.2 Bubble Detection

Nondestructive readout (NDRO) of a single bubble domain can be achieved through the use of Hall-effect detectors (Strauss and Smith 1970). The vertical component of the bubble's stray field produces a Lorentz force in an adjacent semiconductor thin film, which causes a

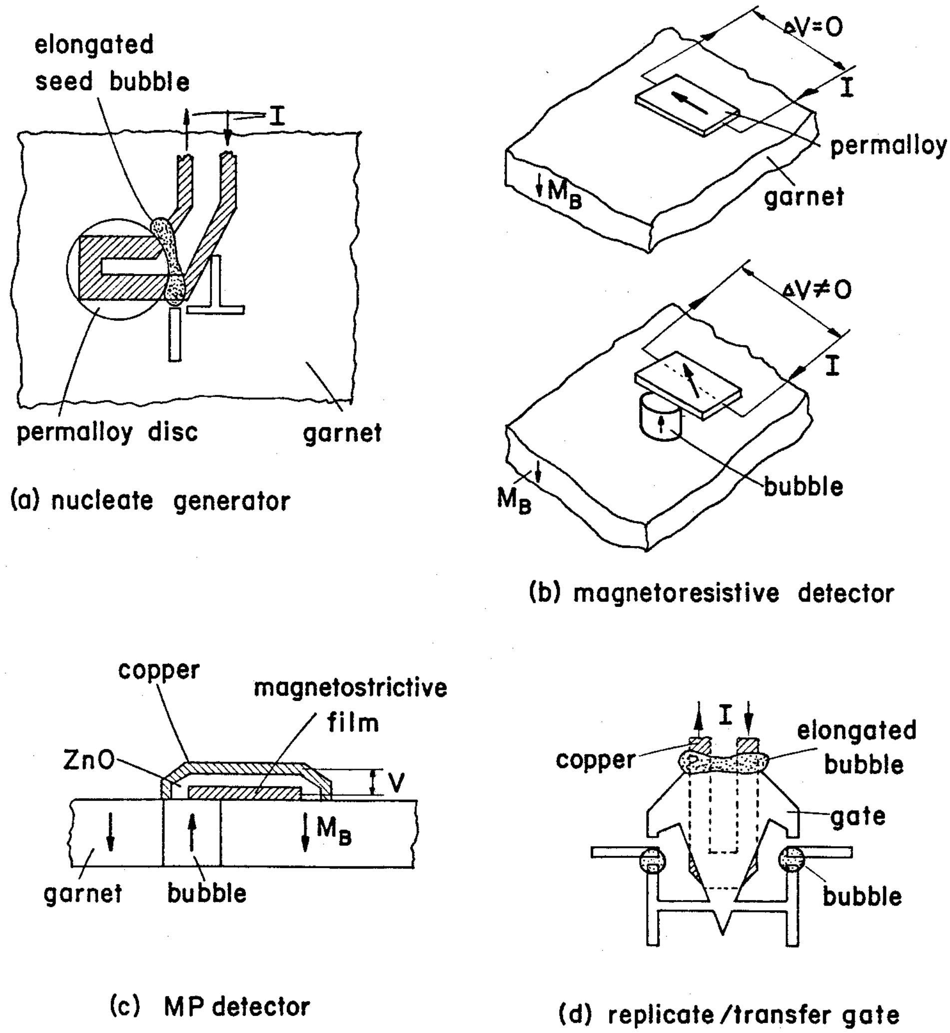

Figure 2.2 Bubble circuits: (a) a nucleate generator (Nelson, Chen and Geusic 1973), (b) a magnetoresistive detector (Strauss 1971), (c) an MP detector (Ishak, Kinsner, and Della Torre 1975) and (d) a bubble replicator (Bobeck, Bonyhard and Geusic 1975).

voltage to appear at right angles to both the bubble field and the current direction in the semiconductor. The main disadvantage of this method of detection is the requirement of an external power supply to produce the necessary current in the semiconductor film.

Magnetoresistive detection is based on the fact that the resistance of a permalloy bar changes when subject to an external magnetic field (e.g. from an adjacent bubble). This change in resistance will result in a detectable voltage change at the permalloy terminals (Strauss 1971 and Almasi, Keefe, Lin and Thompson 1971). See Fig. 2.2(b). Although this detector is easy to fabricate, it still requires external current to operate and also responds to the propagation field which results in a low signal-to-noise ratio.

More recently, the magnetostrictive-piezoelectric (MP) detector (Kinsner and Della Torre 1974, Ishak 1975 and Ishak, Kinsner and Della Torre 1975) and the acoustic-magnetostrictive (AM) detector (Kinsner and Della Torre 1975) were suggested. In the MP detector, the vertical component of the bubble's stray field is used to produce a mechanical strain in a nearby magnetostrictive film (e.g. 60% Ni - 40% Fe permalloy). This strain is coupled to a piezoelectric film (e.g. ZnO), as shown in Fig. 2.2(c), which produces an output signal at a very high output impedance. The noise generated in this detector is much smaller than in the magnetoresistive detector since it does not respond to the propagation field. In the AM detector, a combination of a sonic pulse and the bubble field is used to produce a voltage signal in a magnetostrictive thin film. This detector is capable of detecting a stationary bubble, a property which is needed for a random-access NDRO of a bubble memory configuration.

2.4.3 Bubble Annihilation

An information bit in the form of a bubble can be cleared by the annihilation of the bubble through various techniques. A hairpin conductor could be used to produce a strong magnetic field opposite to the bubble magnetization, or a bubble could be merged to a seed bubble attached to a permalloy sink or a bubble could be propagated to a permalloy guard-rail outside the memory area (Chang 1975).

2.4.4 Bubble Replication

In a serial-access bubble memory, the cycle time can be reduced by utilizing controlled replication of data before reading. The bubble to be read is sent to a replicate circuit where it is cut into two bubbles. One bubble is sent back directly to the original bubble location and the other is routed to a detector circuit. Thus the need for restoring data back into the storage loops after reading is eliminated. The most useful bubble replicators thus far developed employ permalloy elements and a control conductor pattern (Bonyhard, Chen and Smith 1977). Controlled replication is achieved by applying a specified current pulse at an appropriate time within the rotating field cycle. See Fig. 2.2(d).

2.4.5 Bubble Propagation

In a memory system the access of information, through bubble propagation, is done much more frequently than any of the other functions described in Subsections 2.4.1-2.4.4. The success of a bubble memory system, then, depends mainly on how well and reliable bubble propagation is performed. Almost all circuits analyzed in this thesis are bubble propagation circuits.

Bubble propagation is accomplished by spatially varying the strength of the bias field to create a gradient across the bubble. The bubble then moves toward the region of the lower bias field. In practical bubble devices, a traveling local gradient of bias field across the bubble is created by permalloy patterns magnetized by a rotating in-plane field. Figure 2.3 illustrates how a bubble is attracted to a rectangular permalloy bar magnetized by a magnetic field H_T and Fig. 2.4 shows some typical field access bubble propagation circuits. While the T-I and Y-I circuits, shown in Fig. 2.4(a) and (b) respectively, have two gaps per period, the half-disk (gap tolerant) circuits of Fig. 2.4(c) have single gap per period. Gap tolerant circuits offer many advantages over other propagation circuits such as increase of the minimum feature resolution (smallest permalloy dimension) to 1/8 th of a period, excellent bias field margins and the elimination of channel-to-channel interconnection elements (such as the I bars in Fig. 2.4(a) and (b)).

The parallel-bar (Della Torre and Kinsner 1973) and the channel-bar (Della Torre and Kinsner 1975) circuits have the advantage

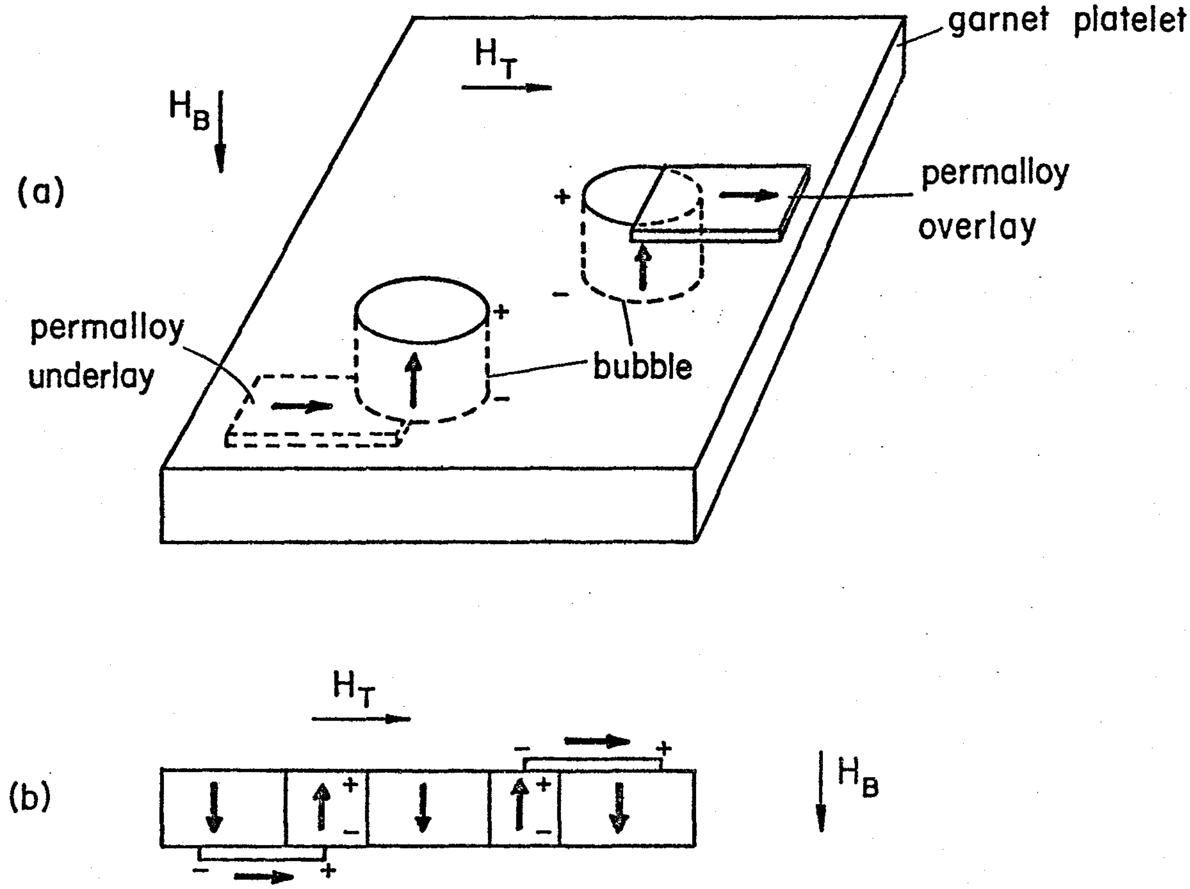

Figure 2.3 Bubble domains attracted to the ends of permalloy overlays and underlays by an in-plane field H_T.

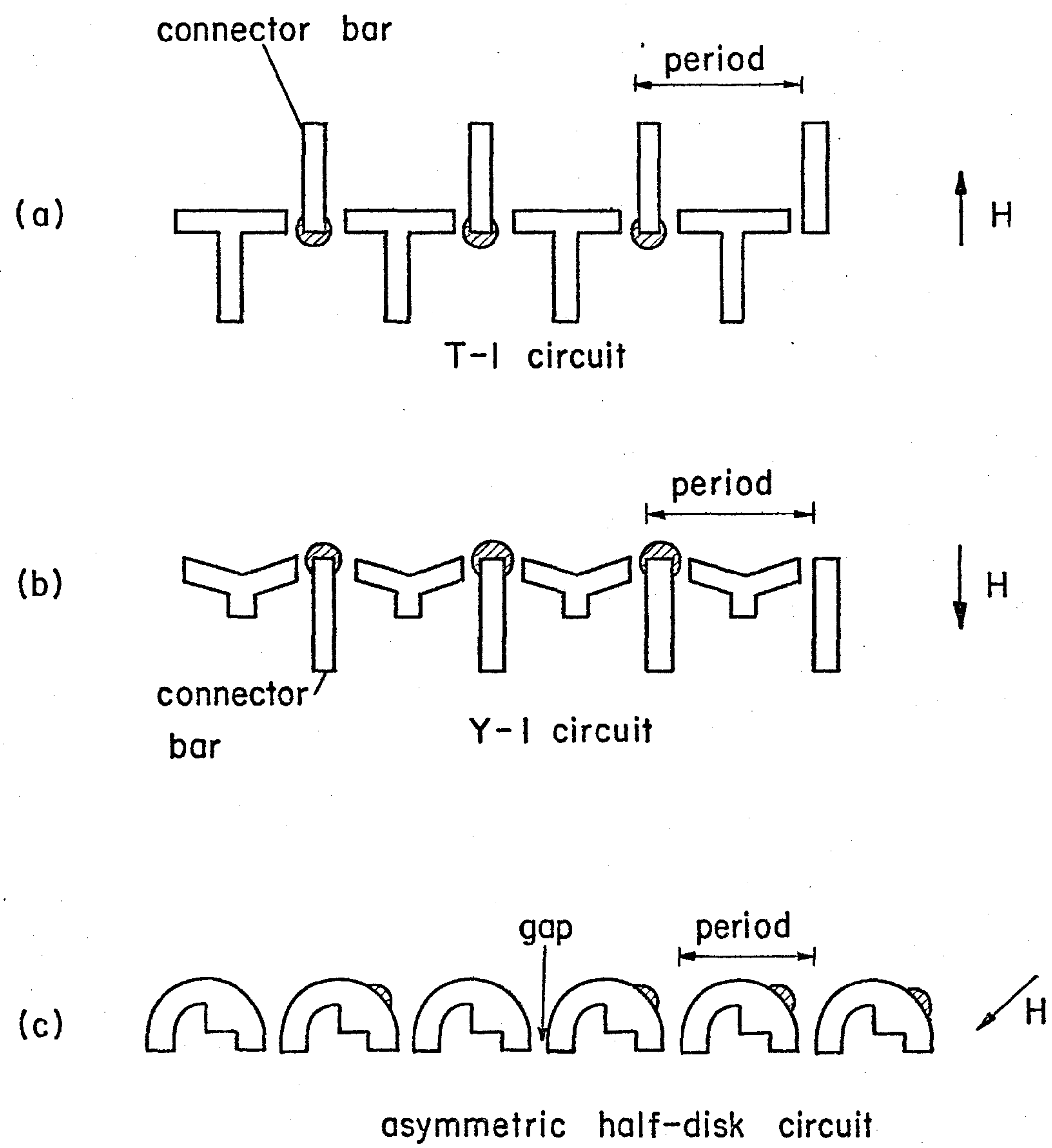

Figure 2.4 Bubble propagation circuits: (a) T-I circuit (Perneski 1969), (b) Y-I circuit (Danylchuk 1971) and (c) asymmetric half-disk circuit (Bonyhard and Smith 1976).

of requiring an oscillating propagation field rather than a rotating field, thus saving one propagation coil. By adjusting the overlapping between successive bars, the parallel-bar circuit produces linear and uniform bubble propagation.

2.5 The Modeling Problem

The simplest field access bubble circuit is composed of a permalloy circuit overlay - magnetized by an in-plane transverse field, adjacent to a magnetic bubble domain, stabilized by a bias field (see Fig. 2.3). The modeling of such a circuit requires the solution of two basic problems: the forward modeling problem and the backward modeling problem. In the former, the changes in the permalloy magnetization and total energy, due to the in-plane propagation field, the bubble's stray field and the bias field, are to be computed. The later problem deals with computation of the changes in bubble size and shape due to the change in the permalloy total energy. A complete modeling technique should be able to solve both the forward and the backward modeling problems. While the forward problem has been analyzed by various authors, the backward problem has only been investigated experimentally.

Modeling techniques for the forward problem vary according to how one can characterize the permalloy material (bubble circuit material). This results in three main modeling approaches: micromagnetic models, domain models and continuum models.

2.6 Micromagnetic Models

Almost all field access bubble propagation circuits are made of thin ferromagnetic films such as a non-magnetostrictive permalloy (80% Ni - 20% Fe). These ferromagnetic films in the demagnetized state (e.g. zero applied field) are divided into a number of small regions called domains. Each domain is spontaneously magnetized to the saturation value, M_s, but the directions of magnetization of the various domains are such that the specimen as a whole has zero net magnetization (Cullity 1972).

A micromagnetic model for a permalloy element placed in an applied field H_A, typically used in bubble circuits, should thus take into account the ferromagnetic nature of the permalloy. The magnetization vector at any point in the permalloy must be of a constant magnitude equal to M_s. Only the direction of this vector is allowed to vary. In addition, an accurate micromagnetic analysis requires the computation of the magnetization distribution over a very large number of points in the permalloy. A typical permalloy bar of dimensions 15x3x0.4 μm requires a mesh of about 18000 points. This will result in a cell size (the distance between two neighboring points) of about 500 Å which reasonably simulates a micromagnetic cell for such bar. For such small cell dimensions, the exchange force (a force, quantum mechanical in origin, trying to align the magnetization vectors parallel to each other), and hence the exchange energy, will contribute a significant term to the total energy.

The actual magnetization distribution in a permalloy element, for

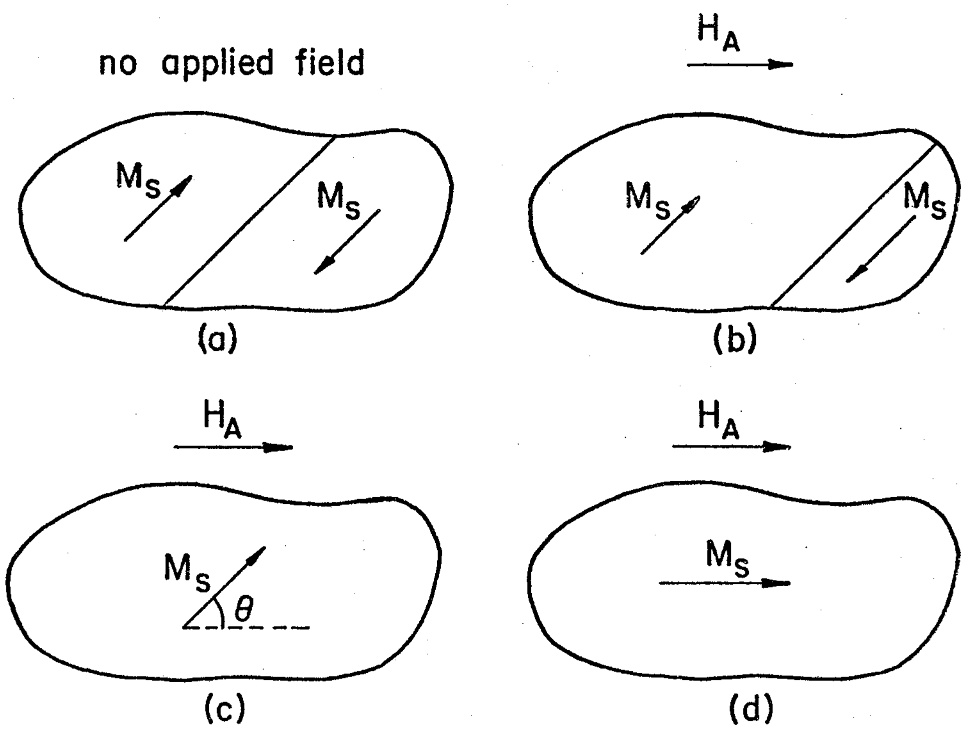

Figure 2.5 A magnetic body (a) in the demagnetized state responds to an applied field H_A by (b) a domain wall motion where the domains whose magnetization are closest to H_A grow at the expense of the other domains until (c) the whole body becomes a single domain and then (d) a magnetization rotation occurs to make M_s parallel to H_A.

any applied field configuration, is obtained by minimizing the permalloy total energy. This distribution should describe the domain structure, including domain walls, in the permalloy.

Due to the large amount of computations and large computer memory requirements involved in this approach, micromagnetic modeling has been avoided by most of the workers in the area of bubble circuit modeling. This problem, however, is discussed in detail in Chapter 3.

2.7 Domain Models

This approach assumes an initial domain distribution in the permalloy, with zero domain wall thickness. The presence of an applied field changes the overall magnetization distribution by an increase in the volume of the domains whose magnetization directions are closest to the applied field, at the expense of the other domains (Della Torre and Longo 1969 and Cullity 1972). See Fig. 2.5.

In one of the domain models, Della Torre and Kinsner (1973) assumed a two domain configuration per rectangular bar as shown in Fig. 2.6(a). This one-dimensional model (the magnetization is allowed to vary only along the bar's long axis) is fairly accurate for analyzing bars with relatively large aspect ratio (length/width). However, experimental observations proved that for short bars, the closure domain configuration, shown in Fig. 2.6(b), should be considered. It was shown (Della Torre and Kinsner 1973) that assuming more than two parallel domains per bar will not produce significant changes in the magnetization distribution.

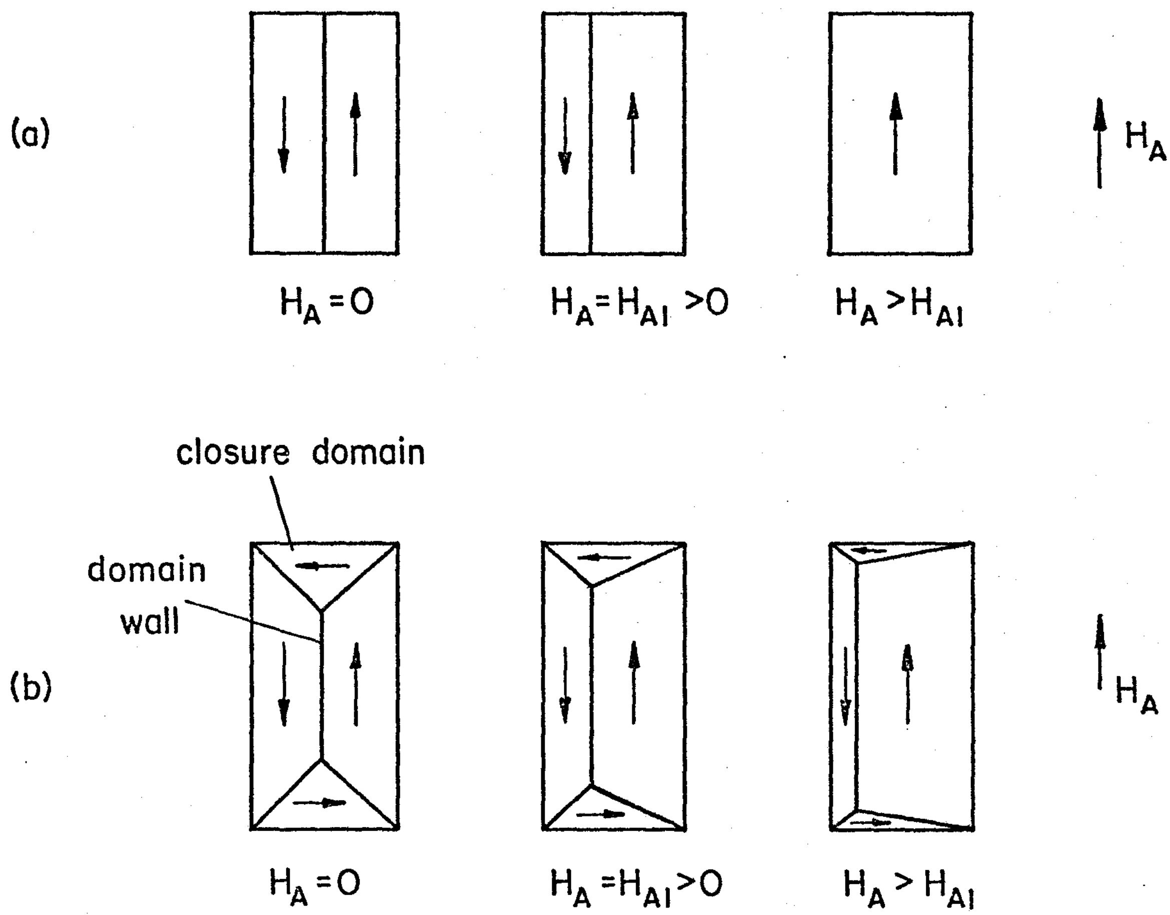

Figure 2.6 Domains and domain walls in rectangular permalloy bars. (a) two longitudinal domains per bar (Della Torre and Kinsner 1973) and (b) a closure domain configuration (Khaiyer 1976).

Khaiyer (1975) suggested a two-dimensional domain model using the closure domain configuration of Fig. 2.6(b). The magnetization, in this model, is allowed to vary along the bar length and width. Only straight domain walls are allowed which is questionable if the bubble's stray field is considered.

2.8 Continuum Models

Continuum models are based on approximating the magnetization in a permeable body by a continuous distribution rather than division into domains. This approach allows using mathematical simulation techniques to compute an average magnetization distribution.

A magnetostatic model for analyzing bubble-permalloy configurations in the absence of in-plane propagation fields was introduced by Boyarchenkov, Raev, Samarin, Balbashov and Chervonenkis (1971). In their model, the charge distribution, on the permalloy element, due to the presence of the bubble domain is computed using an approximate expression for the bubble field (Bobeck 1967). Copeland (1972) suggested a one dimensional continuum model for rectangular permalloy bars using a series expansion to approximate the demagnetizing field (the field set up by the magnetization) in the permalloy. Starting with an initial magnetization distribution, an iterative procedure is used to compute the final one-dimensional magnetization distribution. The model, formulated in this way, is not capable of analyzing cases where two permalloy elements interact with each other.

Later, Lin (1972) introduced another one-dimensional model in which he used a Fourier series method to compute the magnetization distribution in rectangular permalloy bars. No extension to the two-dimensional case was made.

A three-dimensional model was introduced by Kinsner and Della Torre (1972) in which the Poisson's equation for inhomogeneous medium was solved using an iterative technique. Various bubble propagation circuits were analyzed including T-I, Y-I and Chevron circuits (Kinsner and Della Torre 1975). In that model the polarizing influence of the bubble's stray field was not taken into consideration.

Archer, Tocci, George and Chen (1972) and, later, George and Archer (1973a,b) suggested an energy minimization technique to solve for a two-dimensional magnetization distribution in permalloy circuits. The total local field (the vectorial sum of the applied field and the demagnetizing field) is assumed to be identically zero everywhere in the permalloy. This assumption implies that the susceptibility of the permalloy must be infinite to achieve finite magnetization values. This is a disadvantage of the model since measurements proved that thin permalloy films, when etched into small bars, will possess a finite susceptibility in the range of 200-2000 (Dove, Watson, Ma and Huijer 1976 and Feng and Thompson 1977). Basic to the magnetization computation, in this model, is the solution of a large system of linear equations. A typical permalloy bar modeling problem with a mesh of 100 points (points at which the magnetization is to be computed) requires the solution of a set of 200 equations. In addition to large computer memory requirements, the coefficients in these equations may vary over a wide range which may result in an ill-conditioned formulation (Wilkinson 1963). The model was used to analyze various thick permalloy bars (George and Archer 1973a) and chevron circuits (George and Hughes 1976a).

Dove, Watson, Huijer and Ma (1975) used a Fourier series method for the calculation of the permalloy magnetization and energy. Spatial variation of the demagnetizing field in the permalloy was represented in this model by a Fourier series expansion and only rectangular bars were analyzed.

2.9 Analytical Models

A new approach for modeling of bubble circuits was introduced by Almasi, Lin, Munro and Slusarczuk (1974) and generalized by Almasi and Lin (1976). In this model the problem was approached from the viewpoint of the bubble, that is the change in the bubble energy due to the presence of the magnetized permalloy circuit. Approximate analytical expressions were derived giving the change in the bubble energy as functions of the circuit parameters (permalloy and bubble parameters). Although this model offers a simple computation procedure, yet the error in the energy values could be as high as 20% (Almasi and Lin 1976). Using this technique, the forward modeling problem is not solved and it is difficult to analyze complicated propagation structures such as gap tolerant circuits.

2.10 Conclusions

In summary, there exist several modeling techniques for analyzing simple bubble domain field access propagate structures. Some are unrealistic especially when dealing with thin permalloy circuits and some are approximate and cannot deal with complicated shapes of propagation circuits such as gap tolerant circuits. It is the rapid and varied development in the shapes and characteristics of bubble propagation structures, and hence the necessity of developing a general, accurate and efficient model that formed the motivation of this research work.

CHAPTER 3

NEW APPROACHES TO BUBBLE CIRCUIT MODELING

3.1 Introduction

In this chapter new techniques for modeling of field access bubble propagation circuits are presented. First a micromagnetic model for magnetized permalloy circuits is given. The implementation of this analysis was successful; however, it was not practical for use in an optimization program since it required excessive running time and memory storage. Several assumptions are examined that led to a simplified analysis which introduced a new continuum model. In the remainder of this chapter, this continuum model is described in detail.

Both models are numerical in nature and iterative schemes are used to compute the magnetization distribution in the permalloy overlay described in Chapter 2. In the continuum model an arbitrary M-H relation is used to express the permalloy's nonlinear characteristics. The model is capable of handling arbitrary permalloy shapes in two dimensions. Various examples are analyzed using the continuum model and comparison to the results of models of other workers is given.

3.2 Statement of the Problem

An objective of the forward modeling problem, described in Section 2.5, is to find the magnetization distribution $\underset{\sim}{M}(\underset{\sim}{r})$ and the total energy E_p of a permalloy body placed in an applied field $\underset{\sim}{H}_A(\underset{\sim}{r})$, where $\underset{\sim}{r}$ is a position vector. See Fig. 3.1. The applied field $\underset{\sim}{H}_A(\underset{\sim}{r})$, in a typical field access bubble circuit, is composed of four components:

(1) $\underset{\sim}{H}_B$; the bias field required to stabilize bubble domains in a bubble circuit. This field is usually produced by a pair of permanent magnets and is normal to the permalloy plane, that is applied in the z-direction,

(2) $\underset{\sim}{H}_T$; the transverse in-plane field required for the propagation of bubble domains. A pair of coils is required to produce this field which is uniform, rotatable about the z-axis and applied in the x-y plane,

(3) $\underset{\sim}{H}_R(\underset{\sim}{r})$; the radial component of the bubble's stray field which is highly nonuniform in the x-y plane, and

(4) $\underset{\sim}{H}_N(\underset{\sim}{r})$; the normal component of the bubble's stray field which is nonuniform and in the z-direction.

An algorithm for the computation of the bubble's stray field is given later in Subsection 3.4.1.

When a bar is magnetized by an applied field, a demagnetizing field $\underset{\sim}{H}_D(\underset{\sim}{r})$ is created which acts generally in the opposite direction of the magnetization $\underset{\sim}{M}(\underset{\sim}{r})$. The computation of $\underset{\sim}{H}_D(\underset{\sim}{r})$ for an arbitrary shaped magnetized body is one of the most difficult problems in the following analysis. Subsections 3.4.2 and 3.5.1 describe in detail such computations.

In general, the total energy E_p of a magnetized body is composed of the following terms:

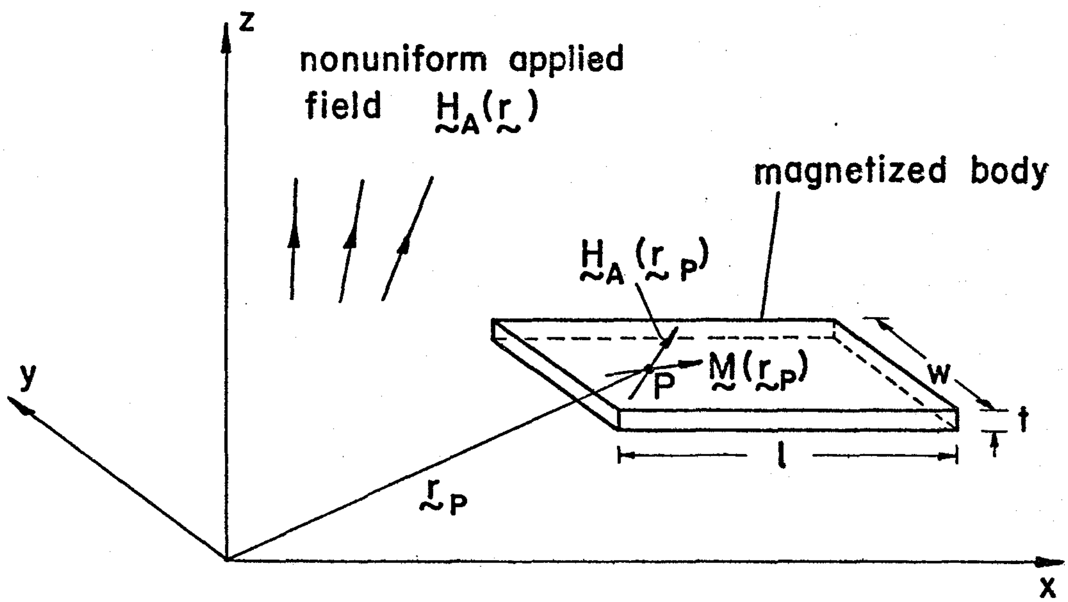

Figure 3.1 A rectangular permalloy bar of dimensions ℓ x w x t in the x-y plane. The z-axis is perpendicular to the bar plane. The applied field and magnetization at point P, whose position vector is $\underset{\sim}{r}_P$, are $\underset{\sim}{H}_A(\underset{\sim}{r}_P)$ and $\underset{\sim}{M}(\underset{\sim}{r}_P)$, respectively.

(1) An applied field energy term E_A,

(2) A demagnetizing energy term E_D,

(3) A magnetocrystalline anisotropy energy term E_{MA},

(4) An exchange energy term E_{EX} and

(5) A magnetoelastic energy term E_{ME}.

The goal of micromagnetic analysis of a magnetic body is the computation of the magnetization distribution $\underset{\sim}{M}(\underset{\sim}{r})$ which will minimize the total energy

$$E_P = E_A + E_D + E_{MA} + E_{EX} + E_{ME} \quad . \tag{3.1}$$

3.3 Energy Analysis

The following analysis refers to ferromagnetic and ferrimagnetic bodies where the magnetization of each elementary subvolume ΔV in the body is of fixed magnitude but variable orientation. When a field $\underset{\sim}{H}_A(\underset{\sim}{r})$ is applied to such a body, the torque exerted on each subvolume ΔV is given by $\underset{\sim}{H}_A(\underset{\sim}{r}) \times \underset{\sim}{M}(\underset{\sim}{r}) \; \Delta V$. This torque tends to align $\underset{\sim}{M}(\underset{\sim}{r})$ parallel to $\underset{\sim}{H}_A(\underset{\sim}{r})$. The total applied field energy may be written as (Cohen 1970)

$$E_A = - \mu_o \int_{V_P} \underset{\sim}{H}_A(\underset{\sim}{r}) \cdot \underset{\sim}{M}(\underset{\sim}{r}) \; dV \; , \tag{3.2}$$

where V_P is the volume of the body.

Similarly, the demagnetizing energy which will result from the creation of $\underset{\sim}{H}_D(\underset{\sim}{r})$, inside the body, is given by (Cohen 1970)

$$E_D = -\frac{1}{2}\mu_o \int_{V_P} \underset{\sim}{H}_D(\underset{\sim}{r}) \cdot \underset{\sim}{M}(\underset{\sim}{r})\, dV \quad . \tag{3.3}$$

The factor 1/2 arises from the fact that self-energy is involved. The demagnetizing field $\underset{\sim}{H}_D(\underset{\sim}{r}_i)$ at point i is computed by summing the contributions of the magnetization $\underset{\sim}{M}(\underset{\sim}{r}_j)$ at all points in the body. The contribution from the magnetization $\underset{\sim}{M}(\underset{\sim}{r}_j)$ to the demagnetizing field $\underset{\sim}{H}_D(\underset{\sim}{r}_i)$ depends on the distance between the two points, $|\underset{\sim}{r}_{ij}|$, and the shape of the magnetic body. The demagnetizing energy E_D is, thus, sometimes called the shape energy or shape anisotropy energy.

In addition to shape anisotropy, the magnetized body, due to its crystalline structure, exhibits a magnetocrystalline anisotropy. Generally speaking, any body has one or more easy directions of magnetization (directions along which the body can be magnetized to saturation with quite low fields). Any attempt to magnetize it in some other direction results in an increase in its internal energy by an amount called the magnetocrystalline anisotropy energy. It is convenient to define this energy in terms of the direction cosines $\alpha_x(\underset{\sim}{r})$, $\alpha_y(\underset{\sim}{r})$ and $\alpha_z(\underset{\sim}{r})$ of the magnetization $\underset{\sim}{M}(\underset{\sim}{r})$ in the form (Della Torre and Longo 1969)

$$E_{MA} = \int_{V_P} \{K_0 + K_1[\alpha_x^2(\underset{\sim}{r})\,\alpha_y^2(\underset{\sim}{r}) + \alpha_y^2(\underset{\sim}{r})\,\alpha_z^2(\underset{\sim}{r}) + \alpha_z^2(\underset{\sim}{r})\,\alpha_x^2(\underset{\sim}{r})] + K_2\,\alpha_x^2(\underset{\sim}{r})\,\alpha_y^2(\underset{\sim}{r})\,\alpha_z^2(\underset{\sim}{r}) + \ldots\}dV \tag{3.4}$$

where K_0, K_1, K_2, ... are the anisotropy constants of the body. Higher powers are generally not needed and sometimes K_2 is so small that the term involving it can be neglected. Since we are usually interested in the change in the energy when $\underset{\sim}{M}(\underset{\sim}{r})$ is changed, the term K_0 need not be considered. In uniaxial magnetic bodies, E_{MA} reduces to

$$E_{MA} = \int_{V_P} K_1 \sin^2 \theta_M(\underset{\sim}{r}) \, dV \tag{3.5}$$

where $\theta_M(\underset{\sim}{r})$ is the angle between the magnetization and the easy axis. In this case K_1 is called the uniaxial anisotropy constant.

The atomic structure of a ferromagnetic material, such as permalloy, is such that exchange forces of a quantum-mechanical nature tend to force the spins of adjacent atoms to lie in parallel directions. The exchange forces are short range and decline so markedly with distance that only adjacent atoms interact. The exchange energy is given by (Brown 1963)

$$E_{EX} = \int_{V_p} A_{EX} \{[\underset{\sim}{\nabla} \alpha_x(\underset{\sim}{r})]^2 + [\underset{\sim}{\nabla} \alpha_y(\underset{\sim}{r})]^2 + [\underset{\sim}{\nabla} \alpha_z(\underset{\sim}{r})]^2\} \, dV \tag{3.6}$$

where A_{EX} is the permalloy exchange constant.

When a substance is exposed to a magnetic field, its dimensions change due to magnetostriction. Conversely, when a stress, or a strain, is applied to a magnetic material, its magnetization changes due to the magnetoelastic effect. The magnetoelastic energy term is given by (Cohen 1970)

$$E_{MA} = - \int_{V_P} \lambda_{ME} \, \underset{\sim}{\sigma}(\underset{\sim}{r}) \sin^2 [\theta_\sigma(\underset{\sim}{r})] \, dV, \tag{3.7}$$

where λ_{ME} is the magnetoelastic constant, $\underset{\sim}{\sigma}(\underset{\sim}{r})$ is the stress vector and $\theta_\sigma(\underset{\sim}{r})$ is the angle between the stress and the magnetization.

3.4 A Micromagnetic Model

Brown (1977) showed that the magnetoelastic energy of the body can be reduced to an expression similar to that in (3.4) (or (3.5) in case of uniaxial materials). Therefore, the effect of the elastic and magnetoelastic properties of the material can be combined and the magnetocrystalline anisotropy constants at zero strain (K_0, K_1, K_2, ... in (3.4)) replaced by slightly different elastic constants so that

$$E_M = E_{MA} + E_{ME} \simeq \int_{V_P} \{K_0' + K_1'[\alpha_x^2(\underset{\sim}{r})\,\alpha_y^2(\underset{\sim}{r}) + \alpha_y^2(\underset{\sim}{r})\,\alpha_z^2(\underset{\sim}{r}) + \alpha_z^2(\underset{\sim}{r})\,\alpha_x^2(\underset{\sim}{r})] + K_2'\,\alpha_x^2(\underset{\sim}{r})\,\alpha_y^2(\underset{\sim}{r})\,\alpha_z^2(\underset{\sim}{r}) + \ldots\}\,dV, \tag{3.8}$$

where K_0', K_1', K_2', ... are the new anisotropy constants. For uniaxial materials,

$$E_M = E_{MA} + E_{ME} \simeq \int_{V_P} K_1' \sin^2 [\theta_M(\underset{\sim}{r})]\,dV\ . \tag{3.9}$$

Using (3.2), (3.3), (3.6) and (3.8), E_P can be expressed as

$$E_P = \int_{V_P} \Big[-\mu_o\,\underset{\sim}{H}_A(\underset{\sim}{r}) \cdot \underset{\sim}{M}(\underset{\sim}{r}) - \frac{1}{2}\mu_o\,\underset{\sim}{H}_D(\underset{\sim}{r}) \cdot \underset{\sim}{M}(\underset{\sim}{r}) + A_{EX}\{[\underset{\sim}{\nabla}\,\alpha_x(\underset{\sim}{r})]^2 + [\underset{\sim}{\nabla}\,\alpha_y(\underset{\sim}{r})]^2 + [\underset{\sim}{\nabla}\,\alpha_z(\underset{\sim}{r})]^2\} + K_1' F_A\,[\alpha_x(\underset{\sim}{r}), \alpha_y(\underset{\sim}{r}), \alpha_z(\underset{\sim}{r})] \Big]\,dV \tag{3.10}$$

where

$$F_A[\alpha_x(\underset{\sim}{r}), \alpha_y(\underset{\sim}{r}), \alpha_z(\underset{\sim}{r})] \overset{\Delta}{=} \alpha_x^2(\underset{\sim}{r})\, \alpha_y^2(\underset{\sim}{r}) + \alpha_y^2(\underset{\sim}{r})\, \alpha_z^2(\underset{\sim}{r}) + \alpha_z^2(\underset{\sim}{r})\, \alpha_x^2(\underset{\sim}{r}) \qquad (3.11)$$

is the effective magnetocrystalline-magnetoelastic anisotropy function.

To find the equilibrium condition for $\underset{\sim}{M}(\underset{\sim}{r})$, we imagine the magnetization to undergo virtual variations $\delta\underset{\sim}{M}(\underset{\sim}{r})$ subject to the constraint

$$|\underset{\sim}{M}(\underset{\sim}{r}_i)| = M_s \quad , \quad i = 1, 2, \ldots, N \quad , \qquad (3.12)$$

and require that the resulting first derivatives of E_P be zero. The constraints (3.12) can, alternatively, be stated as (Brown 1963)

$$\delta\, \underset{\sim}{1}_M(\underset{\sim}{r}_i) = \delta\underset{\sim}{\xi} \times \underset{\sim}{1}_M(\underset{\sim}{r}_i), \; i = 1, 2, \ldots, N \quad , \qquad (3.13)$$

where

$$\underset{\sim}{1}_M(\underset{\sim}{r}_i) = \alpha_x(\underset{\sim}{r}_i)\, \underset{\sim}{1}_x + \alpha_y(\underset{\sim}{r}_i)\, \underset{\sim}{1}_y + \alpha_z(\underset{\sim}{r}_i)\, \underset{\sim}{1}_z, \; i = 1, 2, \ldots, N \qquad (3.14)$$

is a unit vector along $\underset{\sim}{M}(\underset{\sim}{r}_i)$ and $\delta\underset{\sim}{\xi}$ is an arbitrary small vector which discribes a rotation of $\underset{\sim}{1}_M(\underset{\sim}{r}_i)$ through a small angle $|\delta\underset{\sim}{\xi}|$ about an axis in the direction of $\delta\underset{\sim}{\xi}$. The equilibrium condition, therefore, requires that (neglecting surface effects)

$$\underset{\sim}{1}_M(\underset{\sim}{r}_i) \times \underset{\sim}{H}_L(\underset{\sim}{r}_i) = 0, \; i = 1, 2, \ldots, N, \qquad (3.15)$$

where

$$\underset{\sim}{H}_L(\underset{\sim}{r}_i) = \underset{\sim}{H}_A(\underset{\sim}{r}_i) + \underset{\sim}{H}_D(\underset{\sim}{r}_i) + \underset{\sim}{H}_{EX}(\underset{\sim}{r}_i) - \frac{1}{M_s} \frac{\partial E_M}{\partial \underset{\sim}{1}_M(\underset{\sim}{r}_i)} \quad , \quad i = 1, 2, \ldots, N, \qquad (3.16)$$

$$\underset{\sim}{H}_{EX}(\underset{\sim}{r}_i) \stackrel{\Delta}{=} \frac{2A_{EX}}{\mu_o M_s} \nabla^2\left[\underset{\sim}{1}_M(\underset{\sim}{r}_i)\right], \; i = 1, 2, \ldots, N, \tag{3.17}$$

and

$$\frac{\partial}{\partial \underset{\sim}{1}_M(\underset{\sim}{r})} \stackrel{\Delta}{=} \frac{\partial}{\partial \alpha_x(\underset{\sim}{r})} \underset{\sim}{1}_x + \frac{\partial}{\partial \alpha_y(\underset{\sim}{r})} \underset{\sim}{1}_y + \frac{\partial}{\partial \alpha_z(\underset{\sim}{r})} 1_z \; . \tag{3.18}$$

If the permalloy has no anisotropy, then (3.17) reduces to

$$\underset{\sim}{H}_L(\underset{\sim}{r}_i) = \underset{\sim}{H}_A(\underset{\sim}{r}_i) + \underset{\sim}{H}_D(\underset{\sim}{r}_i) + \underset{\sim}{H}_{EX}(\underset{\sim}{r}_i), \; i = 1, 2, \ldots, N \tag{3.19}$$

and the equilibrium condition is satisfied by setting (see Fig. 3.2(b))

$$\theta_M(\underset{\sim}{r}_i) = \theta_L(\underset{\sim}{r}_i), \qquad i = 1, 2, \ldots, N \; . \tag{3.20}$$

From now on, a symbol that denotes a vector without a tilde will refer to the vector magnitude. For example $H_L(\underset{\sim}{r}) \stackrel{\Delta}{=} |\underset{\sim}{H}_L(\underset{\sim}{r})|$.

In most bubble circuits, the dimensions in the plane of the permalloy film (x-y plane in Fig. 3.1) are very large compared to the film thickness. For example, in a 3 μm diameter bubble circuit, typical dimensions of a rectangular bar would be 7.5 x 1.5 x 0.3 μm. This gives a length-to-thickness ratio and a width-to-thickness ratio of 25 and 5, respectively. Therefore, $\underset{\sim}{M}(\underset{\sim}{r})$ tends to lie in the film plane, since if for any reason, $\underset{\sim}{M}(\underset{\sim}{r})$ tilts out of the plane, the resulting demagnetizing field will be large enough to pull it back (Cohen 1970 and Cullity 1972). To a good approximation, the following analysis will refer to a two-dimensional magnetization distribution $\underset{\sim}{M}(\underset{\sim}{r})$ in the x-y plane. Moreover, the bias field $\underset{\sim}{H}_B$ and the normal component of the bubble's stray field $\underset{\sim}{H}_N(\underset{\sim}{r})$ will not affect the magnetization $\underset{\sim}{M}(\underset{\sim}{r})$ since they are in the z-direction.

The problem can still be simplified by assuming that the magnetization distribution $\underset{\sim}{M}(\underset{\sim}{r})$ is to be computed over a discrete mesh of N points distributed uniformly over the magnetic body. Since the magnetization vector has a constant magnitude, over an elementary subvolume ΔV in a ferromagnetic body, it is thus required to compute the direction of $\underset{\sim}{M}(\underset{\sim}{r}_i)$, in the x-y plane, where i = 1, 2, ..., N. This magnetization distribution should be in such a way that E_P of (3.12) is minimized relative to small variations in the magnetization.

Figure 3.2(a) illustrates a two-dimensional mesh of N points, in the x-y plane, over a permalloy bar of dimensions ℓ, w and t. It will be assumed that the magnetization $\underset{\sim}{M}(\underset{\sim}{r}_i)$ at point i represents the magnetization over a cell of dimensions Δx and Δy, $(1/2)\Delta x$ and $(1/2)\Delta y$, Δx and $(1/2)\Delta y$ and $(1/2)\Delta x$ and Δy for interior, corner, x-edge and y-edge points, respectively. A typical point, i, of the mesh is shown in Fig. 3.2(b) together with the fields $\underset{\sim}{H}_A(\underset{\sim}{r}_i)$, $\underset{\sim}{H}_D(\underset{\sim}{r}_i)$ and $\underset{\sim}{H}_{EX}(\underset{\sim}{r}_i)$. The following subsections describe, in detail, the computation of $\underset{\sim}{H}_A(\underset{\sim}{r})$, $\underset{\sim}{H}_D(\underset{\sim}{r})$ and $\underset{\sim}{H}_{EX}(\underset{\sim}{r})$.

3.4.1 Computation of the Applied Field

Considering only field components in the x-y plane, the total applied field is given by

$$\underset{\sim}{H}_A(\underset{\sim}{r}) = \underset{\sim}{H}_T + \underset{\sim}{H}_R(\underset{\sim}{r}) \quad . \tag{3.21}$$

Expressions for $\underset{\sim}{H}_R(\underset{\sim}{r})$ and $\underset{\sim}{H}_N(\underset{\sim}{r})$ in terms of the elliptical integrals of the first, second and third kinds are available in the literature (Lin 1972 and Almasi and Lin 1976). Since $\underset{\sim}{H}_R(\underset{\sim}{r})$ will be computed at large

(a)

(b)

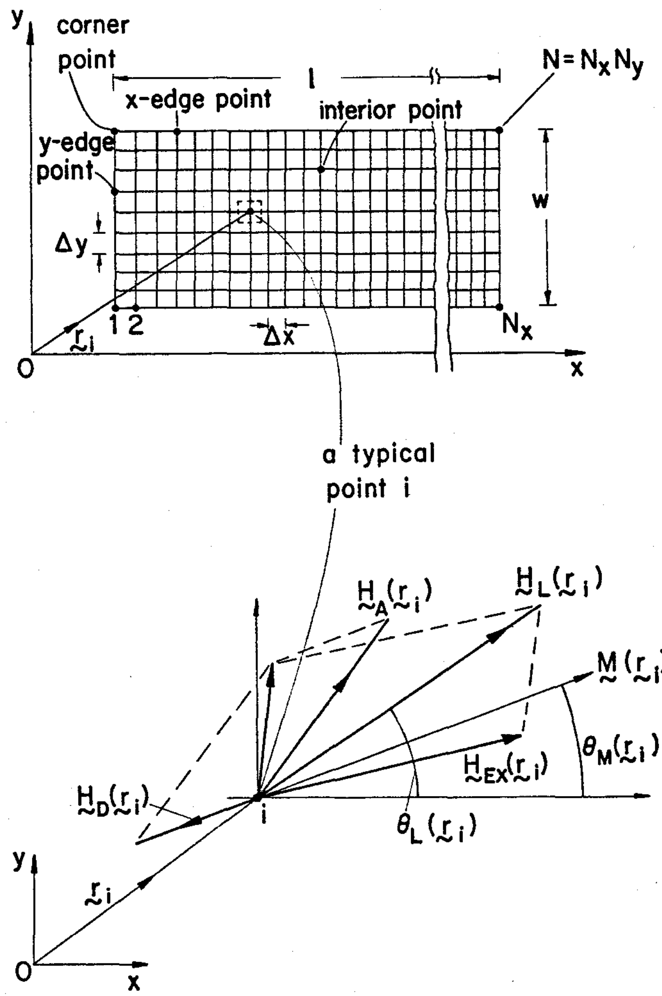

Figure 3.2 A discretization mesh of N points placed over a permalloy bar in the x-y plane. (a) the cell dimensions are Δx and Δy and (b) at point i, the total local field $H_L(r_i)$ is inclined at an angle $\theta_L(r_i)$ to the x-axis.

number of points in the permalloy, an efficient and fast algorithm is required. It was decided to use the expressions derived by Druyvesteyn, Tjaden and Dorleijn (1972) where the bubble's stray field components are expressed in terms of a single generalized elliptical integral

$$CEL(k,p,a,b) = \int_0^{\pi/2} \frac{a\cos^2\psi + b\sin^2\psi}{\cos^2\psi + p\sin^2\psi} \frac{d\psi}{\sqrt{\cos^2\psi + k^2\sin^2\psi}} \quad . \tag{3.22}$$

They showed that (see Fig. 3.3)

$$\underset{\sim}{H}_R(\underset{\sim}{r}) = \frac{-2RM_B}{\pi}\left[\frac{CEL(k_1,1,-1,1)}{\sqrt{(R+r)^2 + z^2}} - \frac{CEL(k_2,1,-1,1)}{\sqrt{(R+r)^2 + (z+h)^2}}\right]\underset{\sim}{1}_r , \tag{3.23}$$

where $\underset{\sim}{1}_r$ is a unit radial vector,

$$k_1^2 = \frac{(R-r)^2 + z^2}{(R+r)^2 + z^2} \tag{3.24}$$

and

$$k_2^2 = \frac{(R-r)^2 + (z+h)^2}{(R+r)^2 + (z+h)^2} \quad . \tag{3.25}$$

A FORTRAN IV program was implemented and tested (Ishak and Della Torre 1976) for computing the bubble's stray field using an iterative scheme to compute the CEL function (Bulirsch 1969). The program proved to be efficient and accurate.

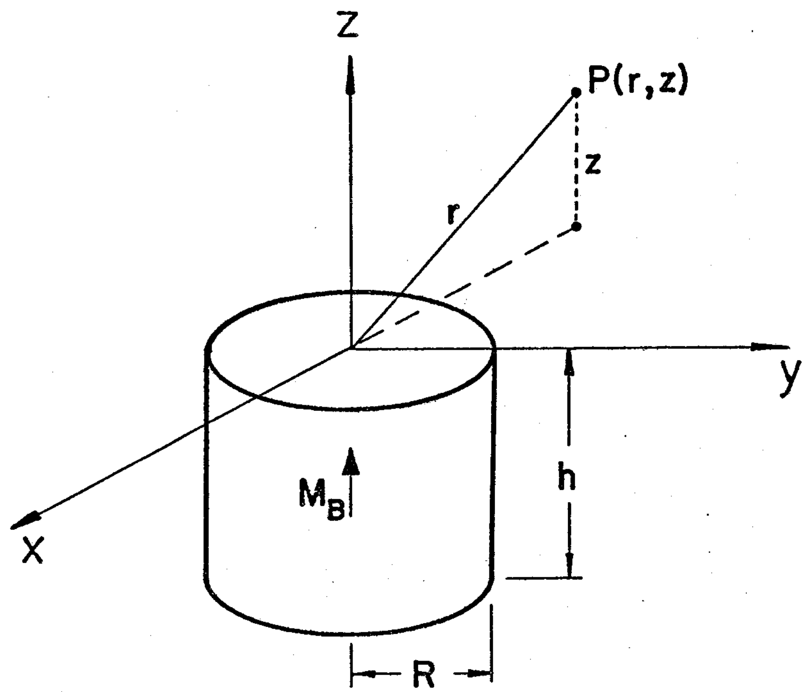

Figure 3.3 The coordinate system used to compute the radial component of the bubble's stray field at a point P(r,z).

3.4.2 Computation of the Demagnetizing Field

The demagnetizing field $\underset{\sim}{H}_D(\underset{\sim}{r}_i)$, at point i, will be given by (Della Torre and Longo 1969)

$$\underset{\sim}{H}_D(\underset{\sim}{r}_i) = -\frac{1}{4\pi} \underset{\sim}{\nabla}_i \int_{V_P} \underset{\sim}{\nabla}_j \frac{1}{|\underset{\sim}{r}_{ij}|} \cdot \underset{\sim}{M}(\underset{\sim}{r}_j)\, dV_j \tag{3.26}$$

where $\underset{\sim}{\nabla}_i$ and $\underset{\sim}{\nabla}_j$ are the nabla operators with respect to the field point i and the source point j, respectively as shown in Fig. 3.4. The x and y components of $\underset{\sim}{H}_D(\underset{\sim}{r}_i)$ can be written as

$$H_{D_x}(\underset{\sim}{r}_i) = \int\int [D_{xx}(\underset{\sim}{r}_i;\underset{\sim}{r}_j)\, M_x(\underset{\sim}{r}_j) + D_{xy}(\underset{\sim}{r}_i;\underset{\sim}{r}_j)\, M_y(\underset{\sim}{r}_j)]dx_j dy_j, \tag{3.27}$$

$$H_{D_y}(\underset{\sim}{r}_i) = \int\int [D_{yx}(\underset{\sim}{r}_i;\underset{\sim}{r}_j)\, M_x(\underset{\sim}{r}_j) + D_{yy}(\underset{\sim}{r}_i;\underset{\sim}{r}_j)\, M_y(\underset{\sim}{r}_j)]dx_j dy_j, \tag{3.28}$$

where the coefficients $D_{xx}(\underset{\sim}{r}_i;\underset{\sim}{r}_j)$, $D_{xy}(\underset{\sim}{r}_i;\underset{\sim}{r}_j)$, $D_{yx}(\underset{\sim}{r}_i;\underset{\sim}{r}_j)$ and $D_{yy}(\underset{\sim}{r}_i;\underset{\sim}{r}_j)$ are functions of the permalloy thickness t and the distance d_{ij} between the field point i and the source point j. In Appendix B expressions for these coefficients are derived in detail.

Since $M(\underset{\sim}{r}_j)$ is constant over an elementary cell around point j, it can be shown that (3.27) and (3.28) reduce to

$$H_{D_x}(\underset{\sim}{r}_i) = \sum_{j=1}^{N} [M_x(\underset{\sim}{r}_j)\ \mathcal{D}_{xx}(\underset{\sim}{r}_i;\underset{\sim}{r}_j) + M_y(\underset{\sim}{r}_j)\ \mathcal{D}_{xy}(\underset{\sim}{r}_i;\underset{\sim}{r}_j)] , \tag{3.29}$$

$$H_{D_y}(\underset{\sim}{r}_i) = \sum_{j=1}^{N} [M_x(\underset{\sim}{r}_j)\ \mathcal{D}_{yx}(\underset{\sim}{r}_i;\underset{\sim}{r}_j) + M_y(\underset{\sim}{r}_j)\ \mathcal{D}_{yy}(\underset{\sim}{r}_i;\underset{\sim}{r}_j)] , \tag{3.30}$$

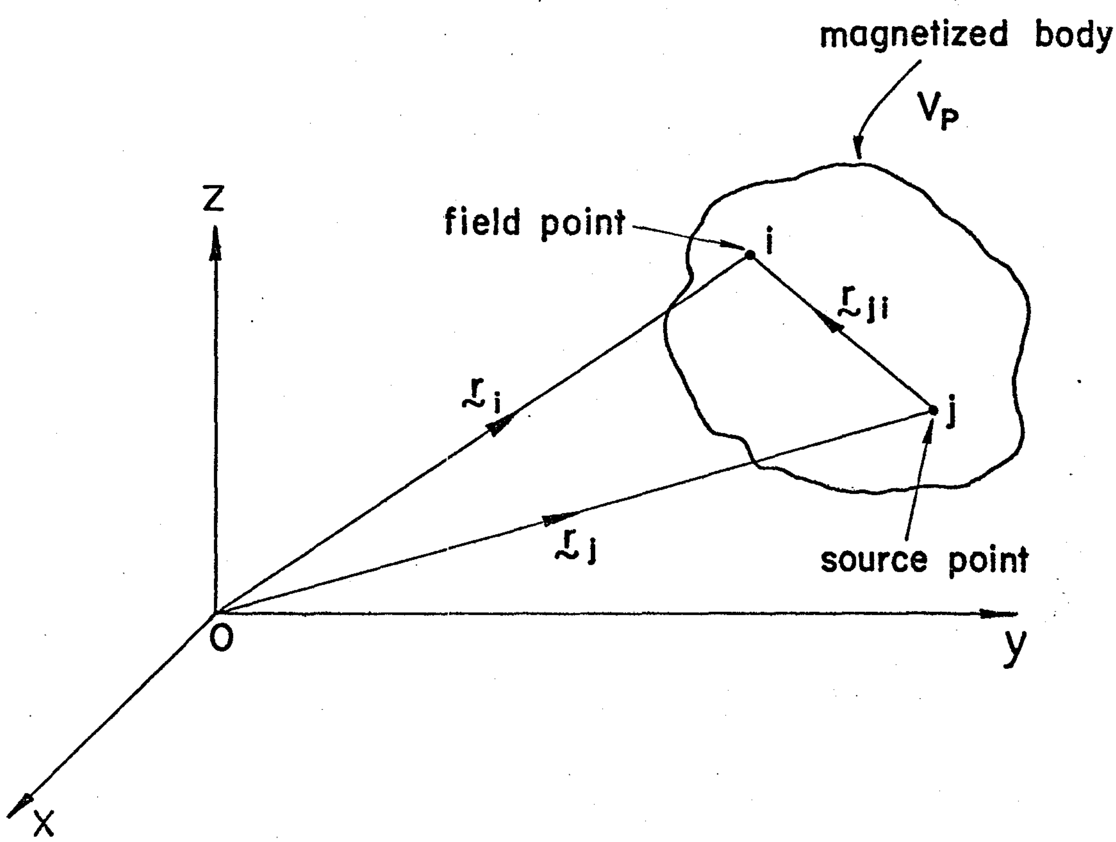

Figure 3.4 The coordinate system used to compute the demagnetizing field at a field point i due to the magnetization at a source point j.

where

$$\mathcal{D}_{k\ell}(\underset{\sim}{r}_i;\underset{\sim}{r}_j) \stackrel{\Delta}{=} \iint D_{k\ell}(\underset{\sim}{r}_i;\underset{\sim}{r}_j)\ dk_j d\ell_j \quad . \tag{3.31}$$

The two-dimensional demagnetizing field distribution as a function of the magnetization distribution, is thus given by (3.29) and (3.30).

3.4.3 Computation of the Exchange Field

Since a unit vector in the direction of the magnetization can be written as

$$\underset{\sim}{1}_M(\underset{\sim}{r}) \stackrel{\Delta}{=} \cos\,\theta_M(\underset{\sim}{r})\ \underset{\sim}{1}_x + \sin\,\theta_M(\underset{\sim}{r})\ \underset{\sim}{1}_y, \tag{3.32}$$

then the x and y components of the exchange field (see (3.17)) at point i are given by

$$H_{EX_x}(\underset{\sim}{r}_i) = \frac{2A_{EX}}{\mu_o\ M_s}\left[\frac{\partial^2}{\partial x^2} + \frac{\partial^2}{\partial y^2}\right] \cos\,[\theta_M(\underset{\sim}{r}_i)] \quad , \tag{3.33}$$

$$H_{EX_y}(\underset{\sim}{r}_i) = \frac{2A_{EX}}{\mu_o\ M_s}\left[\frac{\partial^2}{\partial x^2} + \frac{\partial^2}{\partial y^2}\right] \sin\,[\theta_M(\underset{\sim}{r}_i)] \quad , \tag{3.34}$$

where

$$\theta_M(\underset{\sim}{r}_i) \stackrel{\Delta}{=} \theta_M(x,\ y) \quad . \tag{3.35}$$

Following the analysis of Appendix C, (3.33) and (3.34) reduce to

$$H_{EX_x}(\underset{\sim}{r}_i) = \frac{2A_{EX}}{\mu_o\ M_s}\left\{ - \cos\,\theta_M(\underset{\sim}{r}_i)\ [\theta^2_{M_x}(\underset{\sim}{r}_i) + \theta^2_{M_y}(\underset{\sim}{r}_i)] \right.$$
$$\left. - \sin\,\theta_M(\underset{\sim}{r}_i)\ [\theta_{M_{xx}}(\underset{\sim}{r}_i) + \theta_{M_{yy}}(\underset{\sim}{r}_i)] \right\} , \tag{3.36}$$

$$H_{EX_y}(\underset{\sim}{r}_i) = \frac{2A_{EX}}{\mu_o M_s}\left\{ - \sin\theta_M(\underset{\sim}{r}_i)\,[\theta^2_{M_x}(\underset{\sim}{r}_i) + \theta^2_{M_y}(\underset{\sim}{r}_i)] \right.$$

$$\left. + \cos\theta_M(\underset{\sim}{r}_i)\,[\theta_{M_{xx}}(\underset{\sim}{r}_i) + \theta_{M_{yy}}(\underset{\sim}{r}_i)] \right\}, \tag{3.37}$$

where

$$\theta_{M_n}(\underset{\sim}{r}_i) \triangleq \frac{\partial}{\partial n}\left[\theta_M(\underset{\sim}{r}_i)\right], \tag{3.38}$$

$$\theta_{M_{nn}}(\underset{\sim}{r}_i) \triangleq \frac{\partial^2}{\partial n^2}\left[\theta_M(\underset{\sim}{r}_i)\right], \tag{3.39}$$

and n refers to x and y.

3.4.4 The Micromagnetic Algorithm

Following the analysis of Sections 3.2-3.4, a two-dimensional magnetization distribution $\underset{\sim}{M}(\underset{\sim}{r})$ in a permalloy element, placed in an applied field $\underset{\sim}{H}_A(\underset{\sim}{r})$, can be computed using the following steps:

Step 1 Define a mesh of N points over the permalloy as shown in Fig. 3.2(a) such that Δx and $\Delta y < 500$ Å.

Step 2 Set k = 1. Choose a tolerance ε for the termination criterion. Choose an under-relaxation factor β such that $\beta \ll 1$.

Step 3 Choose a suitable initial magnetization distribution $\{\underset{\sim}{M}^{(0)}(\underset{\sim}{r}_i),$ $i = 1, 2, \ldots, N\}$.

Step 4 Compute $\{\underset{\sim}{H}_A(\underset{\sim}{r}_i),\ i = 1, 2, \ldots, N\}$, using (3.21) and (3.23).

Step 5 Compute $\{\underset{\sim}{H}_D^{(k)}(\underset{\sim}{r}_i),\ i = 1, 2, \ldots, N\}$ using (3.29) and (3.30) and the results of Appendix B.

Step 6 Compute $\{\underset{\sim}{H}_{EX}^{(k)}(\underset{\sim}{r}_i),\ i = 1, 2, \ldots, N\}$ using (3.36) and (3.37) and the results of Appendix C.

Step 7 Compute $\{\underset{\sim}{H}_L^{(k)}(\underset{\sim}{r}_i),\ i = 1, 2, \ldots, N\}$ using (3.16) and $\{\theta_L^{(k)}(\underset{\sim}{r}_i),\ i = 1, 2, \ldots, N\}$ using

$$\theta_L^{(k)}(\underset{\sim}{r}_i) = \tan^{-1}\left[\frac{H_{L_y}^{(k)}(\underset{\sim}{r}_i)}{H_{L_x}^{(k)}(\underset{\sim}{r}_i)}\right] . \tag{3.40}$$

Step 8 Set $\theta_M^{(k)}(\underset{\sim}{r}_i) = \theta_L^{(k)}(\underset{\sim}{r}_i),\ i = 1, 2, \ldots, N.$

Step 9 Replace $\{\theta_M^{(k)}(\underset{\sim}{r}_i),\ i = 1, 2, \ldots,\}$ by an under-relaxed set using

$$\theta_M^{(k)}(\underset{\sim}{r}_i) \leftarrow \beta\ \theta_M^{(k)}(\underset{\sim}{r}_i) + (1-\beta)\ \theta_M^{(k-1)}(\underset{\sim}{r}_i), \qquad i = 1, 2, \ldots, N \tag{3.41}$$

Step 10 Compute the residual error

$$e^{(k)} = \max_{1\le i\le N} \Delta_i^{(k)} \quad , \tag{3.42}$$

where

$$\Delta_i^{(k)} \triangleq \left|\theta_M^{(k)}(\underset{\sim}{r}_i) - \theta_M^{(k-1)}(\underset{\sim}{r}_i)\right| \tag{3.43}$$

Step 11 Stop if $e^{(k)} < \varepsilon$. Set

$$\underset{\sim}{M}(\underset{\sim}{r}_i) = M_s\ \underset{\sim}{1}_M^{(k)}(\underset{\sim}{r}_i) \qquad , i = 1, 2, \ldots, N \quad , \tag{3.44}$$

Step 12 Set k = k+1. Go to Step 5.

3.4.5 Discussion

Step 3 of the above algorithm requires the choice of a suitable initial magnetization distribution. Since the magnitude of the magnetization vector is constant and equal to M_s everywhere in the permalloy, it is convenient to define a demagnetized initial distribution; otherwise, the demagnetizing field components will be very high and instability of the solution may occur.

The reason for using an under-relaxation factor β in Step 9 of the micromagnetic algorithm is that since the permalloy is a high permeability material, then small changes in $\underset{\sim}{M}(\underset{\sim}{r})$ can produce large changes in $\underset{\sim}{H}_D^{(k+1)}(\underset{\sim}{r})$ which could produce very large changes in $\underset{\sim}{M}^{(k+1)}(\underset{\sim}{r})$. Therefore, only very small changes are allowed in $\underset{\sim}{M}^{(k)}(\underset{\sim}{r})$ and this is controlled by using a very small under-relaxation factor.

The assumption in (3.44) imposes a certain condition on the cell size of the N-point mesh in the permalloy. The cell size should be small enough to simulate accurate micromagnetic dimensions. Since domain wall thickness in permalloy films are in the range of 0.05 to 0.1 μm, it is convenient to define a mesh with a cell size of about 200 Å. In a rectangular permalloy bar of dimensions 7.5 x 1.5 x 0.3 μm if one uses square cells of dimensions 200 x 200 Å, then a mesh of more than 28000 points is required. In addition to the large amount of computer memory necessary, a great deal of computer time is required to perform the micromagnetic algorithm with such a large number of points. However, it should be noted that the obtained magnetization distribution is a general one and accurately describes the domain and domain wall behavior in the permalloy.

It is noted that (Ishak and Della Torre 1978c) the computation of the field $\underset{\sim}{H}_D(\underset{\sim}{r})$ (Step 4) consumes most of the running time required for the algorithm. Therefore, one way of reducing the required computer time is to use a fine/coarse mesh configuration where the magnetization, the applied field and the exchange field are computed over the fine mesh and the demagnetizing field is evaluated over a coarser mesh. Interpolation procedures are then used to obtain the demagnetizing field components over the fine mesh.

Using a fine/coarse mesh configuration with 4681/561 points over a permalloy bar of dimensions 7.5 x 1.5 x 0.3 μm, it was found that, using a CDC-6400 computer, one iteration in the micromagnetic algorithm requires 60 seconds of computer time. About 60 iterations were required to converge to a residual error of 1%.

Due to computer memory and time limitations, it was decided to use another approach for the forward modeling problem. Nevertheless, the micromagnetic algorithm as described in Subsection 3.4.4 is the most general and accurate way of analyzing a ferromagnetic body, and will have to be used for analyzing submicron bubble propagation circuits.

3.5 A Continuum Model

3.5.1 Introduction

In this approach, the magnetization is assumed to be continuously distributed within each of the permalloy pattern elements. This is a macroscopic model which views the magnetization as the average of each individual domain magnetization. Therefore, the magnetization components are computed over a relatively coarse mesh. Since the exchange field decreases rapidly with the distance between neighboring points, it is reasonable to neglect the effect of the exchange energy on the total permalloy energy in a continuum model.

During the deposition of permalloy films for bubble circuit applications, a rotating deposition field, in the plane of the film, is applied to create essentially isotropic films, on a macromagnetic scale. In addition, most bubble circuits are fabricated using non-magnetostrictive films to eliminate the stresses between the permalloy layer and the garnet film. Thus, to a reasonable approximation, the permalloy energy can be written as

$$E_P = E_A + E_D \tag{3.45}$$

which means that the total local field at any point i in the permalloy will be composed of only the applied field and the demagnetizing field components.

Further, it is assumed that the magnetization distribution can be approximated by a discrete expansion coupled with a suitable interpolation scheme (George and Hughes 1976a)

$$M_x(\underset{\sim}{r}_i) = \sum_{j=1}^{N} M_x(\underset{\sim}{r}_j)\ I(i;j)\ , \tag{3.46}$$

$$M_y(\underset{\sim}{r}_i) = \sum_{j=1}^{N} M_y(\underset{\sim}{r}_j)\ I(i;j)\ , \tag{3.47}$$

where I(i;j) is an interpolant having the Kronecker delta form :

$$\begin{aligned} I(i;j) &= 1 \quad , \quad i = j \\ &= 0 \quad , \quad i \neq j \end{aligned} \tag{3.48}$$

Viewed from this point, the substitution of (3.46) and (3.47) into (3.27) and (3.28) yields

$$\begin{bmatrix} \underset{\sim}{H}_{D_x} \\ \underset{\sim}{H}_{D_y} \end{bmatrix} = \begin{bmatrix} C_{xx} & C_{xy} \\ C_{yx} & C_{yy} \end{bmatrix} \begin{bmatrix} \underset{\sim}{M}_x \\ \underset{\sim}{M}_y \end{bmatrix} \quad , \tag{3.49}$$

where

$$\underset{\sim}{H}_{D_k} \triangleq [H_{D_k}(\underset{\sim}{r}_1) \quad H_{D_k}(\underset{\sim}{r}_2) \; \cdots \; H_{D_k}(\underset{\sim}{r}_N)]^T \; , \tag{3.50}$$

$$\underset{\sim}{M}_{D_k} \triangleq [M_k(\underset{\sim}{r}_1) \quad M_k(\underset{\sim}{r}_2) \quad \cdots \quad M_k(\underset{\sim}{r}_N)]^T \; , \tag{3.51}$$

$$C_{k\ell} \triangleq \begin{bmatrix} C_{k\ell}(1,1) & C_{k\ell}(1,2) & \cdots & C_{k\ell}(1,N) \\ C_{k\ell}(2,1) & C_{k\ell}(2,2) & \cdots & C_{k\ell}(2,N) \\ \vdots & \vdots & & \vdots \\ C_{k\ell}(N,1) & C_{k\ell}(N,2) & \cdots & C_{k\ell}(N,N) \end{bmatrix} \quad , \tag{3.52}$$

$$C_{k\ell}(m,p) \triangleq \iint D_{k\ell}(\underset{\sim}{r}_m;\underset{\sim}{r}_n) \; I(p;n) \; dk_n d\ell_n \quad . \tag{3.53}$$

Since the elements of $C_{k\ell}$ depend only on the geometrical parameters of the permalloy, they are computed once, for each circuit, and used throughout the analysis of the circuit and for different applied field configurations. It is noted that the integrand in (3.53) is singular when m = n. Appendix B discusses the nature of this singularity and the procedure used to perform the integration when m=n. It is also noted that, generally, the matrix $C_{k\ell}$ is diagonally dominant which means that the demagnetizing field is almost in the opposite direction of the magnetization. A similar technique for computing the demangetizing field distribution has been used by Della Torre and

Kinsner (1973).

The magnetization in the permalloy is computed iteratively from an initial distribution $\underset{\sim}{M}^{(0)}(\underset{\sim}{r})$. Assuming a fixed bubble size and position, the two in-plane components of $\underset{\sim}{H}_A(\underset{\sim}{r})$, namely $\underset{\sim}{H}_T$ and $\underset{\sim}{H}_R(\underset{\sim}{r})$, and the demagnetizing field $\underset{\sim}{H}_D(\underset{\sim}{r})$ are computed using (3.21), (3.23) and (3.52), respectively. The total local field is, then, computed and a new magnetization distribution

$$\underset{\sim}{M}^{(k+1)}(\underset{\sim}{r}) = f[H_L^{(k)}(\underset{\sim}{r})] \; \underset{\sim}{1}_L^{(k)}(\underset{\sim}{r}) \tag{3.54}$$

is next computed where k refers to the iteration number and f determines the M-H_L relation for the permalloy. The process is repeated until a final magnetization distribution is obtained according to a predetermined accuracy.

Ma (1976) showed that permalloy patterns for bubble circuit applications possess a wide variety of M-H_A characteristics. In general, the magnetization varies nonlinearly with the applied field and, hence, with the local field (Cullity 1972). This is in agreement with the results of Doyle and Casey (1972) and Krinchik, Chepurova, Shamatov, Raev and Andreev (1975). They measured the magnetization loops for various permalloy films and came to the conclusion that even when M varies linearly with H_A for low applied fields, it asymptotically approaches M_s for large fields. The point at which M no longer increases linearly with H_A was difficult to measure. However it did vary in different samples from 0.3 M_s to 0.9 M_s.

A wide variety of functions were tested to simulate the permalloy M-H_L characteristics and it was found that the magnetization converged to reasonable values in all cases. The M-H_L relation

$$M(\underset{\sim}{r}) = M_s \left[t_1 \frac{H_L(\underset{\sim}{r})}{H_t} \right] \quad , \; H_L(\underset{\sim}{r}) \leq H_t, \tag{3.55}$$

$$M(\underset{\sim}{r}) = M_s \left\{ t_1 + \frac{2}{\pi} (1-t_1) \tan^{-1} \left[\eta \frac{H_L(\underset{\sim}{r})}{H_t} \right] \right\}, \; H_L(\underset{\sim}{r}) \geq H_t, \tag{3.56}$$

where t_1, H_t and η are the parameters shown in Fig. D.2, is found to be general enough that by controlling these parameters, a wide variety of functions can be obtained. Typical values for t_1, H_t and η are 0.5, 1000 A/m and $\pi/2$, respectively. Appendix D sketches various other functions together with their properties.

3.5.2 The Magnetization Algorithm

The iterative procedure to compute the magnetization distribution in a permalloy body, at a fixed bubble diameter and position, can be summarized in the following steps (Ishak and Della Torre 1978a):

Step 1 Define a suitable mesh of N points over the permalloy body.

Step 2 Compute the elements of the matrices C_{xx}, C_{xy}, C_{yx} and C_{yy} in (3.49) using the procedure outlined in Appendix B.

STEP 3 **Set** $k = 1$. Choose a tolerance vector $\underset{\sim}{\varepsilon}$ for the termination criterion. Choose a suitable under-relaxation factor β. Recommended values are in the range $0.03 < \beta < 0.05$. Choose a suitable function f to represent the M-H_L characteristics as shown in (3.55), (3.56) and Appendix D.

Step 4 Compute $\{\underset{\sim}{H}_R(\underset{\sim}{r}_i),\ i = 1, 2, \ldots, N\}$ using (3.23).

Step 5 Compute $\{\underset{\sim}{H}_A(\underset{\sim}{R}_i),\ i = 1, 2, \ldots, N\}$ using (3.21).

Step 6 Define a suitable initial distribution $\{\underset{\sim}{M}^{(0)}(\underset{\sim}{r}_i),\ i=1,2,\ldots,N\}$. For example, use (3.54) replacing $\underset{\sim}{H}_L(\underset{\sim}{r})$ by $\underset{\sim}{H}_A(\underset{\sim}{r})$.

Step 7 Compute $\{\underset{\sim}{H}_D^{(k)}(\underset{\sim}{r}_i),\ i = 1, 2, \ldots, N\}$ using (3.49).

Step 8 Compute $\{\underset{\sim}{H}_L^{(k)}(\underset{\sim}{r}_i),\ i = 1, 2, \ldots, N\}$ using (3.19).

Step 9 Compute $\{\underset{\sim}{M}^{(k)}(\underset{\sim}{r}_i),\ i = 1, 2, \ldots, N\}$ using (3.54).

Step 10 Replace $\{\underset{\sim}{M}^{(k)}(\underset{\sim}{r}_i),\ i = 1, 2, \ldots, N\}$ by an under-relaxed set using

$$\underset{\sim}{M}^{(k)}(\underset{\sim}{r}_i) \leftarrow \beta\, \underset{\sim}{M}^{(k)}(\underset{\sim}{r}_i) + (1-\beta)\underset{\sim}{M}^{(k-1)}(\underset{\sim}{r}_i), \quad i = 1, 2, \ldots, N. \tag{3.57}$$

Step 11 Compute the residual error

$$\underset{\sim}{e}^{(k)} = [m_x^{(k)} \quad m_y^{(k)}]^T \tag{3.58}$$

where

$$m_n^{(k)} \triangleq \sum_{i=1}^{N} \left[\frac{M_n^{(k)}(\underset{\sim}{r}_i)-M_n^{(k-1)}(\underset{\sim}{r}_i)}{M_n^{(k)}(\underset{\sim}{r}_i)}\right]^2, \tag{3.59}$$

Step 12 Stop if $\underset{\sim}{e}^{(k)} < \underset{\sim}{\varepsilon}$. Set

$$\underset{\sim}{M}(\underset{\sim}{r}_i) = \underset{\sim}{M}^{(k)}(\underset{\sim}{r}_i),\ i = 1, 2, \ldots, N\ . \tag{3.60}$$

Step 13 Set $k = k+1$. Go to Step 7.

3.5.3 Discussion

Following the argument in Subsection 3.4.4, a very small under-relaxation factor β should be used to avoid oscillation and/or divergence in the numerical process. On the other hand, using an extremely small value for β will result in a slow convergence. Therefore, an optimization of β is desired to affect a stable solution as well as a reasonably fast convergence.

Figure 3.5 shows the effect of the under-relaxation factor β on the number of iterations required to achieve a residual error of less than 0.1% in the magnetization components of a 105 point mesh defined over a 15 x 3 x 0.4 μm rectangular permalloy bar. It was found in general, that the optimum value for β is problem dependent which decreases as the number of points, in the iteration mesh, increases. Moreover, the value of β is inversely proportional to the slope of the M-H_L characteristics which is in agreement with the results of Ortenburger (1977). For most of the problems treated in this thesis it is noted that $0.03 < \beta < 0.05$ results in reasonable computer times as well as numerical stability in the iterative procedure.

In Step 9 of the magnetization algorithm, the x and y components of the magnetization vector everywhere in the permalloy are computed. By neglecting the cross-coupling terms, each component can be computed separately. Ma (1976) showed that this is reasonable for ferromagnetic bodies and Ortenburger, Cole and Potter (1977) used separate analysis for the x and y components of the magnetization in high permeability recording media.

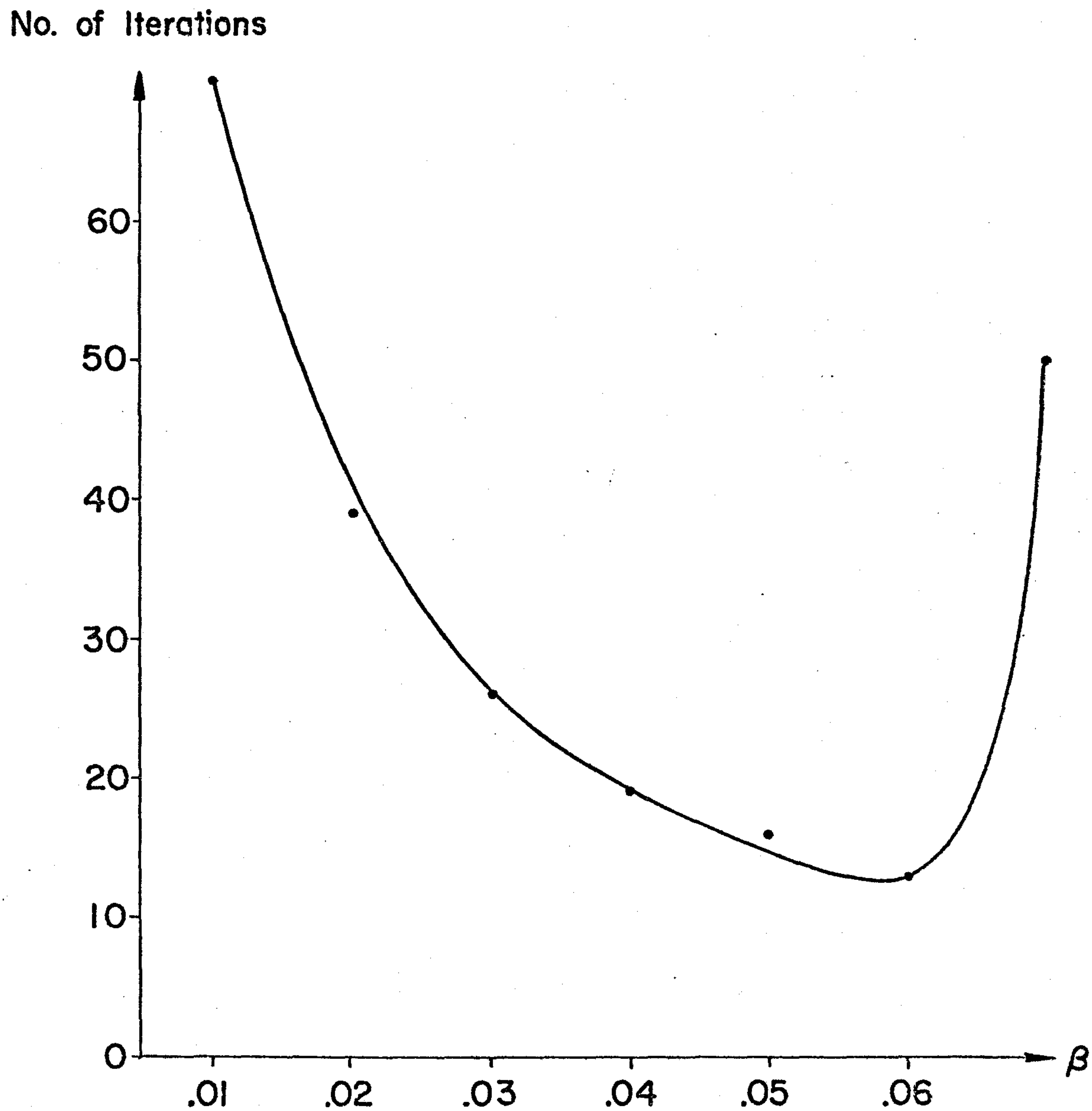

Figure 3.5 Effect of the under-relaxation factor on the number of iterations required in the magnetization algorithm.

The residual error defined in (3.56) is the normalized total error in the magnetization components. Alternatively, the maximum change in these components can be used to terminate the iteration process, that is

$$\underset{\sim}{e}^{(k)} = [e_x^{(k)} \quad e_y^{(k)}]^T, \tag{3.61}$$

where

$$e_n^{(k)} = \max_{1 \leq i \leq N} \frac{|M_n^{(k)}(\underset{\sim}{r}_i) - M_n^{(k-1)}(\underset{\sim}{r}_i)|}{M_n^{(k)}(\underset{\sim}{r}_i)}, \tag{3.62}$$

3.6 Examples

Figure 3.6 shows the demagnetizing factors (see Appendix B) of a 15 x 3 x 0.4 μm permalloy bar calculated from the matrix of (3.49) using a cubic-spline interpolation function in (3.46) and (3.47). Comparison to the case of a linear interpolation is also given. The magnetization distributions in a 7.5 x 1.5 x 0.3 μm permalloy bar when placed in a uniform in-plane field are shown in Fig. 3.7 together with its demagnetizing factors. It is noted that the magnetization distribution reflects the demagnetizing factor distribution.

The effect of the position of a bubble domain on the magnetization distributions in a rectangular bar is given in Fig. 3.8. The maximum magnetization, for any bubble position, usually occurs near the bubble perimeter due to the bubble's stray field. Figure 3.9 shows the demagnetizing field distributions and the magnetization distributions along the center line of a rectangular permalloy bar for two different bubble positions. It is noted that the maximum of the

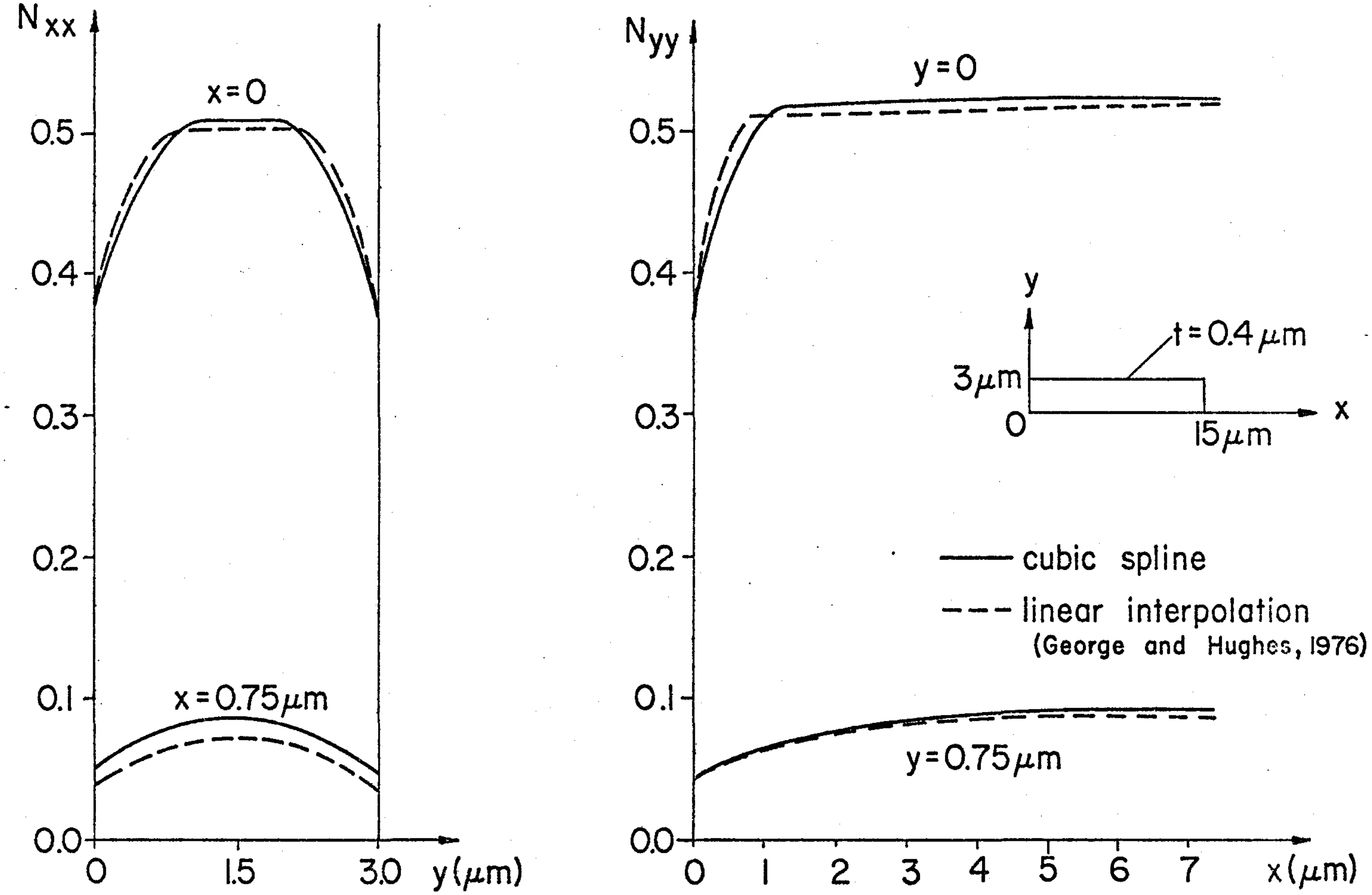

Figure 3.6 Demagnetizing factor distributions of a rectangular permalloy bar of dimensions 15 x 3 x 0.4 μm (shown in the inset). Solid lines refer to cubic spline interpolation (see (3.46) and (3.47)) and dashed lines to linear interpolation (George and Hughes 1976a).

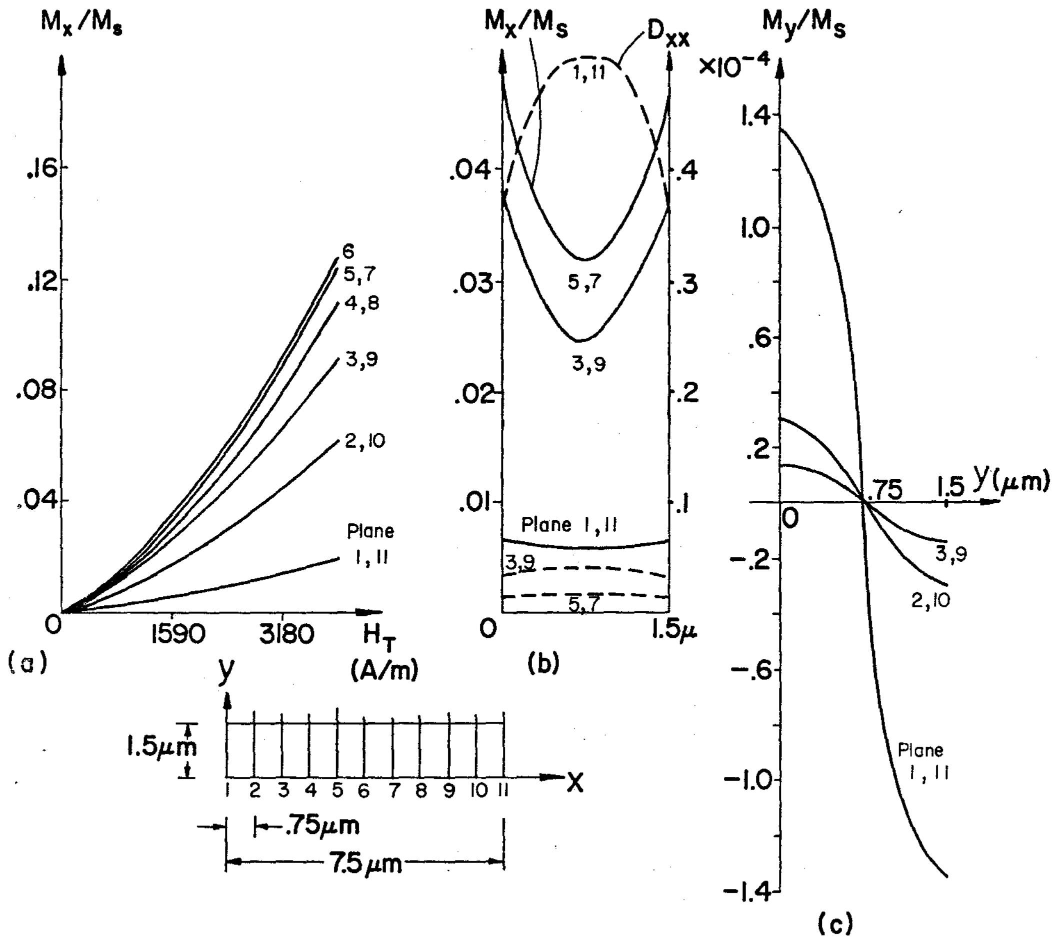

Figure 3.7 The magnetization distributions in a rectangular permalloy bar of dimensions 7.5 x 1.5 x 0.3 μm: (a) x-component of the magnetization as a function of H_T, (b) x-component as a function of y and the demagnetizing factors and (c) y-component of the magnetization as a function of y.

magnetization occurs at the minimum of the demagnetizing field.

To compare the results of the magnetization algorithm with results of models of other workers, the average magnetization distributions along the x and y axes of a 15 x 3 x 0.4 μm permalloy bar are computed and plotted as shown in Fig. 3.10. Since the present model uses a finite value for the permalloy susceptibility, it yields relatively lower magnetization values than those of the infinite susceptibility model of George and Hughes (1976a).

Both symmetric and asymmetric half-disk circuits are analyzed to show the capabilities of the model regarding the handling of complicated permalloy shapes. Figure 3.11 illustrates the demagnetizing factor distributions of a symmetric half-disk and Fig. 3.12 shows the demagnetizing field and the magnetization distributions at two different cross-sections of a two-period asymmetric half-disk circuit. Since characteristics of half-disk circuits have not been published, it is not possible to compare the results of Figs. 3.11 and 3.12 to experimental data. However, in Chapter 4, it will be shown that, using the magnetization algorithm, some propagation characteristics of half-disk circuits are obtained and that they are in a good agreement with experimental observations.

The FORTRAN IV program used to test the magnetization algorithm of Section 3.5 was developed on a CDC-6400 computer (Ishak and Della Torre 1978b). The program consists of two main parts. The first part accepts the permalloy pattern definitions, constructs a suitable mesh of N points over this pattern, computes the matrices of (3.52) and stores

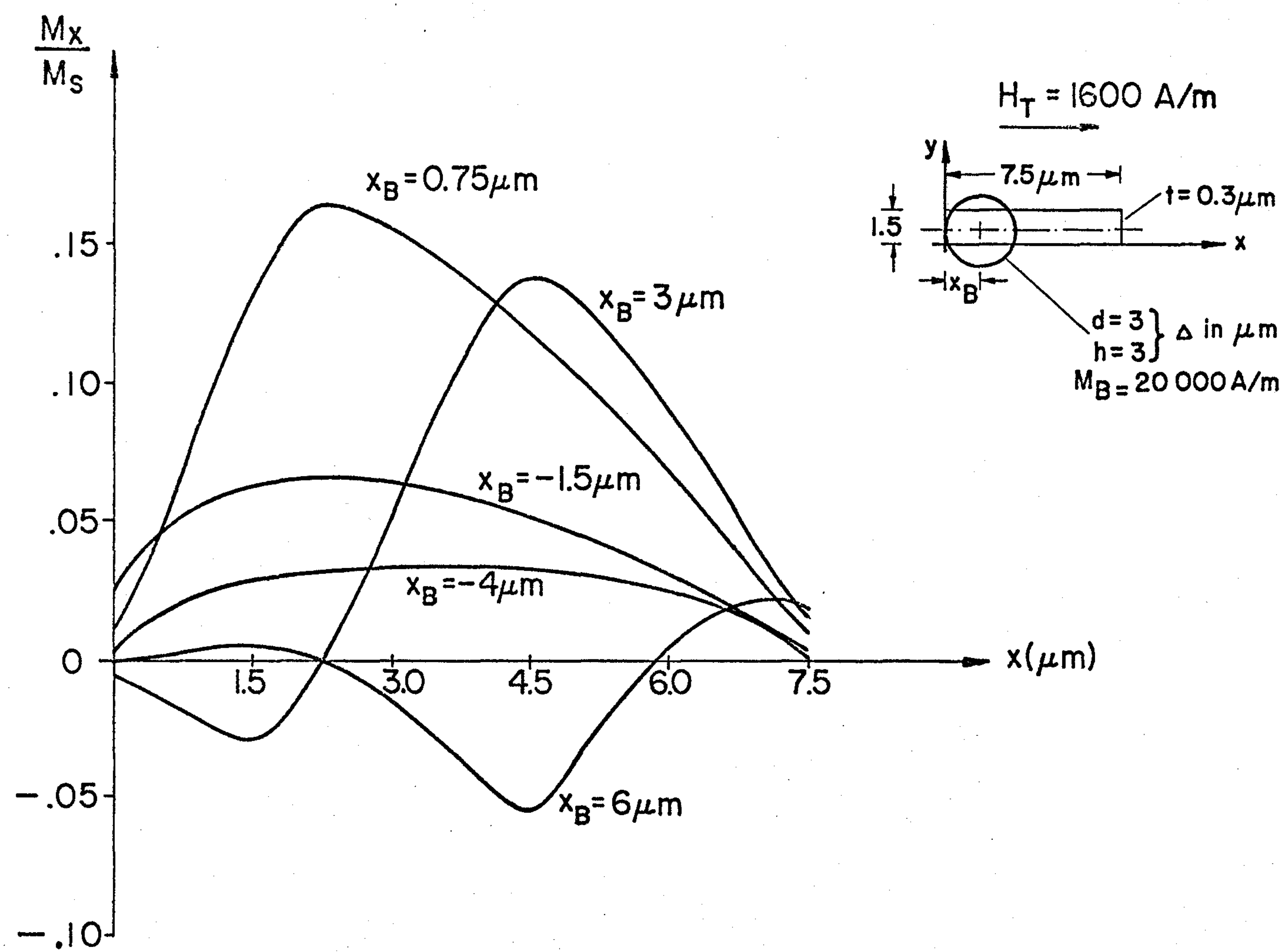

Figure 3.8 Effect of the bubble position on the magnetization distribution along the center line of a rectangular permalloy bar of dimensions 7.5 x 1.5 x 0.3 μm. The maximum magnetization occurs at the bubble perimeter.

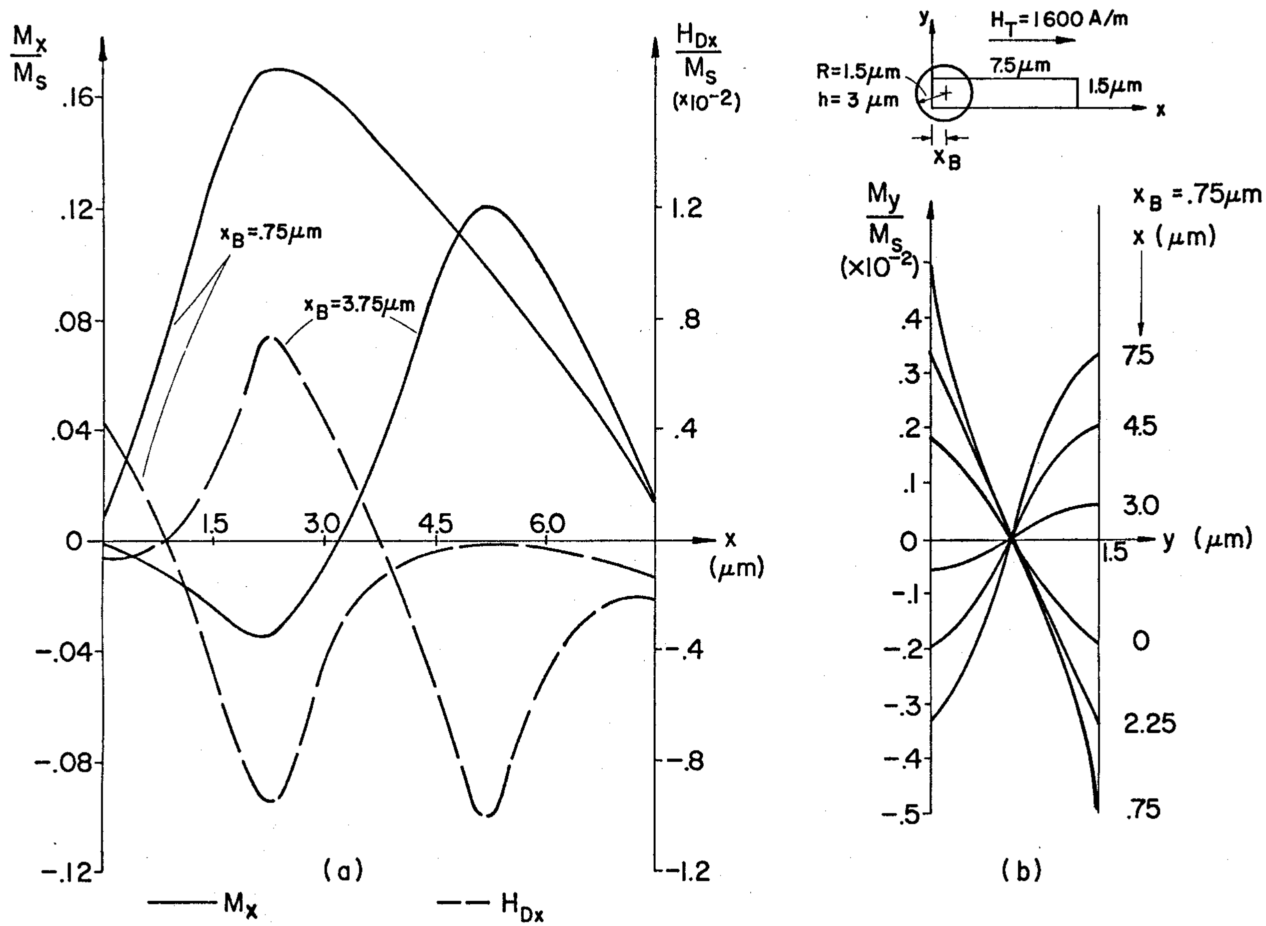

Figure 3.9 The x-component of the demagnetizing field and the magnetization distribution along the center line of a rectangular permalloy bar of dimensions 7.5 x 1.5 x 0.3 μm (a) for two bubble positions and (b) y-component of the magnetization as a function of y.

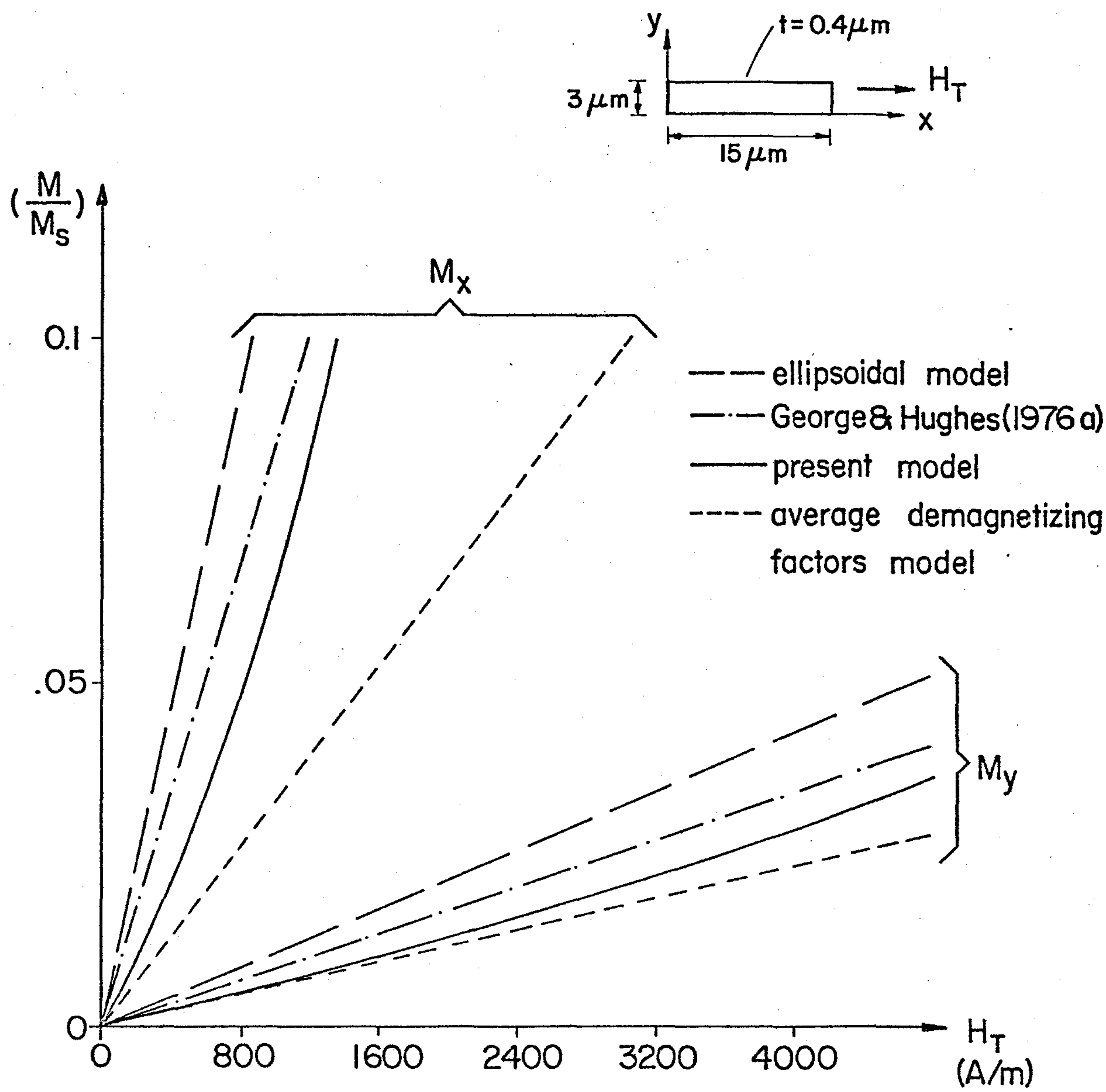

Figure 3.10 Comparison between the results of the magnetization algorithm and the results of models of other workers.

them on a magnetic disc. In the second part, the permalloy-bubble configurations are read and the computation proceeds to determine $\underset{\sim}{M}(\underset{\sim}{r})$ for each configuration.

A memory storage of about 55 K words, using a CDC-6400 computer, is required for each part of the program for a mesh of 300 points. It is noted that the computation time required for the analysis in the second part of the program depends on the choice of the initial magnetization distribution $\underset{\sim}{M}^{(0)}(\underset{\sim}{r})$. However, certain criteria can reduce this time appreciably when the analysis involves different bubble positions. Starting with an initial bubble position, any initial distribution $\underset{\sim}{M}^{(0)}(\underset{\sim}{r})$ can be assumed, preferably based on $\underset{\sim}{H}_A(\underset{\sim}{r})$, and the final magnetization distribution $\underset{\sim}{M}(\underset{\sim}{r})$ is computed using the magnetization algorithm. For the next bubble position, $\underset{\sim}{M}(\underset{\sim}{r})$ (of the previous position) is used as an initial distribution. If the consecutive change in the bubble position, along the permalloy, is not large, a reduction in computer time is obtained using this criterion.

For a half-disk circuit, with a mesh of 91 points, 15 seconds of computer time are required for the analysis in the second part of the program (using $\beta = 0.045$) for the first bubble position. When the bubble moves along the perimeter of the disk, in steps of about 1 μm, only 5 seconds are required for each consecutive bubble position. The entire analysis of the two parts of the program for the half-disk circuit for 10 bubble postions and 10 in-plane field orientations, takes about 11 minutes of computer time.

A comparison between the computer time and memory requirements to

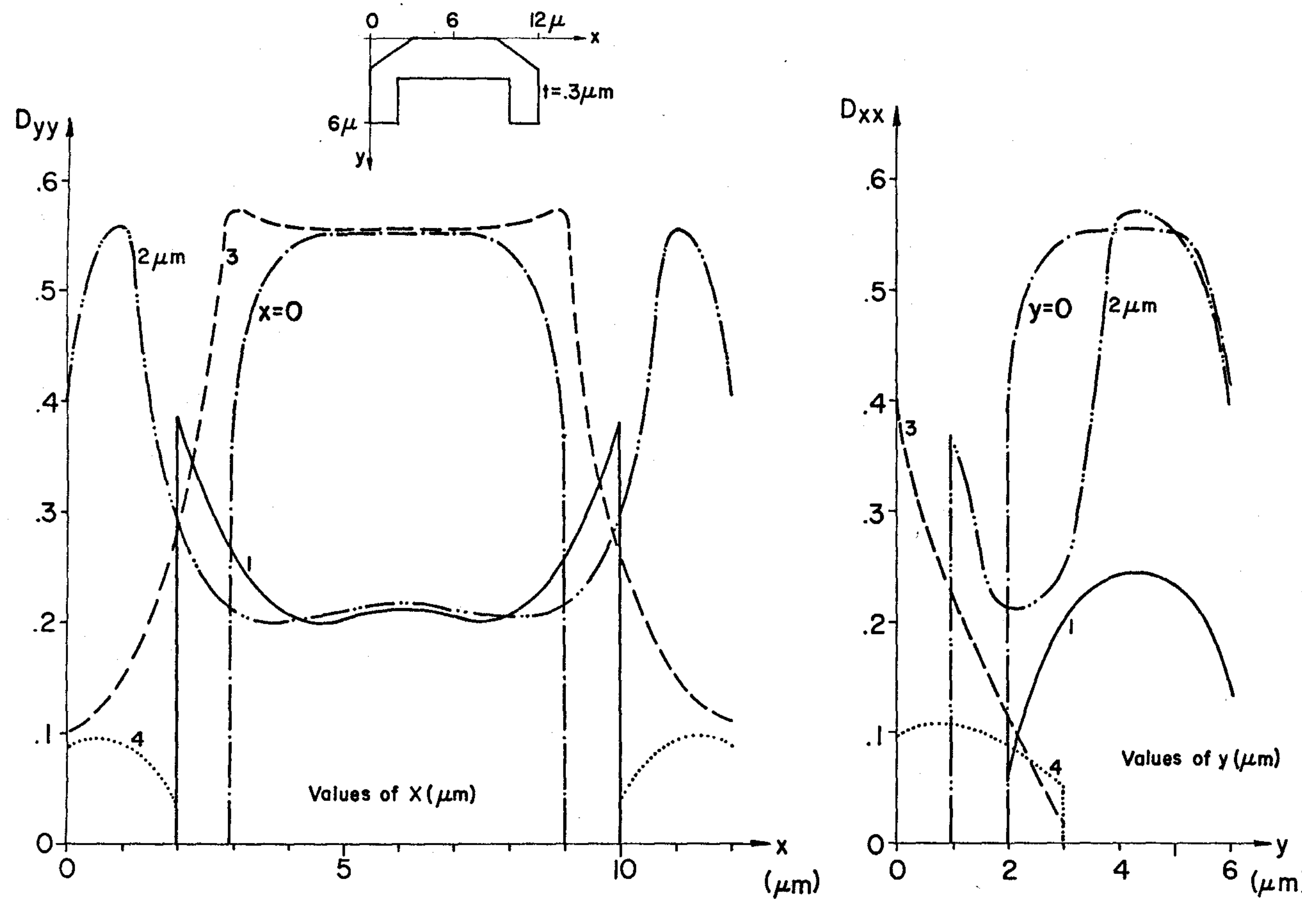

Figure 3.11 The demagnetizing factor distribution at five different cross-sections in a symmetric half-disk (see the inset).

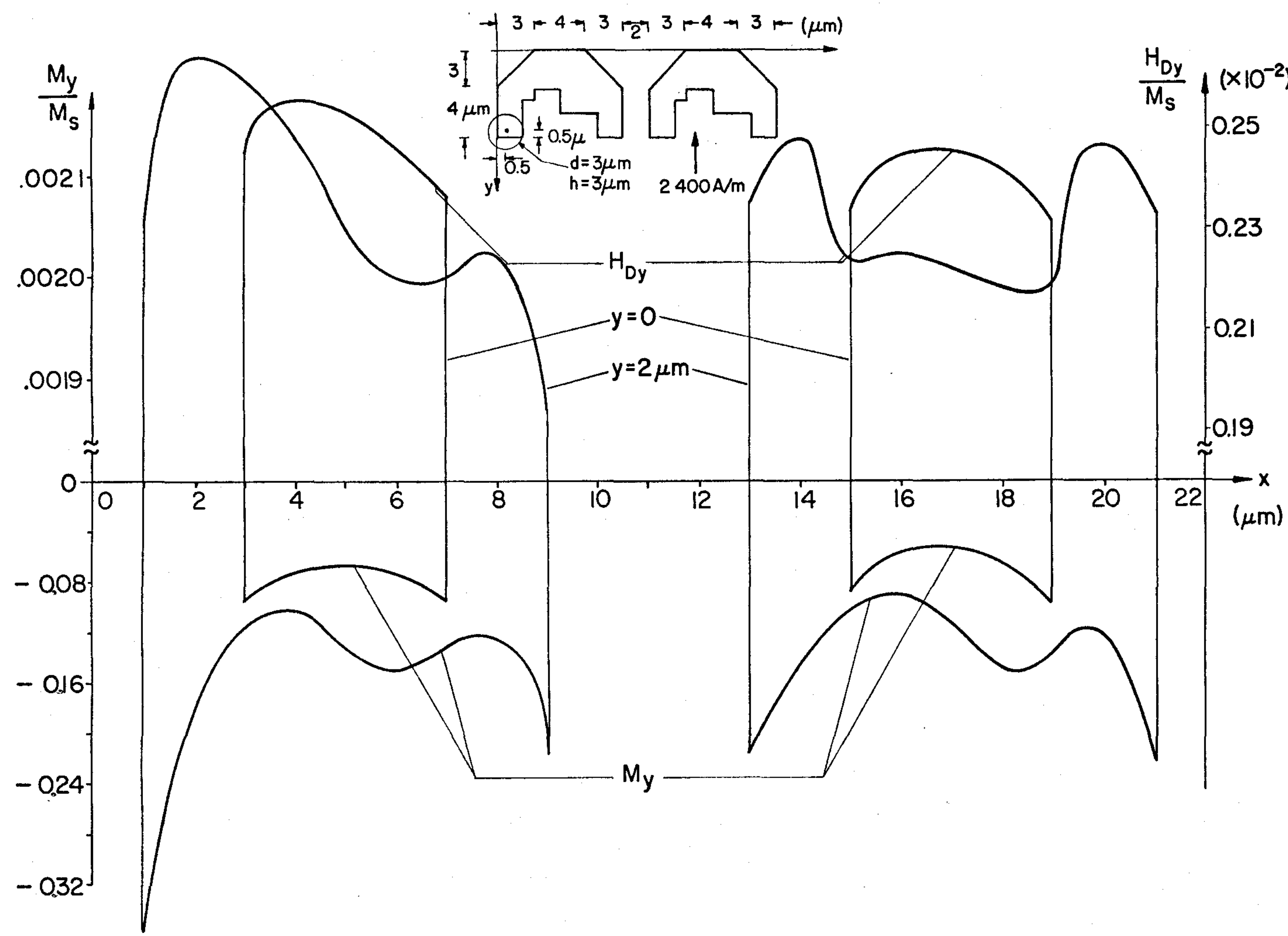

Figure 3.12 The y-component of the demagnetizing field and the magnetization distribution at two different cross-sections in two periods of asymmetric half-disk circuit in the presence of a bubble and an in-plane field.

TABLE 3.1

COMPARISON BETWEEN THE COMPUTER TIME AND MEMORY REQUIREMENTS FOR THE PRESENT MODEL AND THE MODEL BY GEORGE AND HUGHES (1976a)

PARAMETER	PRESENT MODEL (1)	GEORGE AND HUGHES' MODEL (2)
COMPUTER TIME (MIN)	11	3
COMPUTER MEMORY (K WORDS)	55 (Part 1) 55 (Part 2)	-- (3)

Number of points in the mesh, N = 100

Number of field orientations = 10

Number of bubble positions = 10

(1) Using a CDC-6400 computer.

(2) Using an IBM-370/168 computer.

(3) In a private communication with P.K. George, he indicated that he used an IBM-370/168 with 800 K Byte memory.

Note: The IBM-370/168 computer is about 4 to 10 times faster than the CDC-6400 computer (Fleming 1978).

analyze a typical bubble circuit is shown in Table 3.1 for the present model and the model of George and Hughes (1976a). Taking into account the speed factors of the two computers used in the analysis of the two models, it is seen that the present model requires less computer time and memory.

3.7 Conclusions

The micromagnetic algorithm of Subsection 3.4.4 can be used to accurately analyze submicron bubble circuits since it takes into account all possible energy terms. This algorithm is also applicable for studying other kinds of memory circuits such as thin film memories.

Having an arbitrary two dimensional permalloy layout in a general nonuniform applied field, the magnetization algorithm of Subsection 3.5.2 is an efficient means of computing the demagnetizing field and the magnetization distributions in the permalloy. The inclusion of the permalloy nonlinear characteristics, through the use of an experimentally determined M-H_L relation, allows more realistic analysis of bubble circuits.

Proper choice of the under relaxation factor β and the initial magnetization distribution $\underset{\sim}{M}^{(0)}(\underset{\sim}{r})$ results in appreciable saving in computation times.

CHAPTER 4

ANALYSIS OF PROPAGATION CIRCUITS AND BUBBLE SIZE FLUCTUATIONS

4.1 Introduction

The model described in Chapter 3 is used for analysis of various propagation structures and the results are presented in Sections 4.2-4.4 of this chapter. These include rectangular bars, chevrons and half-disks. The potential well distributions, for these circuits, are computed and plotted as functions of the bubble position. Various conclusions are drawn and used to characterize each individual circuit. The results for rectangular bars are compared to the results of other existing models.

Experimental observations show that a bubble domain trapped at the end of a permalloy element has a different variation of diameter versus bias field than does a free isolated bubble (Chang 1975, Almasi and Lin 1976 and George and Hughes 1976b). The interpretation of this is that the permalloy changes the magnetostatic energy of the bubble domain by locally modifying the bias field acting on the bubble. In other words, the permalloy acts as a potential energy well for the bubble. Depending on the direction of the rotating in-plane field, this potential well is either decreased or increased. This means that in actual propagation circuits, the bubble diameter might be either larger or smaller than that of a free bubble for the same bias field.

Since bubble domains are stable only over a certain range of the bias field (Thiele 1969), it is important to avoid stripping-out or collapsing a trapped bubble in order to prevent anomalous propagation and loss of information, respectively. Thus any serious approach to the dynamics of bubble circuits should at least consider bubble size fluctuations.

Using the continuum model of Chapter 3, a new algorithm for computing the bubble size fluctuations is developed and presented in Section 4.5 of this chapter. The results obtained using this algorithm for rectangular permalloy bars are compared to experimental data by Jones and Enoch (1974).

4.2 The Potential Well

If we assume the zero energy level for the permalloy to be the energy of the configuration without the bubble and the in-plane field, then the permalloy energy, E_p, can be interpreted as the change in the energy when the in-plane field is applied and the bubble is introduced. See (3.1). Using the magnetization algorithm of Section 3.5, $\underset{\sim}{M}(\underset{\sim}{r})$ and $\underset{\sim}{H}_D(\underset{\sim}{r})$ can be computed for an arbitrary shaped permalloy circuit and hence E_p, using (3.45). The new distribution of magnetic charges inside and on the surface of the magnetized permalloy produces a local z-directed field, $\underset{\sim}{H}_z$, where the z-axis is normal to the permalloy plane as shown in Fig. 3.1. The magnitude of $\underset{\sim}{H}_z$, that is the potential well depth, H_z, is obtained by normalizing E_p to twice the bubble's magnetic moment m_B (Kinsner 1973 and George and Archer 1973). Thus

$$\underset{\sim}{H}_z = \frac{E_p}{2m_B} \underset{\sim}{1}_z , \qquad (4.1)$$

where

$$m_B = (\mu_o M_B) \left(\frac{\pi}{4} d^2 h \right) , \qquad (4.2)$$

This field, H_z, locally modifies the bias field, H_B, acting on the bubble. Since the bubble will move towards the position of a lower bias field, the potential well distribution of a permalloy circuit can be used to determine how the bubble moves along the propagation track.

4.3 Analysis of Bubble Circuits

4.3.1 Rectangular Bars

The reason for analyzing rectangular permalloy bars is that they are considered one of the basic building blocks in many propagation circuits such as T-I, Y-I, X-I, parallel-bars and channel-bars circuits. Potential well profiles for T-I, chevron and Y-I circuits have been developed by Kinsner (1974).

Figure 4.1 shows the potential well distribution along the center line of a rectangular bar under the influence of a bubble's stray field and two different in-plane field values. The maximum potential well depth (minimum $\underset{\sim}{H}_z$) does not occur at the edge of a bar but rather for this geometry about 0.75 μm inside it. This fact is experimentally verified by looking at the position of the center of a trapped bubble domain under a bar (Jones and Enoch 1974). The nonlinearity of the permalloy is evident in that doubling the applied field does not double

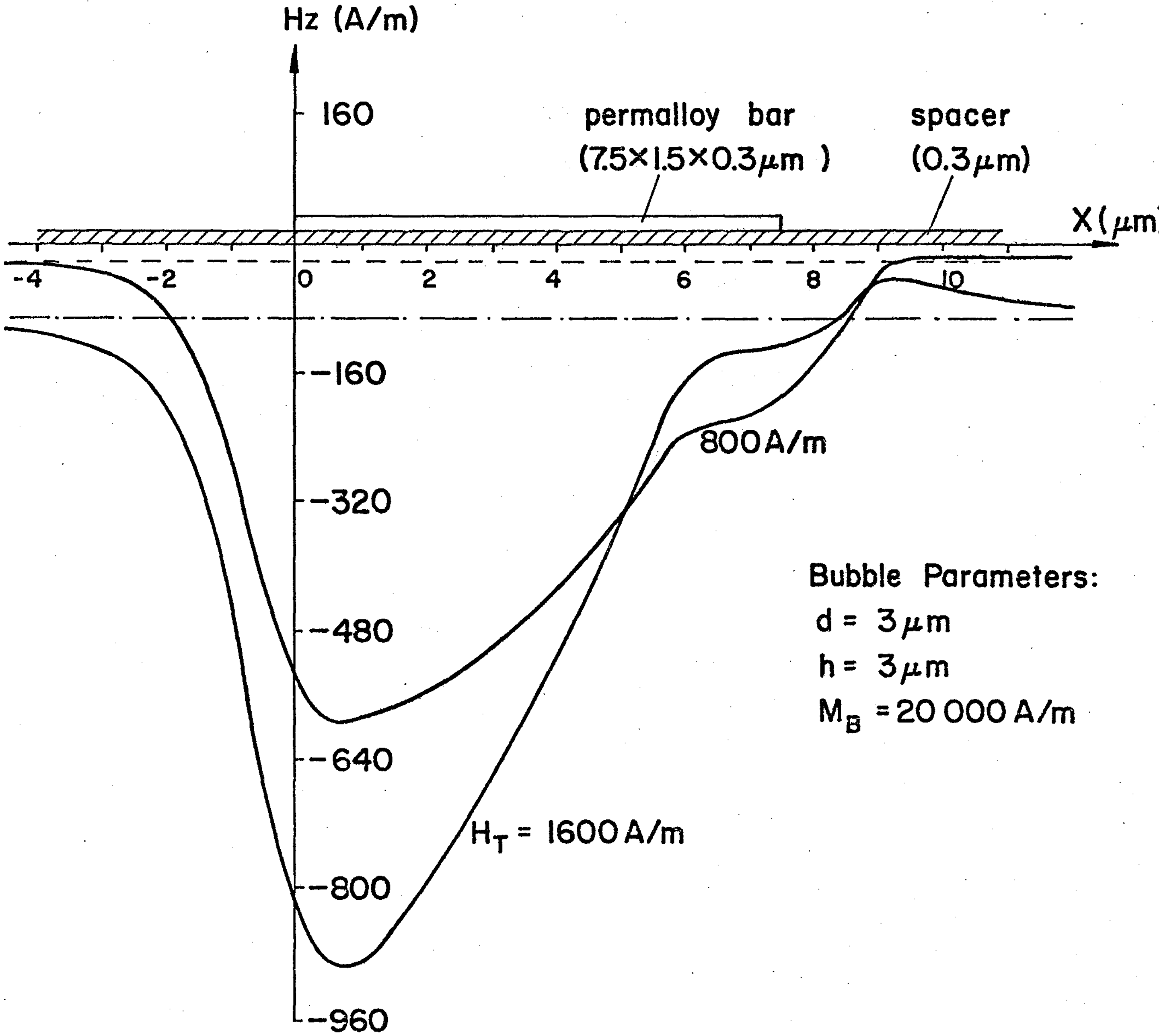

Figure 4.1 The potential well distribution along the center line of a rectangular permalloy bar of dimensions 7.5 x 1.5 x 0.3 μm for two different in-plane field values in the positive x-directions.

the well depth.

Comparison to the results of George and Hughes (1976b) is shown in Fig. 4.2 for a rectangular permalloy bar of dimensions 15 x 3 x 0.4 μm. Again the use of an infinite permeability in their model results in a relatively larger potential well depth. Nevertheless, the profiles of the potential well are similar and the minima of both distributions occur at about 1.5 μm inside the bar. A two-dimensional potential well profile for the same bar under the same applied field configuration is shown in Fig. 4.3 where the well depths corresponding to the contours labelled E and P are 0 A/m and -800 A/m, respectively with steps of -75 A/m for the contours in-between.

The field H_z is plotted as a function of bubble diameter in Fig. 4.4 for a 7.5 x 1.5 x 0.3 μm rectangular bar with a bubble sitting on the end as shown in the inset. Because the curves in Fig. 4.4 are not flat, trapped bubble strip-out and collapse diameters will differ from the free bubble values. It is noted that for a given bubble diameter, the potential well depth increases as the in-plane field increases. Moreover, this increase usually becomes greater as the bubble diameter decreases which is attributed to the higher bubble's stray field. A detailed algorithm for computing the trapped bubble characteristics is presented in Section 4.4.

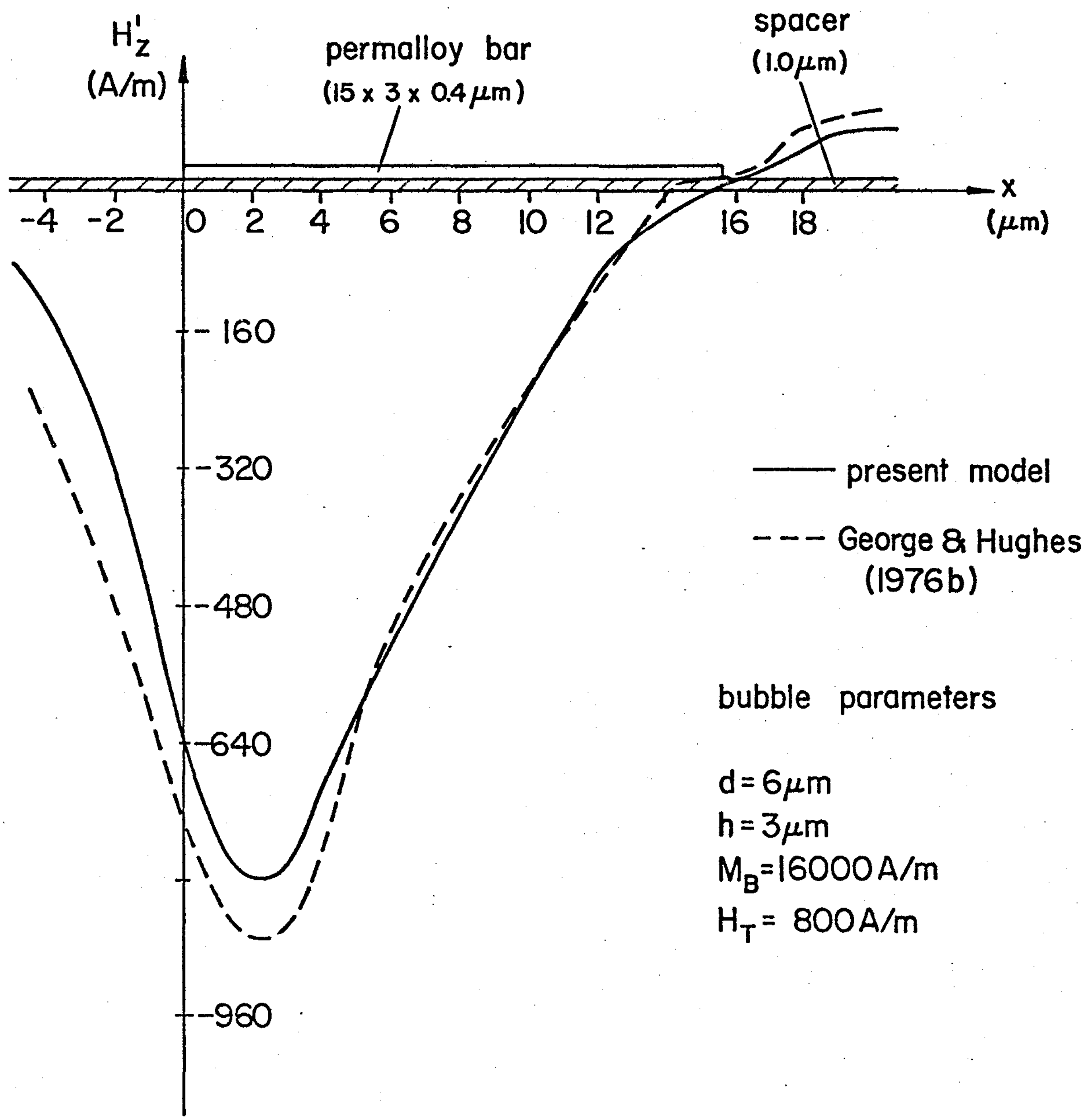

Figure 4.2 Comparison between the results of the present model and the results of George and Hughes (1976b) for a rectangular permalloy bar of dimensions 15 x 3 x 0.4 μm.

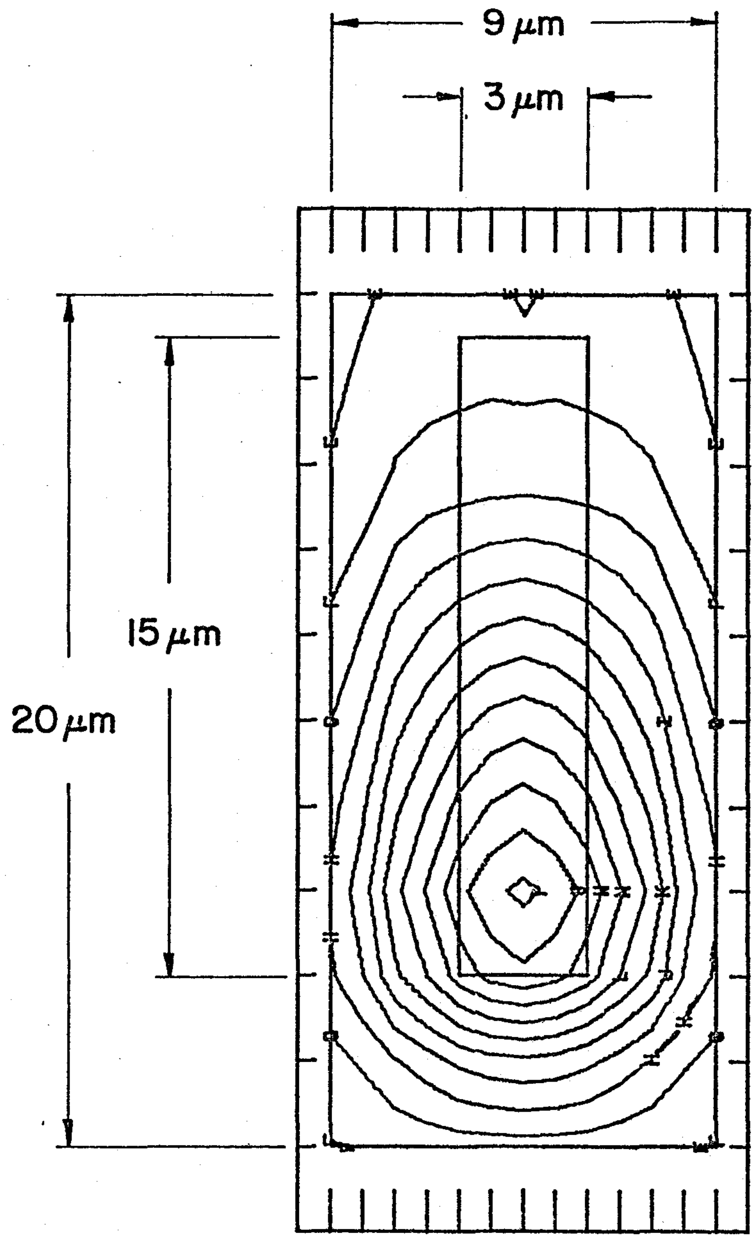

Figure 4.3 Two-dimensional potential well profile for a rectangular permalloy bar of dimensions 15 x 3 x 0.4 μm. The contours labelled P and E correspond to H_z = -800 A/m and 0 A/m, respectively.

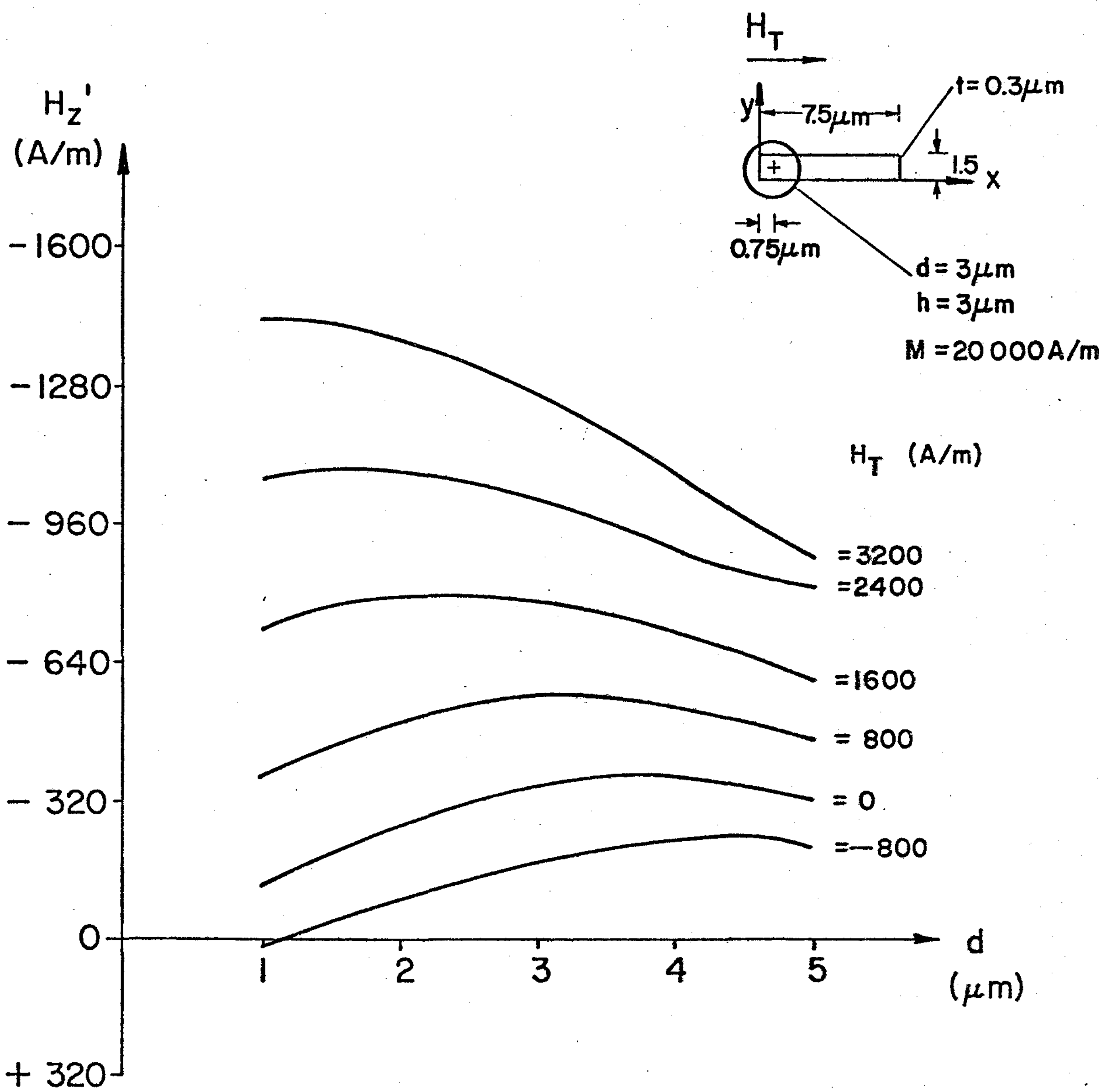

Figure 4.4 Effect of bubble diameter on the potential well depth along the center line of a rectangular permalloy bar of dimensions 7.5 x 1.5 x 0.3 μm.

4.3.2 Chevron Circuits

The problem with symmetric chevrons shown in Fig. 4.5 as propagation circuits is that the bubble does not move appreciably from position 1 to position 2 until the in-plane field, $\underset{\sim}{H}_T$, rotates almost 60^{o} from the the horizontal (dotted curve). This is verified experimentally in the work of Almasi and Lin (1976). Therefore, nonuniform propagation results along the arms of the chevron and the propagation margins (H_T versus H_B curves) are unacceptable for efficient operation. Figure 4.5 illustrates such a drawback where the potential well distributions along the bubble path in a 90^{o} chevron are shown for 6 different in-plane field orientations. The bubble's center position, corresponding to the minimum H_z, stays essentially at point 1 until θ is more than 60^{o} (Della Torre and Ishak 1978).

The asymmetric chevron circuit offers some advantages over the symmetric chevron circuit. This can be seen by comparing the potential well distributions of Fig. 4.6 (for the asymmetric case) to those of Fig. 4.5. It can be seen that, in general, $\partial H_z/\partial X$ in the former are higher than those in the latter, where X refers to the bubble position. Since the gradient $\partial H_z/\partial X$ is proportional to the speed of the bubble (Thiele 1969) it is advantageous to use a propagation circuit with large $\partial H_z/\partial X$. Moreover, the graph for $\theta = 60^{o}$ in Fig. 4.6 shows a minimum substantially away from point 1. This results in a more uniform propagation than in the case of the symmetric chevron.

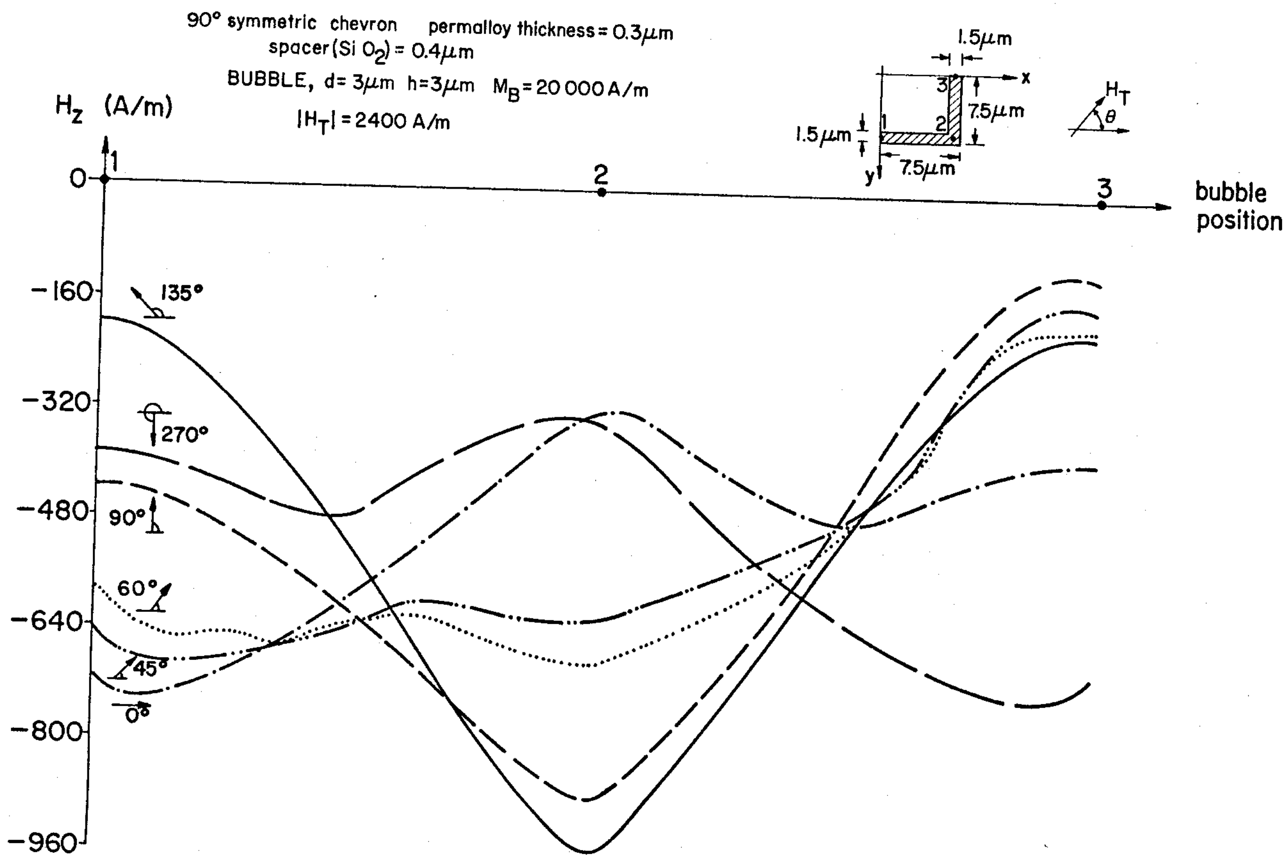

Figure 4.5 The potential well profile along the bubble path in a 90° symmetric chevron for six in-plane orientations. The bubble hardly moves from point 1 (see the inset) to point 2 until θ > 60°.

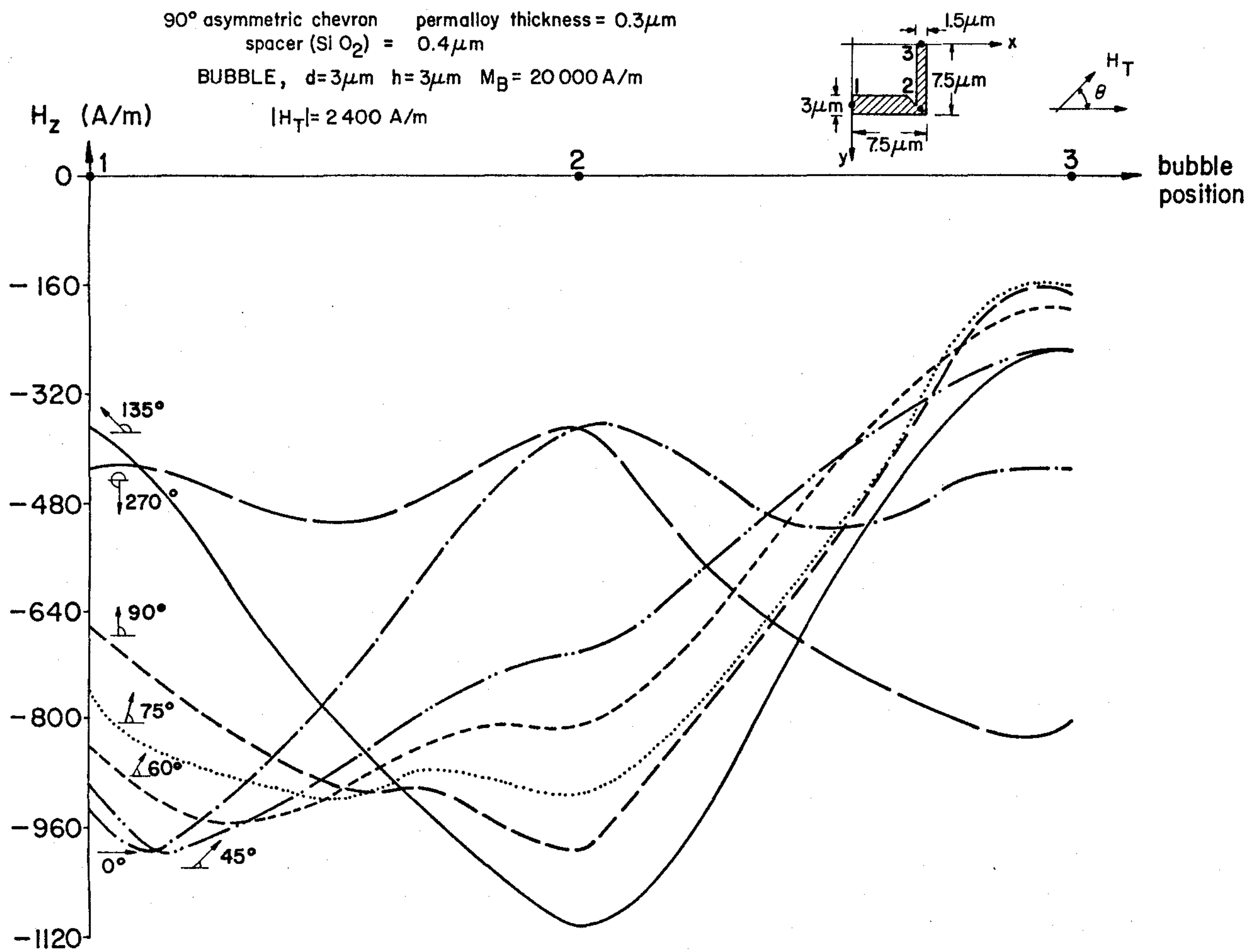

Figure 4.6 The potential well profile along the bubble path in a 90° asymmetric chevron for seven in-plane field orientations. The potential well gradients for $0 < \theta < 90°$ are larger than those of Fig. 4.5.

4.3.3 Half-Disk Circuits

The half-disk propagation structures (see Fig. 2.4(c)) represent the state-of-the-art in bubble propagation circuits. In these circuits, the gaps are situated between essentially parallel poles (poles magnetized in the same direction by the applied field). This is in contrast to the T-I circuit shown Fig. 2.4(a) where the gaps are located between orthogonal poles (poles magnetized in directions almost perpendicular to each other). As the bubble approaches the gap in a half-disk circuit, it comes under the influence of two strong poles stretching it across the gap. The bubble then shrinks away from its original position as the field rotates. Because the bubble crosses the gap by stretching rather than by translation, the potential well gradient required in the T-I circuits, is virtually eliminated. Furthermore, in the half-disk propagation circuits, there are no permalloy bar connectors between the adjacent tracks thus eliminating the possibility of a bubble moving to another track and permalloy mediated bubble-bubble interaction.

Figures 4.7 and 4.8 illustrate the two-dimensional potential well profiles for one period of symmetric and asymmetric half-disk circuits, respectively. Eight positions for the rotating in-plane are shown corresponding to one complete propagation field cycle. Assuming that the bubble will seek the position of a minimum potential, it is clear that it will move on the outer perimeter of the disks, that is along the locus of point M.

The potential well distributions for two periods of a symmetric

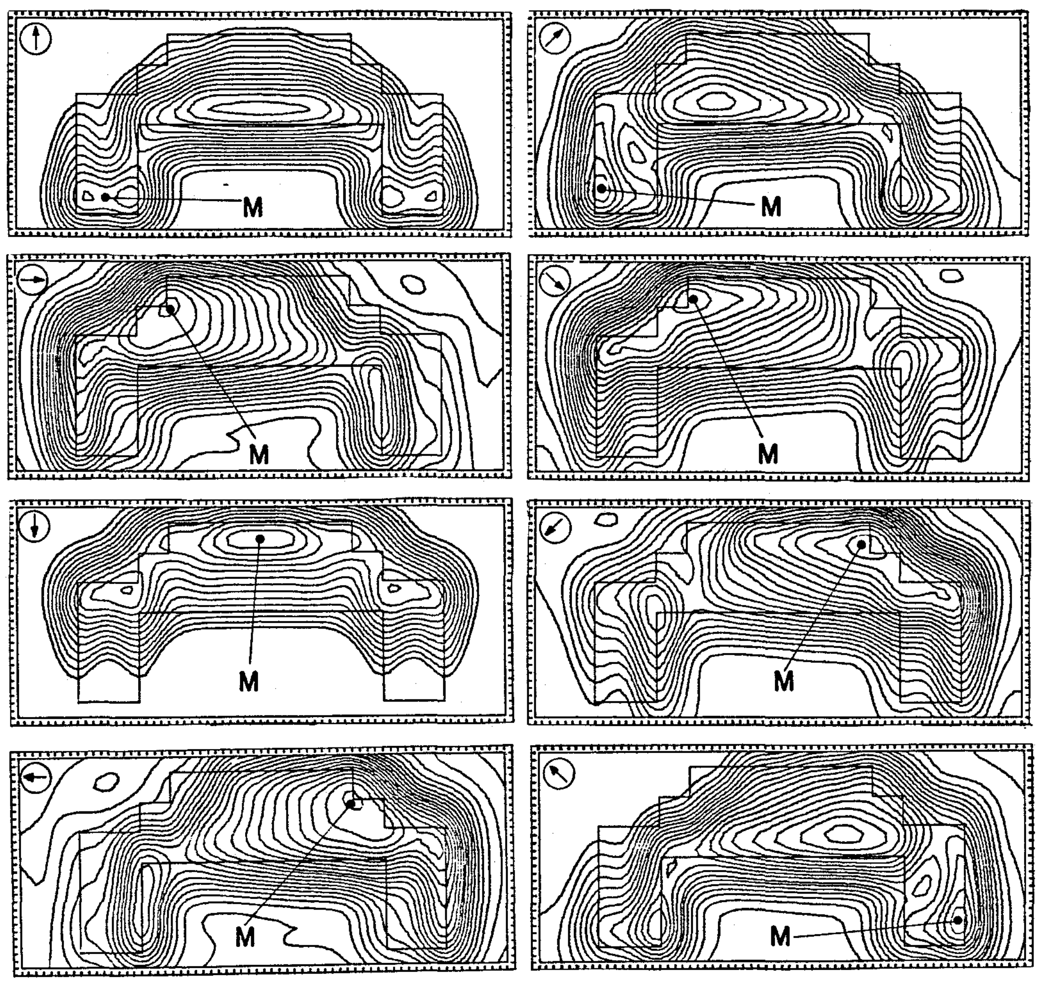

Figure 4.7 Two-dimensional potential well profile for a symmetric half-disk of 14 μm period and 2 μm gap. The points M refer to the location of the minimum potential well depth, where the center of a bubble (d = 2 μm, h = 3 μm) will be located.

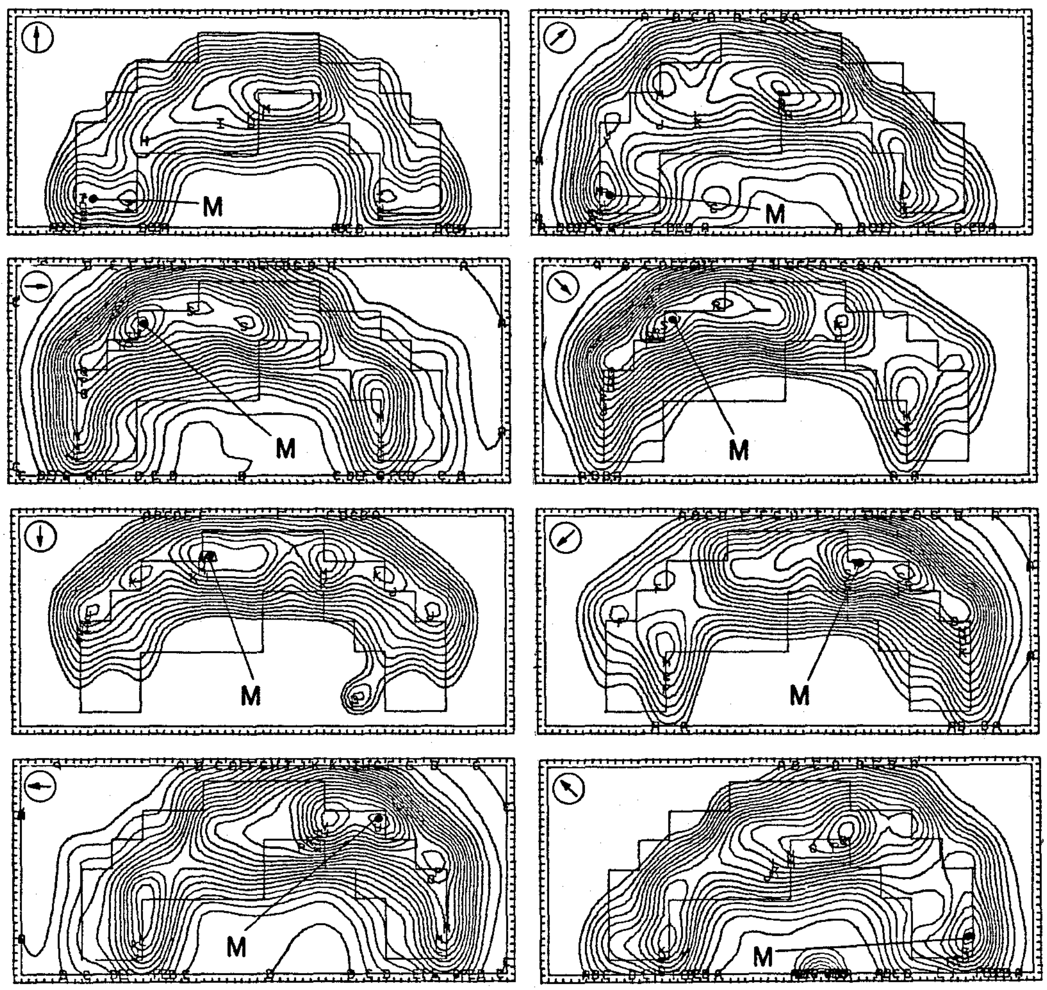

Figure 4.8 Two-dimensional potential well profile for an asymmetric half-disk circuit of 14 μm period and 2 μm gap. The points M refer to the minimum potential well depth, where the center of a bubble (d = 2 μm, h = 3 μm) will be located.

half-disk circuit are shown in Fig. 4.9 for four different in-plane field orientations. When $\underset{\sim}{H}_T$ is in the negative y-direction (see inset), two well defined poles are located on the sides of the gap (point D). The bubble will elongate and bulge across the gap. The large potential gradient for the case when $\underset{\sim}{H}_T$ in the positive x-direction assurs that the bubble will move away from the gap to point C as the field rotates. The same is true for point E when $\underset{\sim}{H}_T$ is in the negative x-direction.

Better operation, especially across the gap, is obtained by using the asymmetric half-disk structure. Figure 4.10 shows that when $\underset{\sim}{H}_T$ is in the negative y-direction, the potential well distribution in the gap is smoother and deeper as compared to Fig. 4.9. One of the most important characteristics of the asymmetric half-disk propagation circuits seen from the present analysis, and experimentally validated (Bonyhard and Smith 1976), is the fact that propagation from right to left is superior to propagation from left to right (see inset of Fig. 4.10). This is clear by comparing the gradients of the potential wells for $\underset{\sim}{H}_T$ in the negative and the positive x-directions. The former is larger than the latter suggesting smoother propagation from point D to point E.

Investigation of the potential well distributions when $\underset{\sim}{H}_T$ is in the positive y-direction for both symmetric and asymmetric half-disk circuits in Figs. 4.9 and 4.10 reveals a drawback of these circuits. The potential well is flat and the bubble will strip-out. More defined magnetic poles are required near points B and F which can be achieved by having a sharp, rather than a flat, permalloy pattern near these points

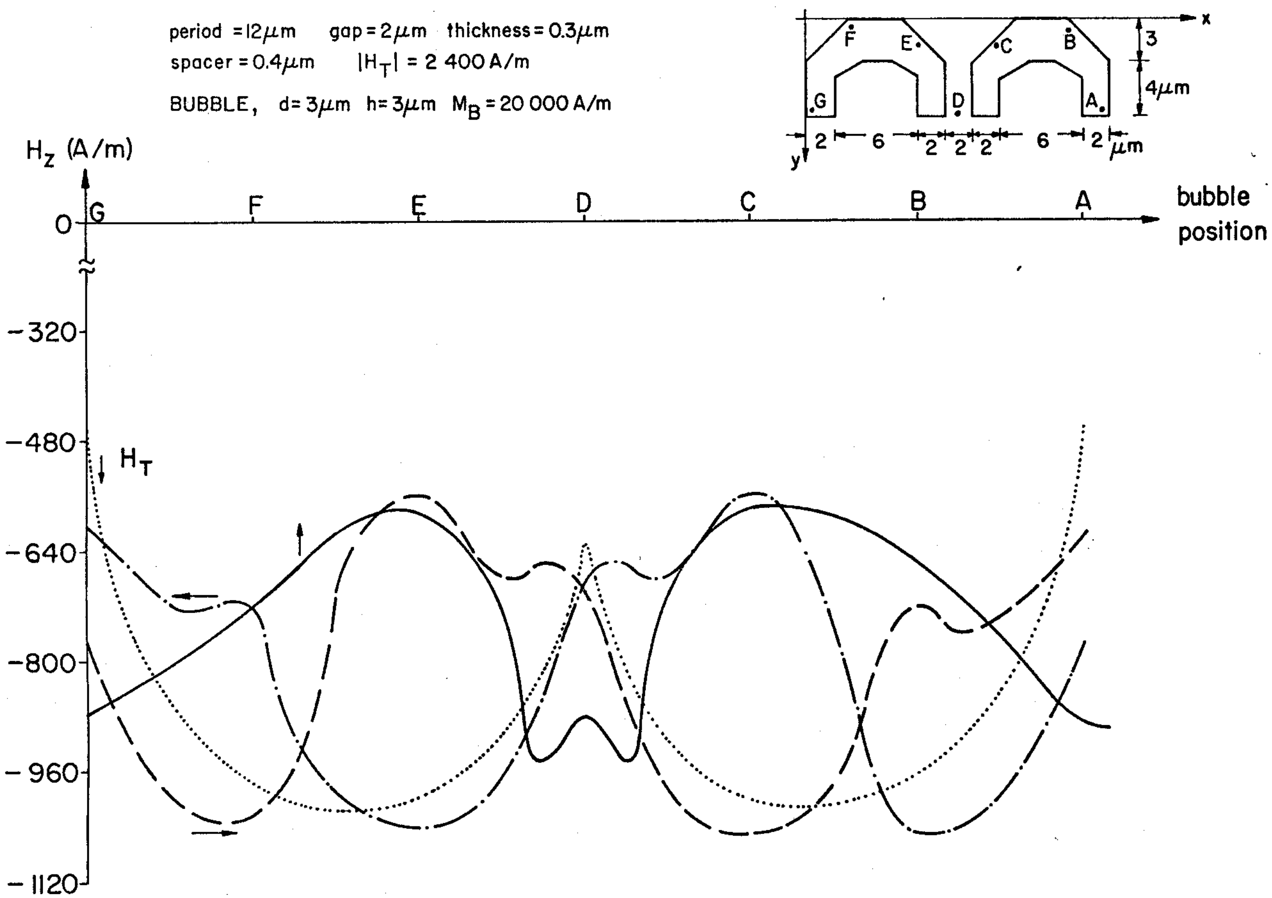

Figure 4.9 The potential well profile along the bubble path in a two period symmetric half-disk circuit (see the inset) for four in-plane field orientations. The bubble stretches across the gap when H_T is in the negative y-direction.

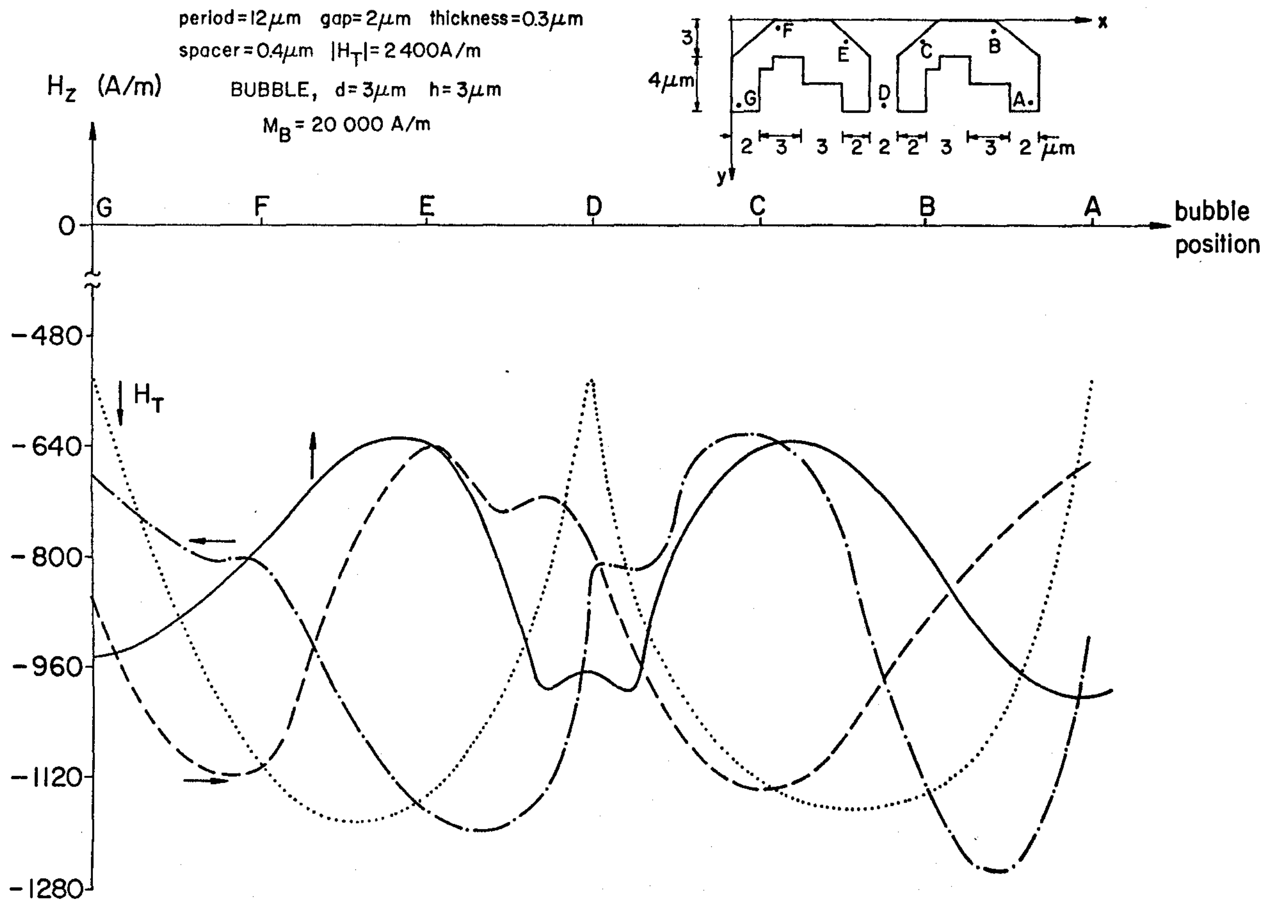

Figure 4.10 The potential well profile along the bubble path in a two period asymmetric half-disk circuit (see the inset) for four in-plane field orientations. The well depth across the gap is smoother than that in Fig. 4.9.

as in the case of the asymmetric chevron gap tolerant circuits.

4.3.4 Bubble Replicators

Figure 4.11 shows how a bubble in a gap tolerant circuit is replicated into two bubbles. One bubble goes back to the propagation track to substitute for the original bubble and the other goes to the major loop for detection (or annihilation). The permalloy element that does the replication and the transfer is called the "sideways" replicator (Bonyhard, Chen and Smith 1977).

A typical "sideways" replicator was analyzed using the analysis of Chapter 3 and the results are shown in Fig. 4.12. When $\underset{\sim}{H}_T$ is in the positive x-direction, the flat potential well produced at point 1, 2, 3 and 4 stretches the bubble. A magnetic field normal to the permalloy plane, produced by the hairpin conductor, splits the stretched bubble into two bubbles. As $\underset{\sim}{H}_T$ rotates to the negative y-direction, one bubble should go to point 7 and the other bubble to the major loop on top of point 1 (not shown in inset of Fig. 4.12). However, the strong poles produced at points 5 and 6 might attract the first bubble and an improper transfer could occur. This problem, clearly shown in Fig. 4.12, was observed experimentally (Bonyhard, Chen and Smith 1977) and a modified gate was designed (Bonyhard 1977).

4.4 Bubble Size Fluctuations

The potential well depth given by (4.1), produced by the permalloy, assumes a fixed bubble diameter, d. Actually since $\underset{\sim}{H}_z$

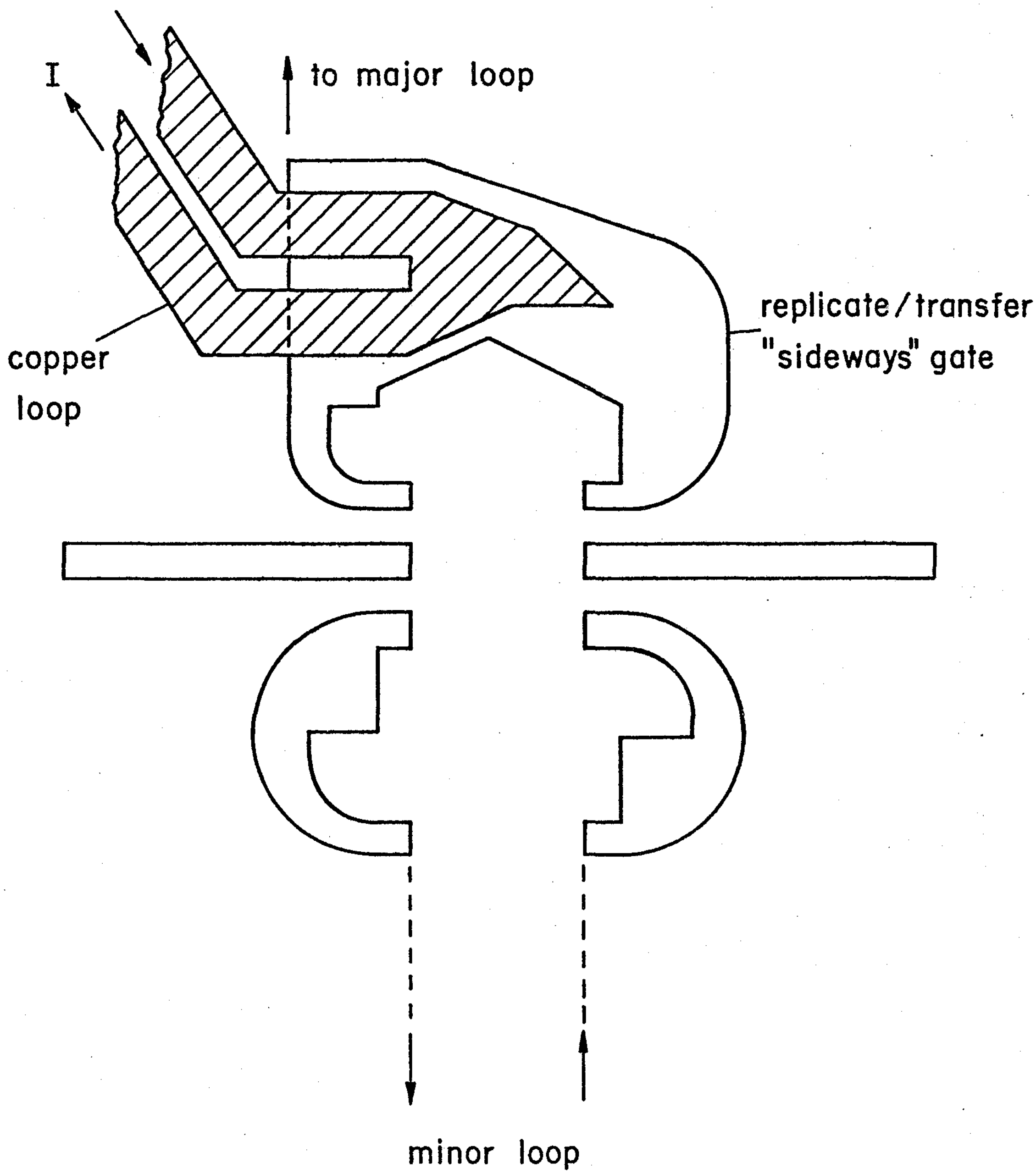

Figure 4.11 "Sideways" replicator (Bonyhard, Chen and Smith 1976). The bubble stretches under the copper loop and is split into two bubbles when I is applied. One bubble goes back to the minor loop and the other to the major loop.

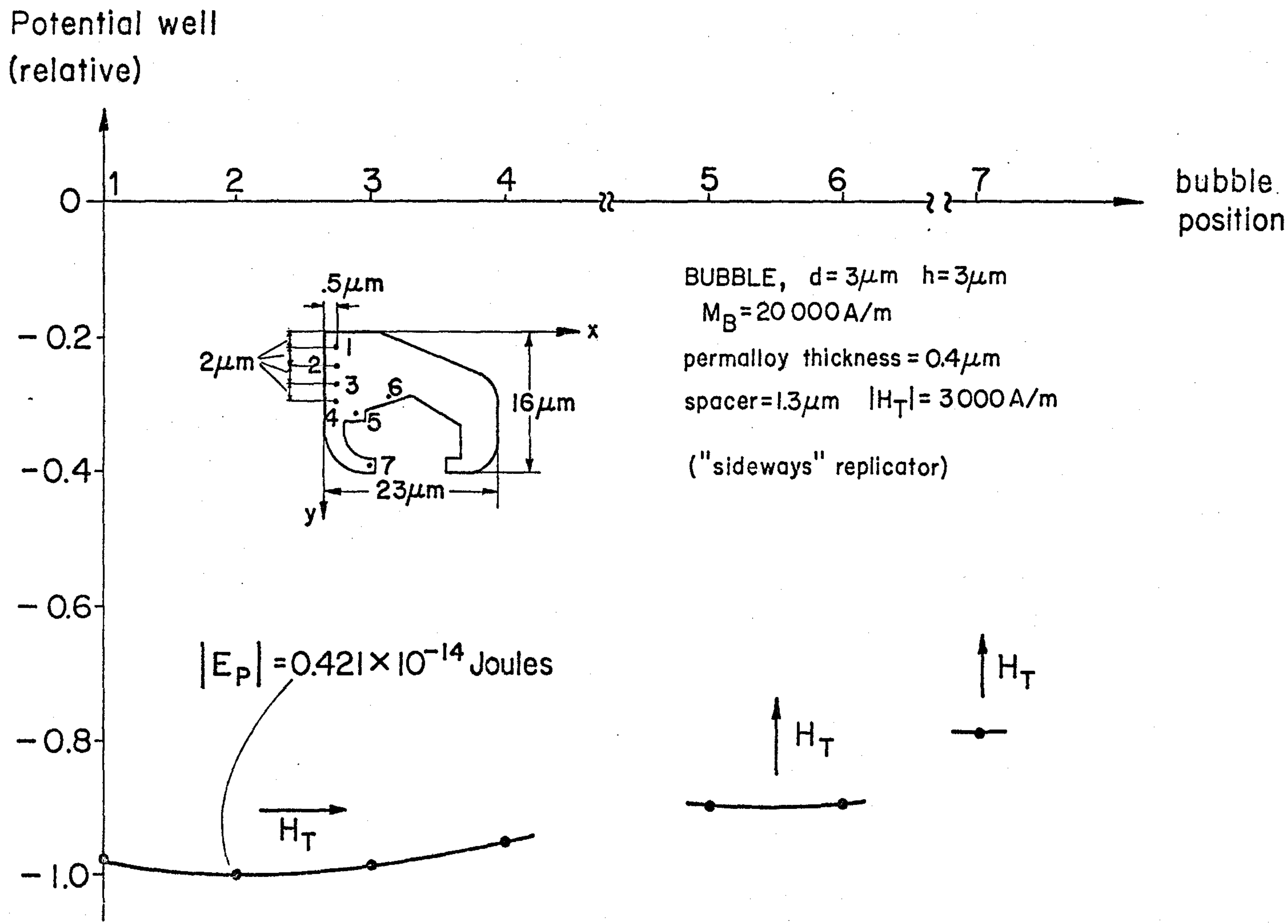

Figure 4.12 The potential well distribution in a "sidways" replicator for two in-plane field orientations.

modifies $\underset{\sim}{H}_B$, the bubble diameter changes and further analysis is required to compute the total effective change ΔH_B in H_B and hence the trapped bubble diameter d_{trap}. George and Hughes (1976b) used an equilibrium analysis based on Thiele's (1969) results to evaluate ΔH_B. They assumed that at fixed bubble diameter,the change E_p in the permalloy energy, in the presence of a bubble, is equal to the change ΔE_{MS} in the magnetostatic energy of the bubble, in the presence of the permalloy. That is

$$E_p = \Delta E_{MS} \quad . \tag{4.3}$$

The total energy E_T of a cylindrical bubble domain is given by (Thiele 1969)

$$E_T = \sigma_w(\pi dh) + 2(\mu_o M_B)(\frac{\pi}{4} d^2 h)H_B - E_{MS}, \tag{4.4}$$

where

$$\sigma_w = 4\sqrt{A_{ex} \; K_u} \tag{4.5}$$

is the wall energy density and E_{MS} is the domain's magnetostatic energy. The equilibrium relationship between H_B and d is in general found by setting $\partial E_T/\partial d$ to zero which gives

$$\frac{H_B}{M_B} = \frac{1}{\mu_o \; M_B^2 \; \pi dh} \frac{\partial E_{MS}}{\partial d} - \frac{\ell_m}{d} \quad . \tag{4.6}$$

If E_{MS} is changed by an amount ΔE_{MS}, then

$$\frac{\Delta H_B}{M_B} = \frac{1}{\mu_o \; M_B^2 \; \pi dH} \frac{\partial (\Delta E_{MS})}{\partial d} \tag{4.7}$$

and combining (4.1)-(4.3) and (4.7), the total effective change in H_B is, then, given by

$$\Delta H_B = H_z + \frac{d}{2}\frac{\partial H_z}{\partial d} \quad . \tag{4.8}$$

The bubble will, thus, be affected by an effective bias field

$$H_B\ (\text{eff.}) = H_B + \Delta H_B \quad . \tag{4.9}$$

George and Hughes (1976b) computed the quantity $\partial H_z/\partial d$ by plotting various graphs for H_z versus d and measuring the slope of these graphs. In addition to the neccessity of evaluating H_z for several bubble diameters in order to measure the slope, the error using this approach can be as high as 10% (George and Archer 1973b).

A simpler and more accurate approach based on understanding the physical essence of the problem was implemented and tested by Ishak and Della Torre (1978a). When a bubble approaches a magnetized permalloy element, it changes the permalloy energy by an amount E_p and the bubble, momentarily, feels a change H_z in the bias field. The bubble diameter changes to a new value to stabilize with the new bias field value. This new bubble will, again, change the permalloy energy by an amount ΔE_p and H_z is modified by an amount ΔH_z (corresponding to ΔE_p). The bubble diameter changes again. The process is repeated until an equilibrium is achieved and a stable bubble-permalloy configuration is attained. This iterative interaction between the bubble and the permalloy suggests an iterative numerical procedure, to compute the stable bubble characteristics and the final permalloy magnetization distribution and energy.

4.5 The Bubble Size Fluctuation Algorithm

4.5.1 Introduction

Given a bubble material of thickness h and characteristic length ℓ_m which supports bubble domains of diameter d at a bias field H_B, the bubble size fluctuation algorithm computes the new diameter d_{trap} of the bubble when it is trapped under the permalloy as well as its new center position (the backward modeling problem). The algorithm also checks the collapse and the run-out conditions. Thiele's analysis (1969) or DeBonte's analysis (1975) can be used to study the stability of high Q bubbles and low Q bubbles, respectively. Computer programs based on the analysis of DeBonte (1975) are implemented (Ishak and Della Torre 1977a and Ishak and Della Torre 1977b) to compute the parameters of bubble domains in low Q materials.

The bubble size fluctuation algorithm consists of the following steps:

Step 1 Set $k = 1$. Set $d^{(k-1)} = d$. Choose a tolerance ε_1 for the termination criterion. Recommended value, $\varepsilon_1 = 10^{-8}$.

Step 2 Call the collapse and run-out algorithm, of Subsection 4.5.2, to compute the collapse and run-out fields H_{CO} and H_{RO}, respectively.

Step 3 Call the magnetization algorithm of Subsection 3.5.2 to compute $\underset{\sim}{M}^{(k)}(\underset{\sim}{r})$ and hence $E_p^{(k)}$ using (3.45).

Step 4 Compute $\underset{\sim}{H}_z^{(k)}$ using (4.1).

Step 5 Compute the modified bias field

$$\underset{\sim}{H}_B^{(k)}(\text{mod.}) = \underset{\sim}{H}_B + \underset{\sim}{H}_z^{(k)} \tag{4.10}$$

Step 6 Exit if $H_B^{(k)}(\text{mod.}) > H_{CO}$ or $H_B^{(k)}(\text{mod.}) < H_{RO}$.

Step 7 Call the bubble diameter algorithm, of Subsection 4.5.3, to compute the modified bubble diameter $d^{(k)}$.

Step 8 Compute the residual error

$$e_1^{(k)} = |d^{(k)} - d^{(k-1)}| \tag{4.11}$$

Step 9 Stop if $e_1^{(k)} < \varepsilon_1$. Set $d_{trap} = d^{(k)}$.

Step 10 Set k = k+1. Go to Step 3.

4.5.2 Computation of the Collapse and Run-out Fields

Thiele (1969) derived the equilibrium and stability conditions for a bubble domain as

$$\lambda - a\frac{H_B}{M_B} - F(a) = 0 \quad , \tag{4.12}$$

$$\lambda - S_o(a) < 0 \quad , \tag{4.13}$$

and

$$\lambda - S_n(a) > 0 \ , \ n \geq 2, \tag{4.14}$$

where

$$a = \frac{d}{h} \tag{4.15}$$

is the aspect ratio of the bubble,

$$\lambda = \frac{\ell_m}{h} \tag{4.16}$$

is the normalized characteristic length, F(a) is the force function, $S_o(a)$ is the radial stability function and $S_n(a)$, $n \geq 2$ are the higher order stability functions. Since

$$S_n(a) > S_{n+1}(a), \; n \geq 2 \tag{4.17}$$

for any a, (4.14) can be reduced to

$$\lambda - S_2(a) > 0 \quad . \tag{4.18}$$

Hegedüs and Della Torre (1977) obtained simple expressions for F(a), $S_o(a)$ and $S_2(a)$, among other functions, in terms of the complete elliptical integral CEL, defined in (3.22). They showed that

$$F(a) = \frac{2a}{\pi} \; [\text{CEL}\;(k,\; 1,\; 1/k,\; k) - a] \quad , \tag{4.19}$$

$$S_o(a) = \frac{2a^2}{\pi} \; [1 - ak \quad \text{CEL}\;(k,\; 1,\; 1,\; 0)] \quad , \tag{4.20}$$

$$S_2(a) = \frac{2a}{9\pi} \; [a - k \quad \text{CEL}\;(k,\; 1,\; a^2+4,\; -4)] \quad , \tag{4.21}$$

where

$$k^2 = \frac{1}{a^2+1} \tag{4.22}$$

If a bubble of diameter d and characteristic length ℓ_m is stable at a bias field H_B, then the collapse and run-out fields can be computed using the following algorithm:

The Collapse and Run-out Algorithm

Step 1 Compute a using (4.15). Compute λ using (4.16).

Step 2 Call the inverse bubble function algorithm, of Subsection 4.5.2, to compute the collapse and run-out aspect ratios a_c and a_c, respectively such that $S_o(a_c) = \lambda$ and $S_2(a_r) = \lambda$.

Step 3 Compute $F(a_c)$ and $F(a_r)$ using (4.19).

Step 4 Compute H_{CO} and H_{RO} using (4.12) and replacing a by a_c and a_r, respectively.

The following algorithm computes the aspect ratio a_f given any of the three function $F(a_f)$, $S_o(a_f)$ or $S_2(a_f)$. The steps of the algorithm are illustrated in Fig. 4.13. For simplicity only the case for $S_o(a)$ is shown, that is given $S_o(a_f)$ this algorithm computes a_f.

The Inverse Bubble Function Algorithm

Step 1 Set $k = 1$. Choose a tolerance ε_2 for the termination criterion.

Step 2 Let $a^{(k-1)} = 10\, S_o(a_f)$.

Step 3 Compute $S_o(a^{(k-1)})$ using (4.20). This corresponds to point A in Fig. 4.13.

Step 4 Compute $a^{(k)}$ using

$$a^{(k)} = a^{(k-1)} \frac{S_o(a_f)}{S_o(a^{(k-1)})} \, . \tag{4.23}$$

Step 5 Set $a^{(k)} = 0.01$, if $a^{(k)} < \varepsilon_2$.

Step 6 Compute $S_o(a^{(k)})$ using (4.20). This corresponds to point B in

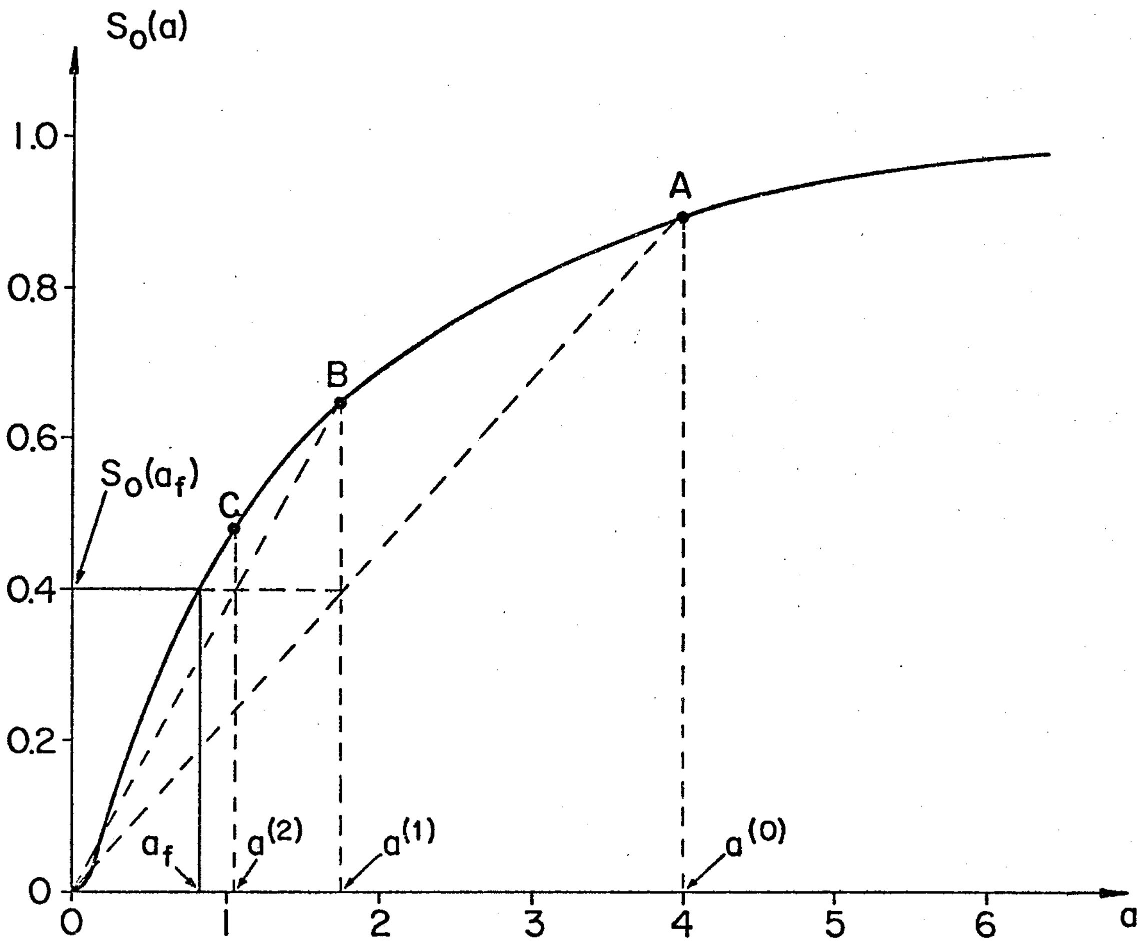

Figure 4.13 The radial stability function $S_o(a)$ as a function of the bubble's aspect ratio (Thiele 1969). The points A, B and C illustrate the steps of the inverse bubble function algorithm of Subsection 4.5.2.

Fig. 4.13.

Step 7 Compute the residual error

$$e_2^{(k)} = |S_o(a^{(k)}) - S_o(a_f)| \quad . \tag{4.24}$$

Step 8 Stop if $e_2^{(k)} < \varepsilon_2$. Set $a_f = a^{(k)}$.

Step 9 Set k = k+1. Go to Step 4.

Comment: To accelerate the convergence of the computations, an over-relaxed value for $a^{(k)}$ can be used to replace the value obtained in Step 4 as

$$a^{(k)} \leftarrow \gamma\, a^{(k)} + (1-\gamma)\, a^{(k-1)} \quad , \tag{4.25}$$

where $\gamma > 1$. Recommended values:

$\gamma = 1.4$ when $F(a_f)$ is given,

$\gamma = 1.2$ when $S_o(a_f)$ or $S_2(a_f)$ are given.

4.5.3 Computation of the New Bubble Diameter

If we define G(a) as

$$G(a) = a\, H_n + F(a) - \lambda \quad , \tag{4.26}$$

where

$$H_n = \frac{H_B}{M_B} \tag{4.27}$$

then $G(a) = 0$ is a solution of (4.12) and this suggests that a can be obtained using the Newton-Raphson iterative algorithm in the form

$$a^{(n)} = a^{(n-1)} - \frac{G(a^{(n-1)})}{G'(a^{(n-1)})} \ , \tag{4.28}$$

where n is the iteration number and

$$G'(a^{(n-1)}) \triangleq \left.\frac{\partial G(a)}{\partial a}\right|_{a=a^{(n-1)}} . \tag{4.29}$$

Thiele (1969) showed that

$$\frac{\partial F(a)}{\partial a} = \frac{1}{a}\,[F(a) - S_o(a)] \tag{4.30}$$

and hence

$$r_g \triangleq \frac{G(a)}{G'(a)} = \frac{a\,H_n + F(a) - \lambda}{H_n + (1/a)[F(a) - S_o(a)]} . \tag{4.31}$$

Viewed from this point, the modified bubble diameter d(mod.) at a bias field H_B(mod.) can be computed from an initial value d using the following algorithm:

The Bubble Diameter Algorithm

Step 1 Set k = 1. Choose a tolerance ε_3 for the termination criterion.

Step 2 Compute $a^{(k)}$ using (4.15). Compute λ using (4.16). Compute H_n(mod.) using

$$H_n(\text{mod.}) = \frac{H_B(\text{mod.})}{M_B} \tag{4.32}$$

Step 3 Compute $r_g^{(k)}$ using (4.31).

Step 4 Compute $a^{(k+1)}$ using (4.28).

Step 5 Compute $d^{(k+1)}$ as

$$d^{(k+1)} = h\,a^{(k+1)} \tag{4.33}$$

Step 6 Compute the residual error

$$e_3^{(k)} = |F(a^{(k+1)}) - a^{(k+1)} \quad H_n(\text{mod.}) - \lambda| \ . \tag{4.34}$$

Step 7 Stop if $e_3^{(k)} < \varepsilon_3$. Set d(mod.) = $d^{(k+1)}$.

Step 8 Set k = k+1. Go to Step 3.

4.6 Examples

Figure 4.14 shows a T-I bubble propagation circuit used by Kryder, Ahn, and Powers (1975) to propagate 2 μm diameter bubbles in a 1.5×10^{10} bits/m^2 memory chip. The bubble size fluctuation algorithm is used to compute the changes in the bubble diameter as it moves from the I bar to the T bar across the gap. Table 4.1 gives the actual bubble diameter at 3 points along the propagation track (points, A, B and the middle of the gap). The effective change in the bias field and bubble diameter is shown in Table 4.1 for two in-plane field values.

To check the bubble size fluctuation algorithm, the diameter versus the bias field curves for a bubble trapped at the end of a rectangular permalloy bar are plotted and compared to the experimental results of Jones and Enoch (1974). See Fig. 4.15. The observed agreement is excellent and the maximum error in the computed bubble diameter is about 4%. It is noted that about 3 iterations are required to achieve an accuracy of better than 0.5% in the bubble diameter using the algorithm of Subsection 4.5.1. In fact, during the execution of Step 3 of this algorithm, a search is performed over a few points in the neighborhood of the bubble center, at each iteration, to find the minimum of the potential well at which the new bubble center will be

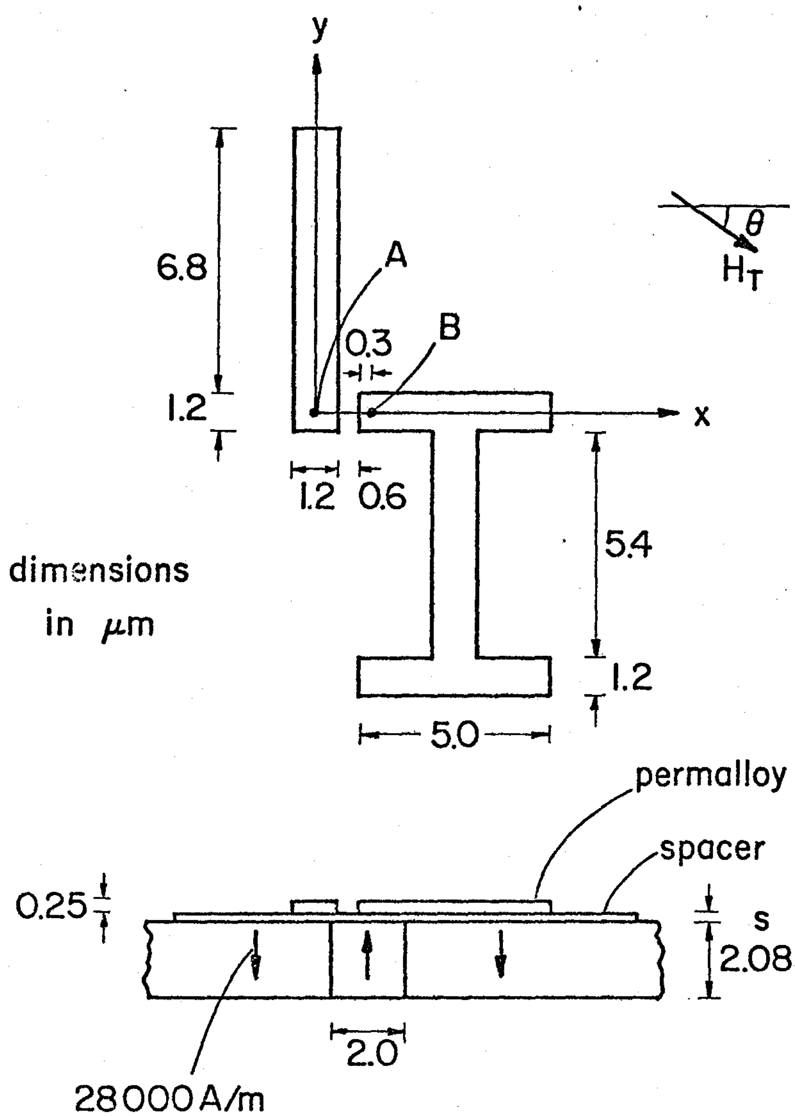

Figure 4.14 The T-I propagation circuit used by Kryder, Ahn and Powers (1975) to propagate 2 μm diameter bubbles in amorphous films.

TABLE 4.1

RESULTS OF THE BUBBLE SIZE FLUCTUATION ALGORITHM FOR

THE T-I PROPAGATION CIRCUIT OF FIG. 4.14

BUBBLE CENTER POSITION	ITERATION NO. (IT)	H_T = 2400 A/M		H_T = 3200 A/M	
		H_z (A/m)	BUBBLE DIAMETER (μm)	H_z (A/m)	BUBBLE DIAMETER (μm)
A	1	-1368.23	2.818	-2064.79	3.275
	2	-1088.10	2.645	-1452.08	2.930
	3	-1071.65	2.635	-1412.00	2.910
MIDDLE OF GAP	1	-959.01	2.567	-1331.03	2.795
	2	-868.04	2.513	-1063.24	2.630
	3	-874.58	2.517	-1101.39	2.653
B	1	-974.75	2.577	-1370.44	2.819
	2	-850.90	2.502	-1098.39	2.651
	3	-863.15	2.510	-1087.32	2.645

Original bubble diameter, d = 2μm

Original bias field, H_B = 12722 A/m

Collapse field, H_{CO} = 13620 A/m

Run-out field, H_{RO} = 10396 A/m

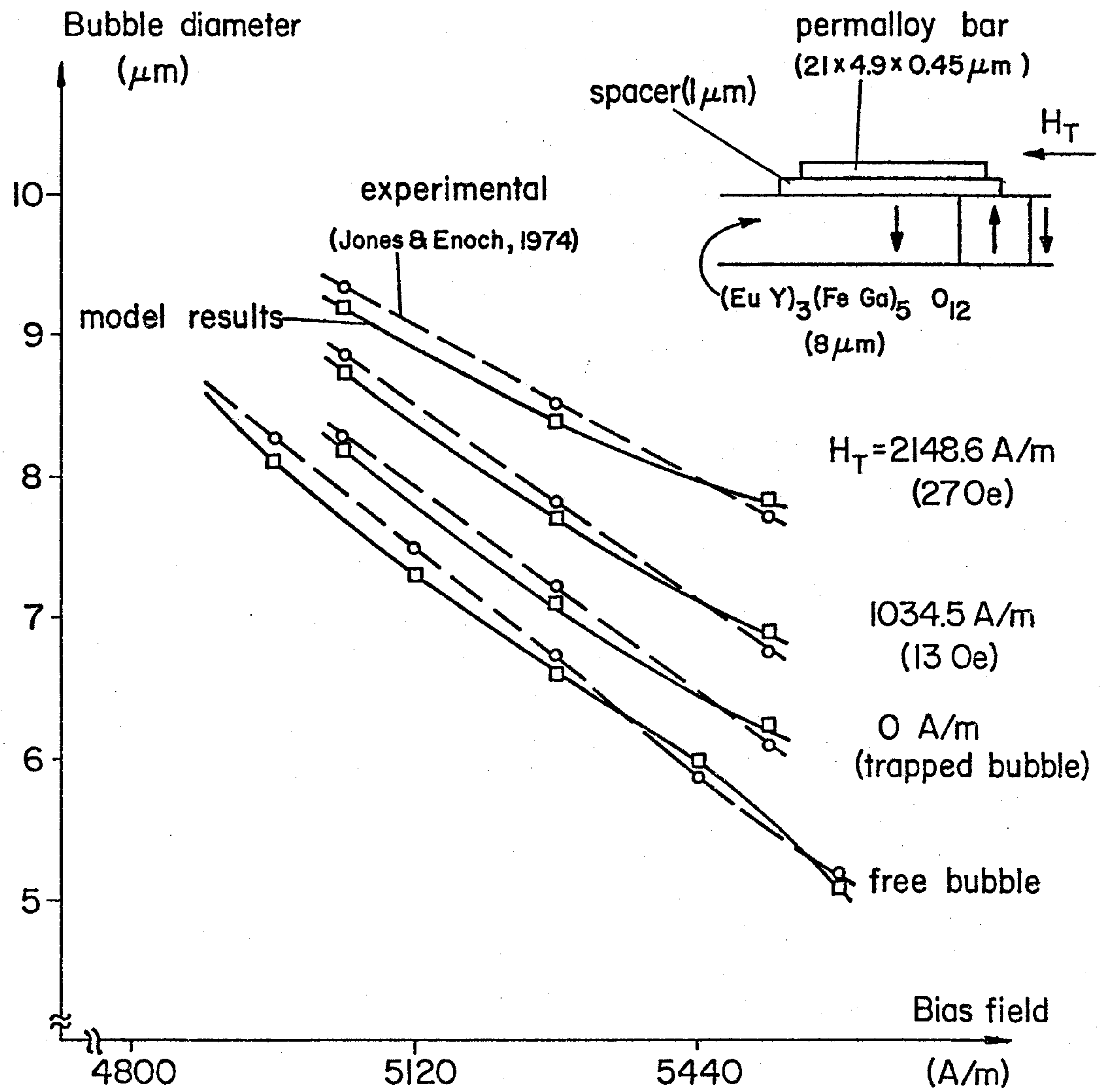

Figure 4.15 Comparison between the results of the bubble size fluctuation algorithm and the experimental data of Jones and Enoch (1974).

located. This means that not only the new bubble diameter is computed using this algorithm but also the new bubble center.

4.7 Conclusions

The analysis presented for bubble propagation circuits, based on the continuum model of Chapter 3, provides an accurate and efficient means of characterizing arbitary shaped permalloy circuits. The analysis showed that gap tolerant circuits (half-disks and asymmetric chevrons) have the advantages of providing a smooth potential well across the gap and large potential well gradients, in general. These result in low in-plane field requirement for propagation.

The results for the chevron circuits shows that the method can be used to modify a specific design to improve the performance. For example, the asymmetric chevron structure is superior to the symmetric one because of the larger potential well gradients and, hence, the more uniform bubble propagation.

The bubble size fluctuation algorithm provides an excellent means of avoiding improper propagation and loss of information, corresponding to stripping or collapsing of bubbles, respectively. In addition, being able to determine the bubble center location under the permalloy circuit is useful in studying bubble replicators because the position of the hairpin conductor loop which provides the cutting field and the phase of the current pulse is determined by the location of the bubble under the permalloy. Moreover, the bubble size fluctuation algorithm can be used in studying the dynamics aspects of bubble circuits.

CHAPTER 5

BUBBLE CIRCUIT OPTIMIZATION

5.1 Introduction

The continuum model of Chapter 3 and the analysis of bubble circuits, presented in Chapter 4, are used as the analysis part of an algorithm for propagation circuit optimization. The criterion for optimization is based on minimizing bubble size fluctuations, assuring proper propagation at all critical points in the circuits and satisfying certain constraints set by practical considerations. As a result, a set of optimum parameters for the bubble-permalloy circuit is computed which when used will result in achieving a potential well profile that yields optimum performance and meets the required specifications.

To reduce the computer time required for the optimization procedure, quadratic polynomial approximations are used to model the potential well depths as functions of the circuit parameters. This method was checked separately and proved satisfactory and efficient.

The constraints on the shape of the potential well distribution and specifically, on the gradient of the well, for a specific circuit, are based on experimental observations of the difficulties associated with propagation along this type of circuit. An example is the gap between the I and the T elements in a T-I circuit where a large gradient is required to move the bubble from the I, across the gap, to the T.

5.2 Qualitative Analysis

In one class of field access propagation circuits the propagation track is almost linear and the bubble velocity does not change appreciably along the propagation track. Examples of circuits belonging to this class are T-I, parallel-bars and half-disks. On the other hand, in the class of circuits including symmetric and asymmetric chevrons, the bubble velocity varies over a wide range as discussed in Chapter 4. Optimum propagation is achieved if the bubble is translated in a potential well whose depth and shape remains constant as it moves by circuits belonging to the first class and in a potential well whose depth is proportional to the bubble velocity for circuits in the second class.

The velocity of a bubble domain (Thiele 1969) is given by

$$v = \frac{\mu_w}{2} (\Delta H_z - \frac{8}{\pi} H_c) \, , \tag{5.1}$$

where ΔH_z is the z-field differential across the bubble, that is

$$\Delta H_z = \frac{\partial H_z}{\partial X} \cdot d \, , \tag{5.2}$$

H_c is the domain wall coercivity and H_z is the effective potential well depth as computed in the bubble size fluctuation algorithm of Subsection 4.5.1. As ΔH_z increases, v increases until the saturation velocity which varies from one material to another from about 20 m/s to about 60 m/s.

Equations (5.1) and (5.2) suggest that to overcome bubble coercivity and mobility drag, the gradient of the potential well should satisfy

$$\frac{\partial H_z}{\partial X} d \geq \frac{8}{\pi} H_c + \frac{2v}{\mu_w} \tag{5.3}$$

everywhere along the propagation track. Experimental observations, though, show that it is enough to satisfy (5.3) at the critical points in the circuit to assure propagation elsewhere (Almasi and Lin 1976). Knowledge of these points, therefore, is essential for circuit design.

5.3 Circuit Parameters

Figure 5.1 shows a typical T-I bubble propagating circuit. The effective potential well depth H_z and, hence, the well gradient $\partial H_z/\partial X$ at any point in the circuit are functions of the circuit parameters. These include permalloy, bubble and external parameters such as the in-plane field and temperature fluctuations. In the following analysis, only those parameters shown in Fig. 5.1 will be considered, that is

$$H_{zi} \triangleq H_{zi}\ (\ell_1,\ \ell_2,\ w,\ t,\ g,\ d,\ h,\ M_B,\ s,\ H_T)\ , \tag{5.4}$$

where i refers to any point along X.

Although any of the parameters in (5.4) may vary independently, yet practical device fabrication requirements and memory specifications impose certain bounds on the values of these parameters. Table 5.1 illustrates the factors affecting the upper and lower bounds on each of the parameters in (5.4).

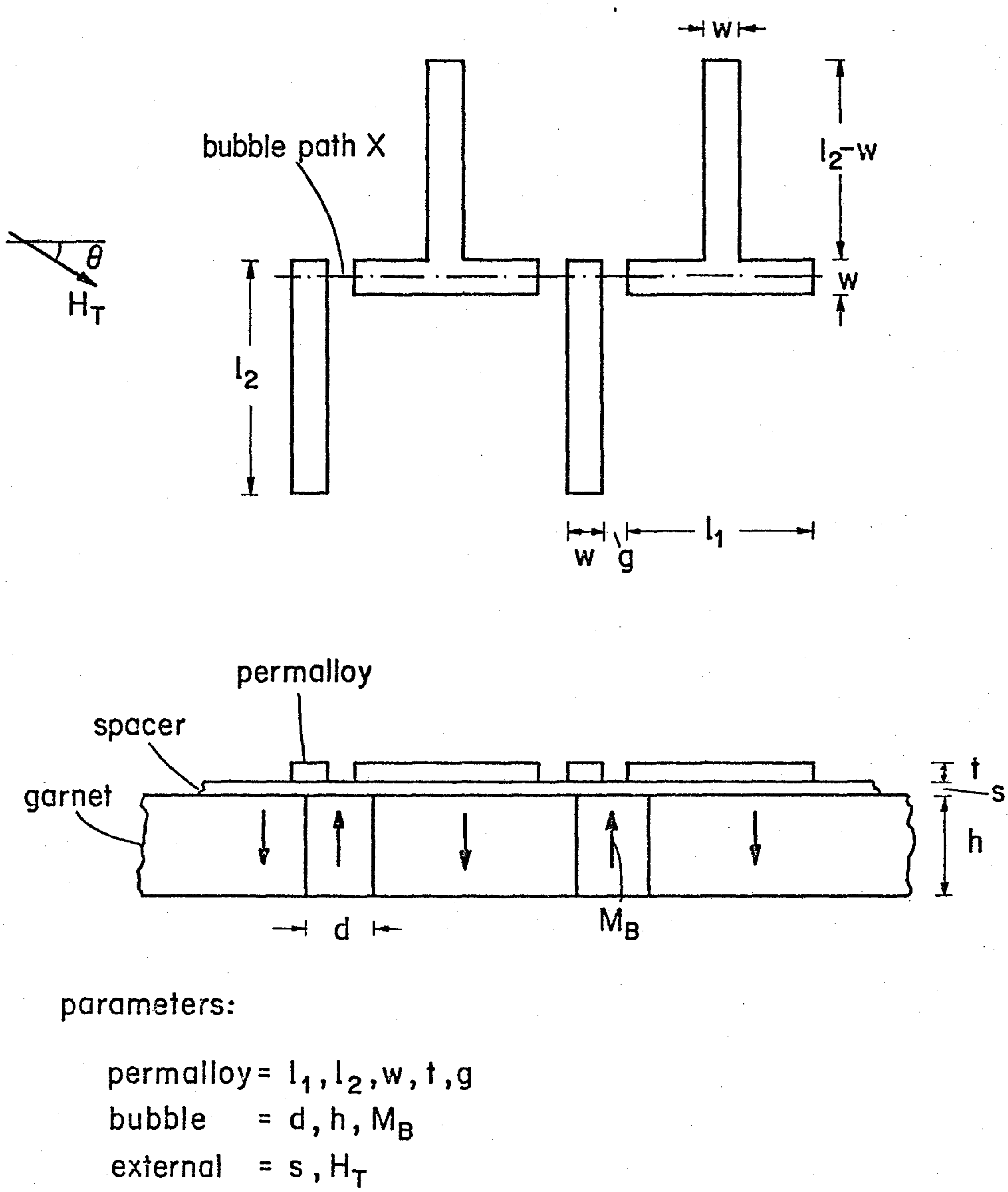

Figure 5.1 A typical T-I propagation circuit. X refers to the bubble path. Permalloy, bubble and external parameters are shown.

5.3 The Optimization Problem

Following the discussion of Sections 5.1-5.3, the problem of propagation circuit optimization can be stated as

$$\text{minimize} \qquad U_1(\underset{\sim}{\phi}) = \max_{i \varepsilon N_1} \left| H_{zi}(\underset{\sim}{\phi}) - H_{zR}(\underset{\sim}{\phi}) \right| \tag{5.5}$$

$$\text{subject to} \qquad c_j(\underset{\sim}{\phi}) = \frac{\partial H_{zj}}{\partial X} - \frac{1}{d}\left[\frac{8}{\pi} H_c + \frac{2v}{\mu_w}\right] \geq 0 \ , \quad j \ \varepsilon \ N_2, \tag{5.6}$$

$$c_k(\underset{\sim}{\phi}) \geq 0 \qquad , \quad k \ \varepsilon \ N_3, \tag{5.7}$$

$$\text{where} \qquad \underset{\sim}{\phi} \stackrel{\Delta}{=} [\ell_1 \quad \ell_2 \quad w \quad t \quad g \quad d \quad h \quad M_B \quad s \quad H_T]^T \ , \tag{5.8}$$

$$N_1 \stackrel{\Delta}{=} \{1,\ 2,\ \ldots,\ n_1\} \ , \tag{5.9}$$

$$N_2 \stackrel{\Delta}{=} \{1,\ 2,\ \ldots,\ n_2\} \ , \tag{5.10}$$

$$N_3 \stackrel{\Delta}{=} \{n_2+1,\ n_2+2,\ \ldots,\ n_3\} \ , \tag{5.11}$$

$$n_3 - n_2 \leq p \qquad , \tag{5.12}$$

n_1 is the number of points, along the propagation track, at which H_z is considered, n_2 is the number of critical points in the circuit and p is the number of circuit parameters. Equation (5.5) requires the definition of a reference potential $H_{zR}(\underset{\sim}{\phi})$. This can be taken as the potential well depth at the end of the I elements in T-I and Y-I circuits or at the end of the disks in half-disk circuits. It should be noted that the objective function (5.5) refers to circuits where the bubble moves with a uniform velocity.

The set of constraints in (5.7) determines the upper and the lower bounds on each of the parameters listed in (5.8). For example

$$c_{n_2+1}(\underset{\sim}{\phi}) = \ell_{1h} - \ell_1 , \tag{5.13}$$

$$c_{n_2+2}(\underset{\sim}{\phi}) = \ell_1 - \ell_{1\ell} , \tag{5.14}$$

where ℓ_{1h} and $\ell_{1\ell}$ are the upper and the lower bounds on ℓ_1.

5.5 Approximation and Method of Solution

Since an optimization procedure will require a repetitive calculation of the objective function, a reduction in the required computer time can be achieved by using a suitable approximation for H_z as a function of the circuit parameters. Abdel-Malek and Bandler (1978a) developed a technique to compute the coefficients of a quadratic polynomial approximation to a function which is assumed continuous and has continuous derivatives. In this work, the well depth, H_z, will be approximated by a quadratic polynomial in the components of the vector $\underset{\sim}{\phi}$, which are the circuit parameters. That is

$$\begin{aligned} P(\underset{\sim}{\phi}) = {} & b_1\phi_1^2 + b_2\phi_2^2 + \ldots + b_p\phi_p^2 + b_{p+1}\phi_1\phi_2 \\ & + b_{p+2}\phi_1\phi_3 + \ldots + b_{K-p-1}\phi_{p-1}\phi_p \\ & + b_{K-p}\phi_1 + b_{K-p+1}\phi_2 + \ldots + b_{K-1}\phi_K + b_K , \end{aligned} \tag{5.15}$$

The coefficients in (5.15) are chosen in such a way to force the polynomial to coincide with $H_z(\underset{\sim}{\phi})$ at K base points,

$$\underset{\sim}{\phi}^{\ell}, \ \ell = 1, 2, \ldots, K , \ K = \frac{(p+1)(p+2)}{2} \tag{5.16}$$

that is

$$P(\underset{\sim}{\phi}^{\ell}) = H_z(\underset{\sim}{\phi}^{\ell}) , \ \ell = 1, 2, \ldots, K , \tag{5.17}$$

and to accurately approximate $H_z(\underset{\sim}{\phi})$ at other points within the specified interpolation region (the region within which the approximation is valid). See Abdel-Malek (1977) and Abdel-Malek and Bandler (1978b).

To test the quadratic approximation method, it was used to model the potential well depths H_{zA} and H_{zB} at the two points A and B, respectively, in the T-I propagation circuit shown in Fig. 4.14. Keeping the first eight components (ϕ_1, ϕ_2, ..., ϕ_8) of the vector $\underset{\sim}{\phi}$, that is (ℓ_1, ℓ_2, w, t, g, d, k, M_B), in (5.8) fixed at the values illustrated in Fig. 4.14, the last two components, that is (s, H_T) are allowed to vary in the ranges

$$3.0 \leq \phi_9 \leq 6.0 \ , \tag{5.18}$$

$$0.4 \leq \phi_{10} \leq 3.6 \ , \tag{5.19}$$

where

$$\phi_9 \stackrel{\Delta}{=} 10^7 \ s \ , \tag{5.20}$$

$$\phi_{10} \stackrel{\Delta}{=} 10^{-3} \ H_T \ . \tag{5.21}$$

The scaling factors in (5.20) and (5.21) are used to improve the numerical conditioning of the computation. The quadratic polynomial approximations of H_{zA} and H_{zB} are, respectively,

$$P_A(\phi_9,\phi_{10}) = b_{1A}\phi_9^2 + b_{2A}\phi_{10}^2 + b_{3A}\phi_9\phi_{10} + b_{4A}\phi_9 + b_{5A}\phi_{10} + b_{6A} \ , \tag{5.22}$$

$$P_B(\phi_9,\phi_{10}) = b_{1B}\phi_9^2 + b_{2B}\phi_{10}^2 + b_{3B}\phi_9\phi_{10} + b_{4B}\phi_9 + b_{5B}\phi_{10} + b_{6B} \ . \tag{5.23}$$

where the coefficients are to be determined.

Two sets of variables (ϕ_9 and ϕ_{10}) are used to compute H_{zA}, H_{zB}, P_A and P_B. The base points, interpolation region and the results obtained are shown in Table 5.2. The maximum error is less than 5%.

TABLE 5.2

COMPARISON BETWEEN THE ACTUAL POTENTIAL WELL DEPTH
AND THE QUADRATIC POLYNOMIAL APPROXIMATION
FOR THE CIRCUIT OF FIG. 4.14

PARAMETERS		POTENTIAL WELL DEPTHS		QUADRATIC APPROXIMATION	
ϕ_9	ϕ_{10}	H_{zA}(OE)	H_{zB}(OE)	P_A	P_B
4.500	1.600	- 8.5500	-10.6500	- 8.4926	-10.6421
4.936	3.272	-17.8801	-26.1425	-16.9866	-25.8055

$\phi_9 = 10^7 s$, s in meters

$\phi_{10} = 10^{-3}\ H_T$, H_T in A/m

Interpolation region: $3.0 \leq \phi_9 \leq 6.0$
$0.4 \leq \phi_{10} \leq 3.6$

Base points $(\phi_9^\ell, \phi_{10}^\ell)$ = (4.5, 2.0), (6.0, 2.0), (3.0, 2.0), (4.5, 3.6), (4.5, 0.4), (3.8, 1.2)

Equations (5.5)-(5.7) will, thus, reduce to

$$\text{minimize} \qquad U(\underset{\sim}{\phi}) = \max_{i \in N_1} \left| P_i(\underset{\sim}{\phi}) - P_R(\underset{\sim}{\phi}) \right| , \tag{5.24}$$

$$\text{subject to} \qquad c_j(\underset{\sim}{\phi}) = P_{Dj}(\underset{\sim}{\phi}) - \frac{1}{d} \left[\frac{8}{\pi} H_c + \frac{2v}{\mu_w} \right] \geq 0 \ , \ j \in N_2, \tag{5.25}$$

$$c_k(\underset{\sim}{\phi}) \geq 0 \qquad , \ k \in N_3, \tag{5.26}$$

where $\underset{\sim}{\phi}$, N_1, N_2 and N_3 are given by (5.8)-(5.11) and $P_{Dj}(\underset{\sim}{\phi})$ is the quadratic polynomial approximation to the potential well gradient at point j, that is

$$P_{Dj}(\underset{\sim}{\phi}) \quad \frac{\partial H_{zj}(\underset{\sim}{\phi})}{\partial X} \ , \ j \in N_2. \tag{5.27}$$

The FORTRAN IV program FLOPT4 for least pth optimization with extrapolation to minimax solutions (Bandler and Sinha 1977) is used to solve the constrained minimax problem defined above in (5.24)-(5.26). In this program, the Bandler-Charalambous technique (1974) is used to transform the constrained nonlinear programming problem into an unconstrained minimax problem. A least pth objective function is then formulated and the minimax solution is obtained by using a slightly modified version of the quasi-Newton method (Fletcher 1972).

5.6 Examples

Kryder, Ahn and Powers (1975) reported a 1.5×10^{10} bits/m^2 bubble memory chip with 2 μm bubbles in GdCoMo amorphous films using T-I propagation structures with parameters as shown in Fig. 4.14. The amorphous film has a coercive field of 240 ± 80 A/m and for s = 0.3 μm, good quasistatic operation with a bias field margin of about 2400 A/m is obtained for $H_T \geq 4800$ A/m.

The optimization procedure of Sections (5.4) and (5.6) is used to obtain, independently, the optimum spacer and bubble height which will minimize the difference between the well depths at points A and B, of Fig. 4.14, as well as satisfying (5.6) in the middle of the gap. In the rest of this section a discussion is presented for the effect of the spacer and the bubble height on the circuit performance using this model.

5.6.1 Spacer Effect

Keeping ℓ_1, ℓ_2, w, t, g, h, d and M_B fixed at the values shown in Fig. 4.14, and leaving s and H_T to vary in the ranges

$$0.05 \leq s \leq 0.45 \ \mu m \ , \qquad (5.28)$$

$$1200 \leq H_T \leq 5000 \ A/m \ , \qquad (5.29)$$

the optimization procedure gives the results shown in Table 5.3(a).

TABLE 5.3(a)

RESULTS OF THE OPTIMIZATION PROCEDURE
FOR THE T-I CIRCUIT OF FIG. 4.14
(SPACER EFFECT)

PARAMETER	INITIAL VALUE	FINAL VALUE
s(μm)	0.25	0.3874
H_T(A/m)	2500	4604

H_c = 240 A/m
μ_W = 8 x 10^6 m^2/A s
v = 0
h = 2.08 μm

CDC-6400 computer time:
for the quadratic approximation = 600 s
for the optimization procedure = 3 s

Although one might think that decreasing the spacer may result in better operation because of the resulting better bubble-permalloy coupling, yet the results of Table 5.3(a) show the opposite. When the spacer is increased from 0.25 μm to 0.3874 μm, all optimization criteria are satisfied and propagation is achieved across the gap. This is in agreement with the initial suggestions by George, Hughes and Archer (1974) for single permalloy bars. The increase in the spacer thickness results in more uniform distribution of the permalloy stray field across the bubble and, hence, in higher field differential ΔH_z.

5.6.2 Bubble Height Effect

Table 5.3(b) gives the results obtained using the optimization procedure, when h is left to vary in the range

$$1.5 < h \leq 3.0\ \mu m\ . \qquad (5.30)$$

TABLE 5.3(b)

RESULTS OF THE OPTIMIZATION PROCEDURE
FOR THE T-I CIRCUIT OF FIG. 4.14
(BUBBLE HEIGHT EFFECT)

PARAMETER	INITIAL VALUE	FINAL VALUE
$h(\mu m)$	2.0	1.75
$H_T(A/m)$	2500	4000
$s = 0.3\ \mu$		

The fact that smaller bubble height results in better propagation can be attributed to the higher resulting z-directed permalloy field on the bubble. Again, for rectangular bars, George, Hughes and Archer (1974) predicted that better operation could be obtained by reducing the bubble height which agrees with this analysis.

5.7 Discussion

Fig. 5.2 shows the potential well profiles along the bubble path for the T-I circuit of Fig. 4.14. Three cases, numbered 1, 2 and 3 are considered which correspond to the initial parameters of Table 5.3(a), the final parameters of Table 5.3(a) and the final parameters of Table 5.3(b), respectively. It is seen that, while the constraint (5.6) is not satisfied in case 1 in the middle of the gap, it is satisfied for cases 2 and 3. It is noted that the effect of reducing the bubble height is stronger than that of increasing the spacer since the former results in lower in-plane field amplitude. On the other hand, Thiele (1969) proved that the stability of bubble domains is largely dependent on the ratio of the diameter to the height. Therefore the upper and lower limits on the domain height are more critical than those on the spacer.

The analysis of Sections 5.2 - 5.5 can be used to compute the minimum in-plane propagation field, for any bubble-permalloy configuration, as a function of the bubble velocity. This is done by allowing the circuit parameters to vary over very narrow ranges and thus are effectively kept constant. For the circuit of Fig. 4.14 and allowing the spacer to vary in the range

$$0.295 \leq s \leq 0.305 \ \mu\text{m} \ , \qquad (5.31)$$

the minimum in-plane fields required for quasistatic and high frequency propagation, with minimum bubble size fluctuations, are shown in Table 5.4. The measured value is reported by Kryder, Ahn and Powers (1975) and is also shown in Table 5.4. The discrepancy between the two results

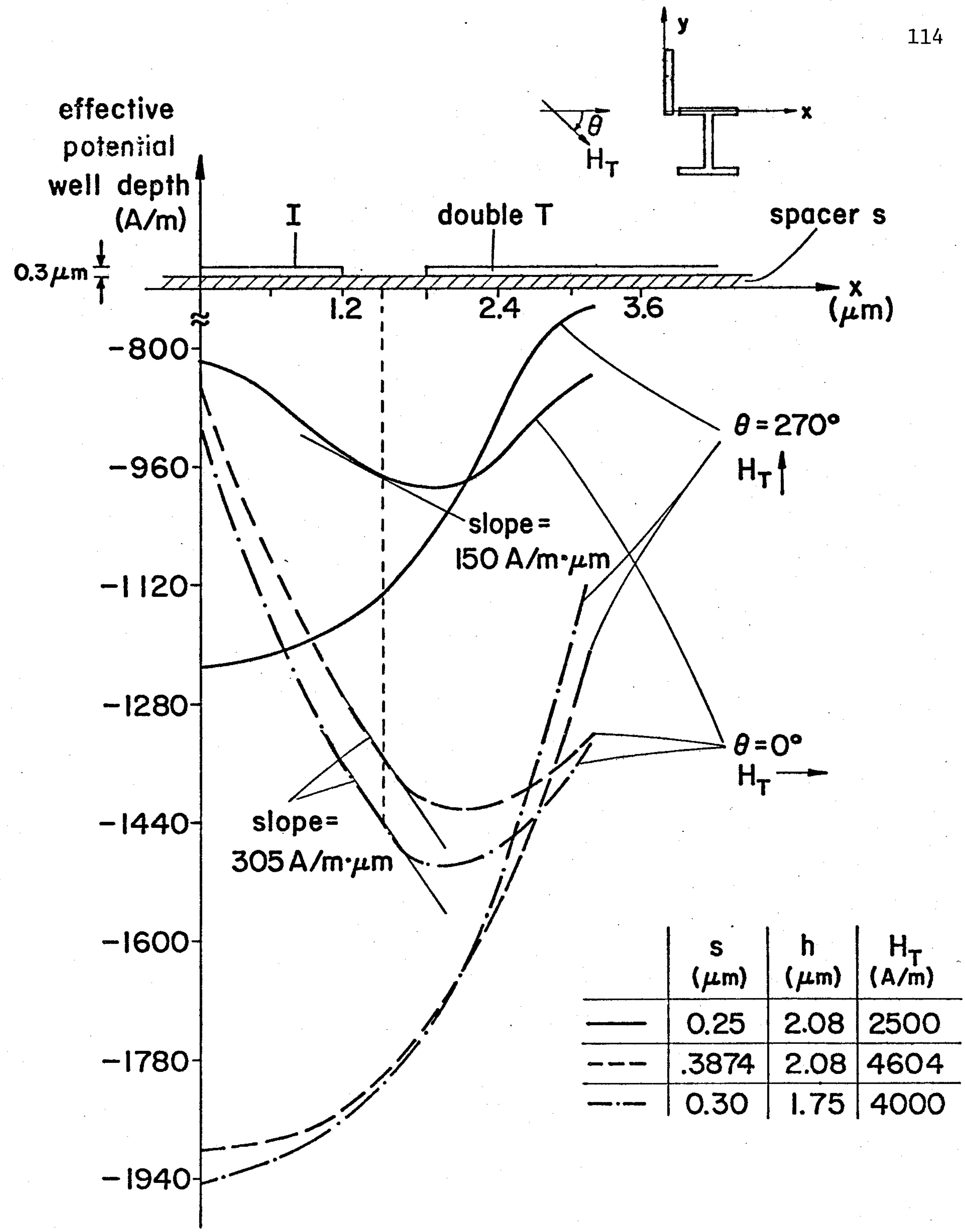

Figure 5.2 Optimized potential well profiles for the T-I circuit of Fig. 4.14.

can be attributed to the errors in the measuring of the coercivity and the height of the bubble materials and the errors in approximating the potential well depth.

TABLE 5.4

MINIMUM IN-PLANE PROPAGATION FIELD
FOR THE T-I CIRCUIT OF FIG. 4.14

BUBBLE VELOCITY (m/s)	COMPUTED MINIMUM IN-PLANE FIELD (A/m)	MEASURED MINIMUM IN-PLANE FIELD (A/m)
0	2800	2080
10	5900	-

$s \simeq 0.3\ \mu m$
$h = 2.08\ \mu m$
$\mu_w = 0.125\ m^2/A\ s$

5.8 Conclusions

The optimization procedure discussed in detail, in this chapter can be used in optimizing the permalloy shape required to propagate bubble domains in a given uniaxial magnetic material . By allowing the permalloy parameters ℓ_1, ℓ_2, w, t, g of (5.4) to vary and by solving the minimax optimization problem of Section 5.5, one can expect to obtain the optimum permalloy configuration that will assure bubble propogation across the circuit's critical points as well as minimizing the bubble size fluctuations. The effect of varying the permalloy parameters, however, has not been studied in this thesis because of computer time limitations. The demagnetizing factors should be updated each time any of the permalloy parameters changes and this requires large amounts of computer time. However, this is a reliable method of optimization and is much less expensive than trying the design by a cut-and-try method.

In conclusion, a novel optimization procedure for propagation circuit optimization has been presented in detail. The algorithm minimizes bubble size fluctuations and, hence minimizes the possibility of improper propagation or loss of information. It also assures propagation along the specified bubble path. An example has been worked out and the effect of two circuit parameters has been discussed. Comparison to experimentally measured in-plane field values shows agreement with the computed values.

CHAPTER 6

CONCLUSIONS

In this thesis, the problem of modeling and optimization of field access bubble propagation circuits has been considered. The micromagnetic approach for modeling of bubble circuits, presented in Chapter 3, is general enough to consider the domain and domain wall structure in the permalloy which is important in studying submicron bubble devices. The concept of the continuum modeling of permalloy circuits requires reasonable computer time and memory. The use of iterative procedure to compute the magnetization in the permalloy allows the inclusion of various energy terms in the total permalloy energy, such as coercivity.

The analysis of various bubble propagation circuits reveal the relative merits of these circuits. The potential well profiles of half-disk circuits show little variations in the well depths along the propagation track. These result in small bubble size fluctuations and, hence, improved operation. The analysis of the asymmetric chevrons shows the reason for the improvements in bubble propagation as compared to the symmetric chevron circuits.

The bubble size and position fluctuation algorithm of Chapter 4 is useful in detecting improper propagation (stripping-out of bubbles) and loss of information (collapsing of bubbles) in any propagation circuit. The algorithm allows the use of such different stability analyses as Thiele's theory (1969) or DeBonte's method (1975) for high and low Q bubbles, respectively.

An algorithm for bubble circuit optimization has been introduced in Chapter 5. The objective is to minimize the bubble size fluctuation along the propagation track and to assure propagation across the critical points in the propagation circuit. To reduce the computation time required in the optimization procedure, a quadratic polynomial approximation to the potential well depth is used which proved accurate and efficient. The optimization algorithm can be used to obtain the optimum shape for the permalloy circuit or the optimum bubble material parameters which meet the required specifications.

This research work has revealed various promising topics for further investigation such as:

(1) A technique for the optimization of the under-relaxation factor β to reduce the number of iterations required in both the micromagnetic and the magnetization algorithms.

(2) Investigation of other techniques of setting up the discretization mesh in the permalloy circuit to reduce the computer time required for evaluating the demagnetizing field distribution for the micromagnetic analysis of submicron bubble circuits.

(3) Modification of the bubble size fluctuation algorithm to include analysis for elliptical bubbles. This is important for studying bubble generators and replicators where the bubble is stretched before cutting.

(4) Applying the optimization algorithm of Chapter 5 to a specific permalloy structure and allowing the permalloy parameters to vary

until the optimum shape is obtained. This is very useful for gap tolerant circuits and, specifically, for half-disks since a wide variety of disk shapes is being used now and it would be beneficial to compute the optimum disk shape.

(5) Implementation of an algorithm for automatic calculation of the upper and lower bounds on each of the propagation circuit parameters, as discussed in Chapter 5. It is important, for example, to define the bounds on the bubble height and saturation magnetization, which assure bubble stability, before using the optimization algorithm.

APPENDIX A

RELATIONSHIPS BETWEEN SI AND CGS UNITS

Table A.1 gives the conversion relations between the SI and the CGS systmes of units for various bubble material parameters (Bobeck and Della Torre 1975).

TABLE A.1

RELATIONSHIPS BETWEEN SI AND CGS UNITS

Physical quantity	SI Symbol	SI Unit	CGS Symbol	CGS Unit	Conversion relation
Flux	ϕ_m	Weber	ϕ_m	Maxwell	1 Wb = 10^8Mx
Flux density	B	Tesla(Wb/m^2)	B	Gauss(Mx/cm^2)	1 T = 10^4 G
Field intensity	H	A/m	H	Oersted	1 A/m = $4\pi \times 10^{-3}$ Oe
Magnetization	M	A/m	I	emu	1 A/m = 10^{-3} emu 1 kA/m = 1 emu
Wall energy	σ_w	J/m^2	σ_w	erg/cm^2	1 J/m^2 = 10^3 erg/cm^2 1 mJ/m^2 = 1 erg/cm^2
Uniaxial anisotropy constant	K_u	J/m^3	K_u	erg/cm^2	1 J/m^3 = 10 erg/cm^2
Mobility	μ_w	m^2/A s	μ_w	cm/s Oe	1m^2/A s = $10^5/4\pi$ cm/s Oe
Constitutive equation	$B = \mu_o(H + M)$		$B = H + 4\pi I$		
Free space	$\mu_o = 4\pi \times 10^{-7}$		1		
Material length	$\ell_m = \frac{\sigma_w}{\mu_o M_B^2}$		$m = \frac{\sigma_w}{4\pi I_s^2}$		
Anisotropy field	$H_K = \frac{2K_u}{\mu_o M_B}$		$H_K = \frac{2K_u}{I_s}$		
Quality factor	$Q = \frac{H_K}{M_B} = \frac{2K_u}{\mu_o M_B^2}$		$Q = \frac{2K_u}{4\pi I_s^2}$		

APPENDIX B

COMPUTATION OF THE DEMAGNETIZING FACTORS

The scalar magnetic potential of a magnetized body is given by (Della Torre and Longo 1969)

$$\psi_{mag}(\underset{\sim}{r}_{ij}) = \frac{1}{4\pi} \int_{V_j} \underset{\sim}{M}(\underset{\sim}{r}_j) \cdot \underset{\sim}{\nabla}_i \left(\frac{1}{r_{ji}}\right) dV_j \ , \qquad \text{(B.1)}$$

where the different parameters are as defined in Fig. 3.4. Using integration by parts it can be shown that the magnetic potential of a magnetized body is due to both surface and volume charges. The demagnetizing field, which is set up by the magnetization inside the body, is then given by

$$\underset{\sim}{H}_D(\underset{\sim}{r}_i) \triangleq - \underset{\sim}{\nabla}_i \ \psi_{mag}(\underset{\sim}{r}_i) = - \frac{1}{4\pi} \underset{\sim}{\nabla}_i \int_{V_j} \underset{\sim}{M}(\underset{\sim}{r}_j) \cdot \underset{\sim}{\nabla}_j \left(\frac{1}{r_{ji}}\right) dV_j \ . \qquad \text{(B.2)}$$

Using Cartesian-coordinate system, one can define F_1 by

$$F_1 \triangleq \underset{\sim}{M}(\underset{\sim}{r}_j) \cdot \underset{\sim}{\nabla}_j \left(\frac{1}{r_{ji}}\right) = \frac{M_x(\underset{\sim}{r}_j)\ (x_i-x_j) + M_y(\underset{\sim}{r}_j)\ (y_i-y_j)}{\left[d_{ij}^2 + (z_i-z_j)^2\right]^{3/2}} \ , \qquad \text{(B.3)}$$

where

$$\underset{\sim}{r}_i = x_i \ \underset{\sim}{1}_x + y_i \ \underset{\sim}{1}_y \qquad \text{(B.4)}$$

$$d_{ij}^2 = (x_i-x_j)^2 + (y_i-y_j)^2 \qquad \text{(B.5)}$$

and the z-component of the magnetization is neglected. Integrating w.r.t. z_j from -t/2 to +t/2, where t is the permalloy thickness, gives

$$\int_{-t/2}^{t/2} F_1 \, dz_j = \{F_2 \, M_x(\underset{\sim}{r}_j) + F_3 \, M_y(\underset{\sim}{r}_j)\} \, \underset{\sim}{1}_x$$

$$+ \{F_4 \, M_x(\underset{\sim}{r}_j) + F_5 \, M_y(\underset{\sim}{r}_j)\} \, \underset{\sim}{1}_y \; , \tag{B.6}$$

where

$$F_2 = \frac{(x_i - x_j)^2}{d_{ij}^4} \{d_{ij}^2 \, F_6 - F_7\} \quad , \tag{B.7}$$

$$F_3 = \frac{2(x_i - x_j)(y_i - y_j)}{d_{ij}^4} \; \frac{d_{ij}^2}{2} \{F_6 - F_7\} \; = F_4 \; , \tag{B.8}$$

$$F_5 = \frac{(y_i - y_j)^2}{d_{ij}^4} \{d_{ij}^2 \, F_6 - F_7\} \quad , \tag{B.9}$$

$$F_6 = - \frac{(z_i + t/2)}{F_8^{3/2}} + \frac{(z_i - t/2)}{F_9^{3/2}} \quad , \tag{B.10}$$

$$F_7 = \frac{(z_i + t/2)}{F_8^{1/2}} - \frac{(z_i - t/2)}{F_9^{1/2}} \; , \tag{B.11}$$

$$F_8 = d_{ij}^2 + (z_i + t/2)^2 \quad , \tag{B.12}$$

$$F_9 = d_{ij}^2 + (z_i - t/2)^2 \quad . \tag{B.13}$$

The terms in (B.6) can be integrated over the permalloy thickness to get the average demagnetizing field or solved for z_i = t/2 to get the demagnetizing field at the film's mid plane. Using the former method, the average terms will be

$$D_{xx}(\underset{\sim}{r}_i;\underset{\sim}{r}_j) \triangleq \frac{1}{t}\int_{-t/2}^{t/2} F_2\, dz_i = \frac{1}{4\pi}\left(\frac{-2}{td_{ij}^4}\right)\left\{(x_i-x_j)^2\left[\frac{d_{ij}^2+2t^2}{\sqrt{d_{ij}^2+t^2}} - d_{ij}\right] - \left[\frac{d_{ij}^2(d_{ij}^2+t^2)}{\sqrt{d_{ij}^2+t^2}} - d_{ij}^3\right]\right\} , \tag{B.14}$$

$$D_{xy}(\underset{\sim}{r}_i;\underset{\sim}{r}_j) \triangleq \frac{1}{t}\int_{-t/2}^{t/2} F_3\, dz_i = \frac{1}{4\pi}\left(\frac{-2}{td_{ij}^4}\right)\left\{(x_i-x_j)(y_i-y_j)\left[\frac{d_{ij}^2+2t^2}{\sqrt{d_{ij}^2+t^2}} - d_{ij}\right]\right\}$$

$$\triangleq D_{yx}(\underset{\sim}{r}_i;\underset{\sim}{r}_j) \quad , \tag{B.15}$$

and $D_{yy}(\underset{\sim}{r}_i;\underset{\sim}{r}_j)$ is obtained from (B.14) by interchanging the x's and the y's.

To obtain (3.53), an interpolation function is required. Greville (1969) suggested a cubic-spline interpolation algorithm which tries fitting to n points the smoothest interpolation function. This algorithm, which is available as a set of subroutines in IMSL library (1977), was used to express I(i;j) in (3.46) and (3.47).

Singularity Analysis

It is noted that the coefficients in (B.14) and (B.15) are infinite when $d_{ij} = 0$. This occurs when $x_i = x_j$ and $y_i = y_j$. Since the integrals in (3.53) are performed over all points in the permalloy, a singularity appears in the integrand.

Since analytical integration of the expressions in (B.14) and (B.15) is difficult, the technique used to avoid the singular integrand is to enclose the point of singularity by an infinitismally small rectangle (region S) as shown in Fig. B.1. The integration in (3.53) is done numerically in region N and the equivalent analytical value (Joseph and Schlomann 1965) of the integral is used to replace the integration over region S. Five different types of region S are illustrated in Fig. B.1 corresponding to different kinds of singularities. These are interior, 90° corner, 270° corner, x-edge and y-edge singularities as shown in Fig. B.1(a)-(e), respectively.

Since the coefficients in (B.14) and (B.15) decrease rapidly as d_{ij} increases, a large number of points should be considered around the singular points. Figure B.2 illustrates the mesh of points established over region N in a 90° corner singularity.

A typical example of a rectangular permalloy bar has the following parameters:

$$\ell = 15\ \mu m$$

$$w = 3\ \mu m$$

$$t = 0.4\ \mu m$$

$$\Delta x = \Delta y = 0.75\ \mu m$$

$$\delta x = \delta y = 0.0375\ \mu m$$

$$N_{xs} = N_{ys} = 21 \text{ points.}$$

It is noted that reducing the dimensions of region S further than the values given above does not result in appreciable change in the singularity contribution to the total integral value.

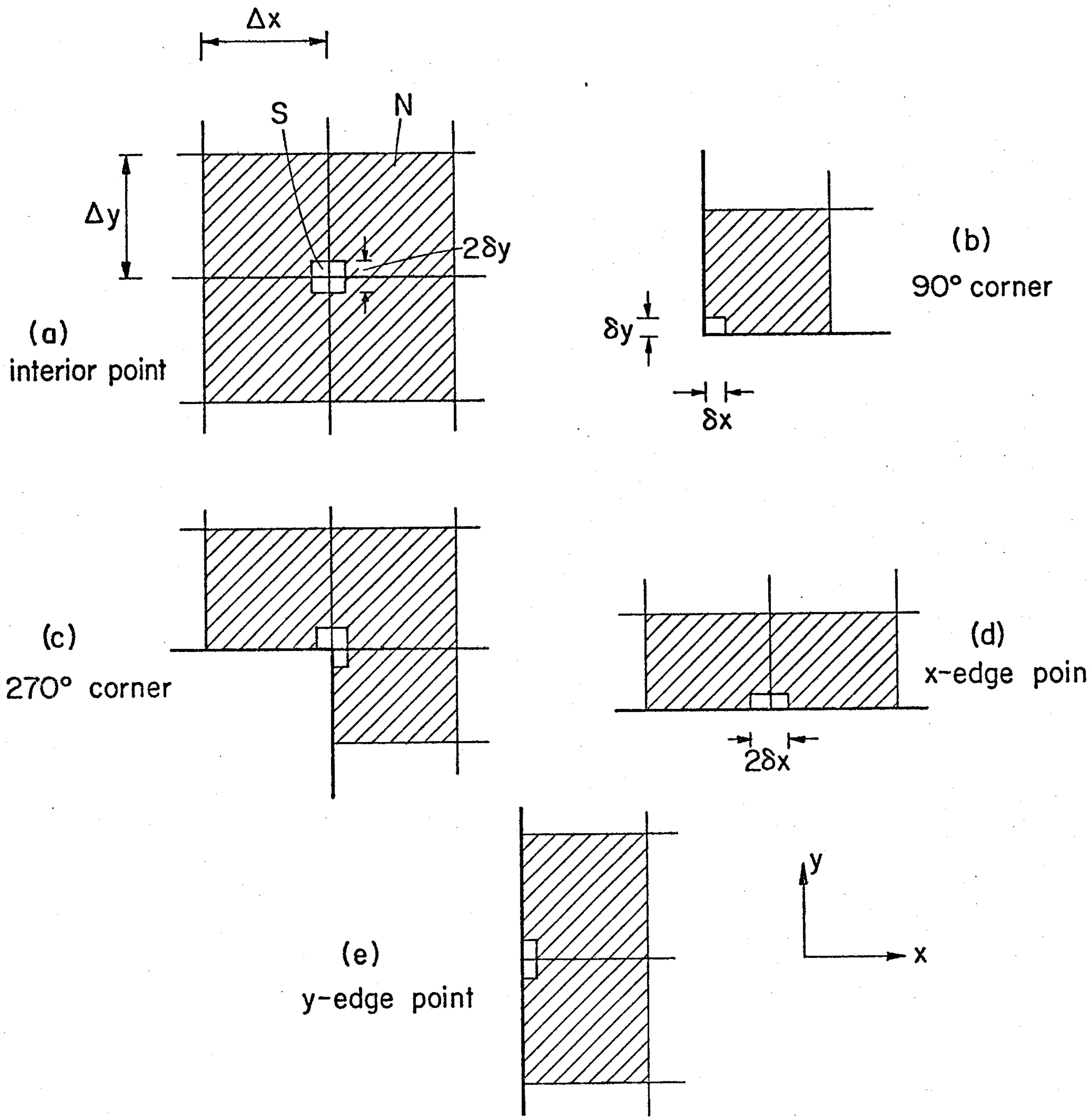

Figure B.1 Various kinds of singularities that appear in the computation of the demagnetizing field: (a) interior, (b) 90° corner, (c) 270° corner, (d) x-edge and (e) y-edge singularities. Region S is singular and N is nonsingular.

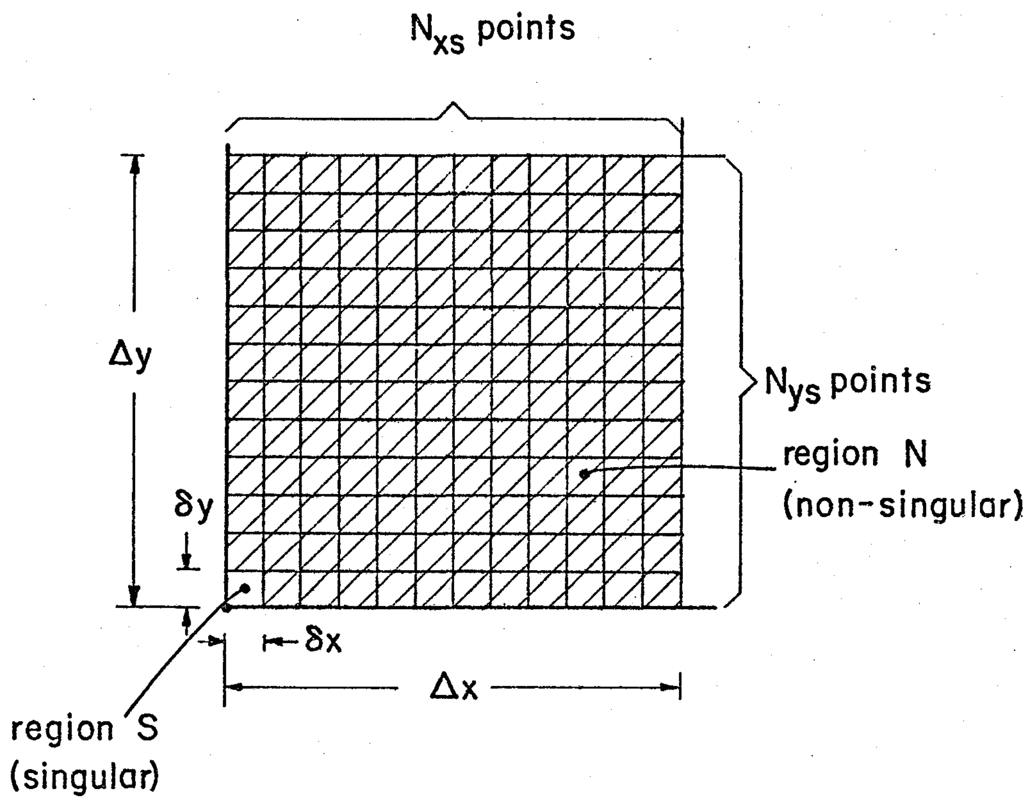

Figure B.2 The discretization mesh used to compute the contribution of a singular corner point to the demagnetizing field.

<u>The Demagnetizing Factors</u>

The substitution of constant x and y magnetization components in (3.49) gives

$$\underset{\sim}{H}_{Dx} = \underset{\sim}{M}\,(C_{xx} + C_{xy}) \quad , \tag{B.16}$$

$$\underset{\sim}{H}_{Dy} = \underset{\sim}{M}\,(C_{yx} + C_{yy}) \quad , \tag{B.17}$$

where $\underset{\sim}{M}$ is the constant magnetization. Therefore, the demagnetizing factors of the body at point i are given by

$$N_{k\ell}(i) = -\sum_{j=1}^{N} C_{k\ell}(i,j) \quad , \tag{B.18}$$

which is equivalent to adding the elements of each row in the matrix C of (3.52). Figure 3.6 gives the demagnetizing factors of a rectangular permalloy bar of dimensions 15 x 3 x 0.4 μm obtained using (B.18).

APPENDIX C

THE EXCHANGE ENERGY

The exchange energy forms an important part of the total energy of many solids. Heisenberg showed that it also plays a decisive role in ferromagnetism. If two atoms m and n have spin angular momentum $\underset{\sim}{S}_m \hbar$ and $\underset{\sim}{S}_n \hbar$, respectively, then the exchange energy between them is given by

$$E_{EX} = - 2\, J_{EX}\, \underset{\sim}{S}_m \cdot \underset{\sim}{S}_n = - 2\, J_{EX}\, S_m\, S_n \cos \delta \qquad (C.1)$$

where J_{EX} is a particular integral, called the exchange integral, and δ is the angle between the spins. If J_{EX} is positive, E_{EX} is a minimum when $\cos \delta = 1$ and a maximum when $\cos \delta = -1$. If J_{EX} is negative, the lowest energy results from antiparallel spins. Since ferromagnetism is due to alignment of spin moments on adjacent atoms, a positive value of J_{EX} is therefore necessary for ferromagnetism to occur. The only three elements with positive J_{EX} are iron, nickel and cobalt (Cullity 1972).

It can be shown (Brown 1963) that the exchange field of an infinitismal volume in a magnetic body is given by (3.17) where

$$A_{EX} = \frac{q\, J_{EX}\, S^2}{a_\ell} \qquad (C.2)$$

is the exchange constant, a_ℓ is the lattice parameter, q is 2 for BCC structure and 4 for FCC structure, and $\underset{\sim}{1}_M$ is a unit vector along the magnetization of that infinitismal volume.

Assuming that a unit vector $\underset{\sim}{1}_M$ is inclined at an angle θ_M to the x-axis, as shown in Fig. C.1(a), then

$$\underset{\sim}{1}_M = \cos\theta_M \, \underset{\sim}{1}_x + \sin\theta_M \, \underset{\sim}{1}_y \quad , \tag{C.3}$$

where

$$\theta_M \triangleq \theta_M(x,y) \quad . \tag{C.4}$$

Since

$$\frac{\partial}{\partial x}\cos\theta_M = -\sin\theta_M \cdot \theta_{M_x} \quad , \tag{C.5}$$

$$\frac{\partial}{\partial x}\sin\theta_M = \cos\theta_M \cdot \theta_{M_x} , \tag{C.6}$$

$$\frac{\partial^2}{\partial x^2}\cos\theta_M = -\sin\theta_M \cdot \theta_{M_{xx}} - \cos\theta \, (\theta_{M_x})^2 , \tag{C.7}$$

$$\frac{\partial^2}{\partial x^2}\sin\theta_M = \cos\theta_M \cdot \theta_{M_{xx}} - \sin\theta_M \, (\theta_{M_x})^2 , \tag{C.8}$$

and similarly for the derivatives with respect to y, then (3.36) and (3.37) follow.

Figure C.1(b) shows a mesh of points centered around point (m,n). Using central difference approximations for first and second derivatives, the terms in (3.36) and (3.37) can be approximated as

$$\theta_{M_x}(m,n) \approx \frac{\theta_M(m+1,n) - \theta_M(m-1,n)}{2\,\Delta x} , \tag{C.9}$$

$$\theta_{M_{xx}}(m,n) \approx \frac{\theta_M(m+1,n) - 2\,\theta_M(m,n) + \theta_M(m-1,n)}{(\Delta x)^2} , \tag{C.10}$$

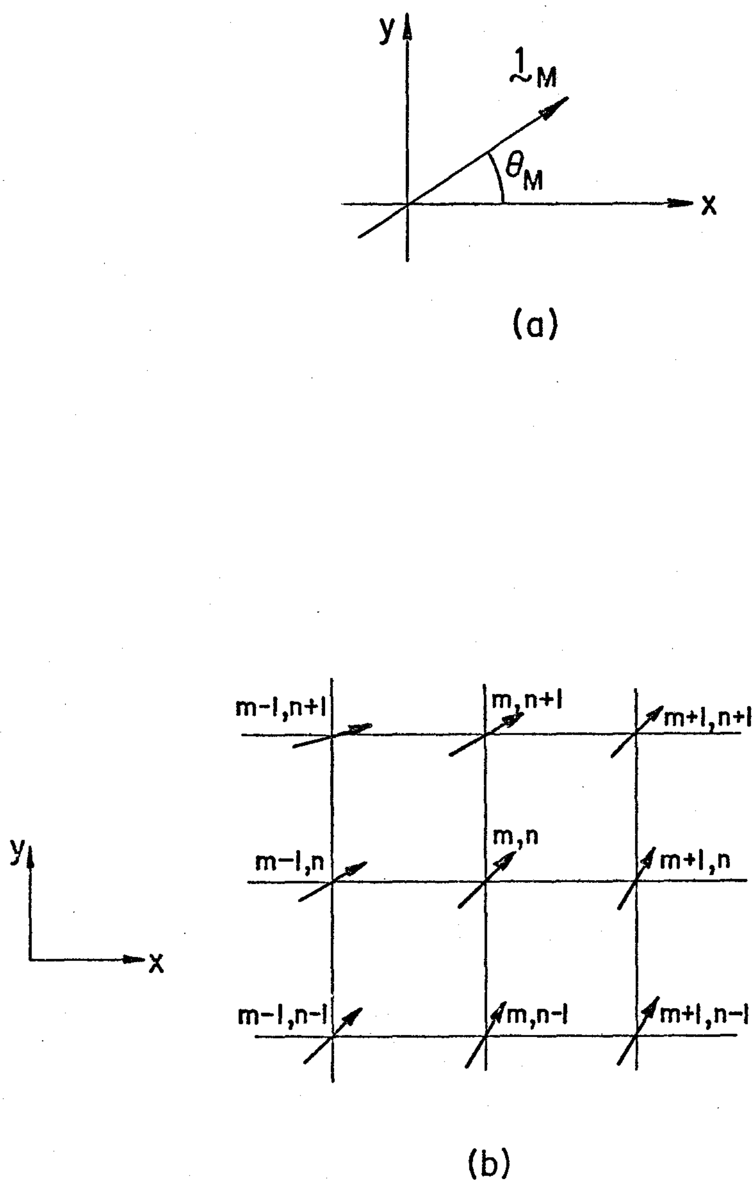

Figure C.1 A (a) unit vector inclined at angle θ to the x-axis and (b) a mesh of points centered around point (m, n).

$$\theta_{M_y}(m,n) \simeq \frac{\theta_M(m,n+1) - \theta_M(m,n-1)}{2\,\Delta y} \quad , \tag{C.11}$$

$$\theta_{M_{yy}}(m,n) \simeq \frac{\theta_M(m,n+1) - 2\,\theta_M(m,n) + \theta_M(m,n-1)}{(\Delta y)^2} \quad . \tag{C.12}$$

APPENDIX D

M-H APPROXIMATIONS

Let us assume that a magnetic body has an average demagnetizing factor N_k in a certain direction, k. If a field H_A is applied to the body along the k direction, a demagnetizing field H_D results and the total local field will be

$$\begin{aligned} \underset{\sim}{H}_L &= \underset{\sim}{H}_A + \underset{\sim}{H}_D \\ &= \underset{\sim}{H}_A - N_k \underset{\sim}{M}_k \quad , \end{aligned} \tag{D.1}$$

where M_k is the average magnetization along the applied field direction. A curve of M_k vs. H_L can be obtained from an M_k-H_A curve by a graphical method (Cullity 1972). In Fig. D.1, OA is a M_k-H_A curve. The dashed line OC is a plot of the relation $H_D = - N_k M_k$ and has a slope of $-1/N_k$. If we plot OC with an equal but positive slope, it becomes OD. Therefore, if OD and OA are sheared to the left by an amount sufficient to make OD vertical, OA will then be a curve of M_k as a function of the local field H_L. It is clear that the apparent susceptibility χ_{app}, given by M_k/H_A, is much less than the true susceptibility χ_{true}, or M_k/H_L. It can be shown , using (D.1), that

$$\frac{1}{\chi_{true}} = \frac{1}{\chi_{app}} - N_k \quad . \tag{D.2}$$

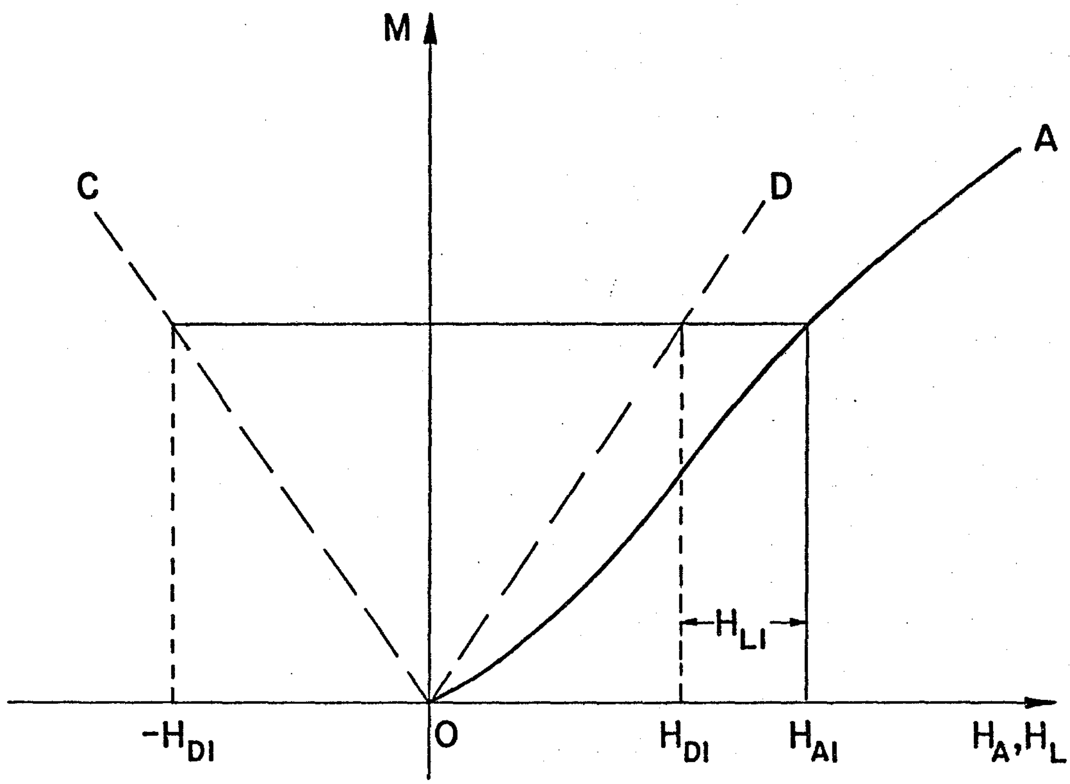

Figure D.1 The M-H_A and the M-H_L relations. When OD and OA are sheared to the left by an amount sufficient to make OD vertical, OA will then give the M-H_L relation.

In general, for permalloy bars, N_k is not constant but varies along the bar's length and width. Nevertheless, the above discussion can be applied to these bars by using their average demagnetizing factors. The conclusion, therefore, is that the M-H_L relation resembles the M-H_A relation but with higher susceptibility.

Various M-H_A relations for permalloy bars were examined using the results of Doyle and Casey (1974), Krinchik, Chepurova, Shamatov, Raev and Andreev (1975) and Ma (1976). In general M varies nonlinearly with H_A but for most bars the relation is linear at low applied fields and asymptotically reaches M_s at high fields.

The relation

$$M/M_s = t_1(H_L/H_t)^2 - k, \qquad H_L \leq H_t \quad , \tag{D.3}$$

$$M/M_s = (t_1-k) + \frac{2}{\pi}(1-t_1+k)\tan^{-1}\left(\eta \frac{H_L-H_t}{H_t}\right), \; H_L \geq H_t, \tag{D.4}$$

where the parameters t_1, H_t and η are shown in Fig. D.2, represents an M-H_L relation for a material with coercive field

$$H_C = H_t \sqrt{k/t_1} \ . \tag{D.5}$$

The continuity of the first derivatives of (D.3) and (D.4) is achieved by choosing

$$t_1 = \frac{\eta(1+k)}{\pi+\eta} \quad , \tag{D.6}$$

where η determines the curvature of (D.4). For the special case where $k \ll 1$, $\eta = 1$ and $H_t \gg H_C$,

$$t_1 \simeq 1/(\pi+1) \quad , \tag{D.7}$$

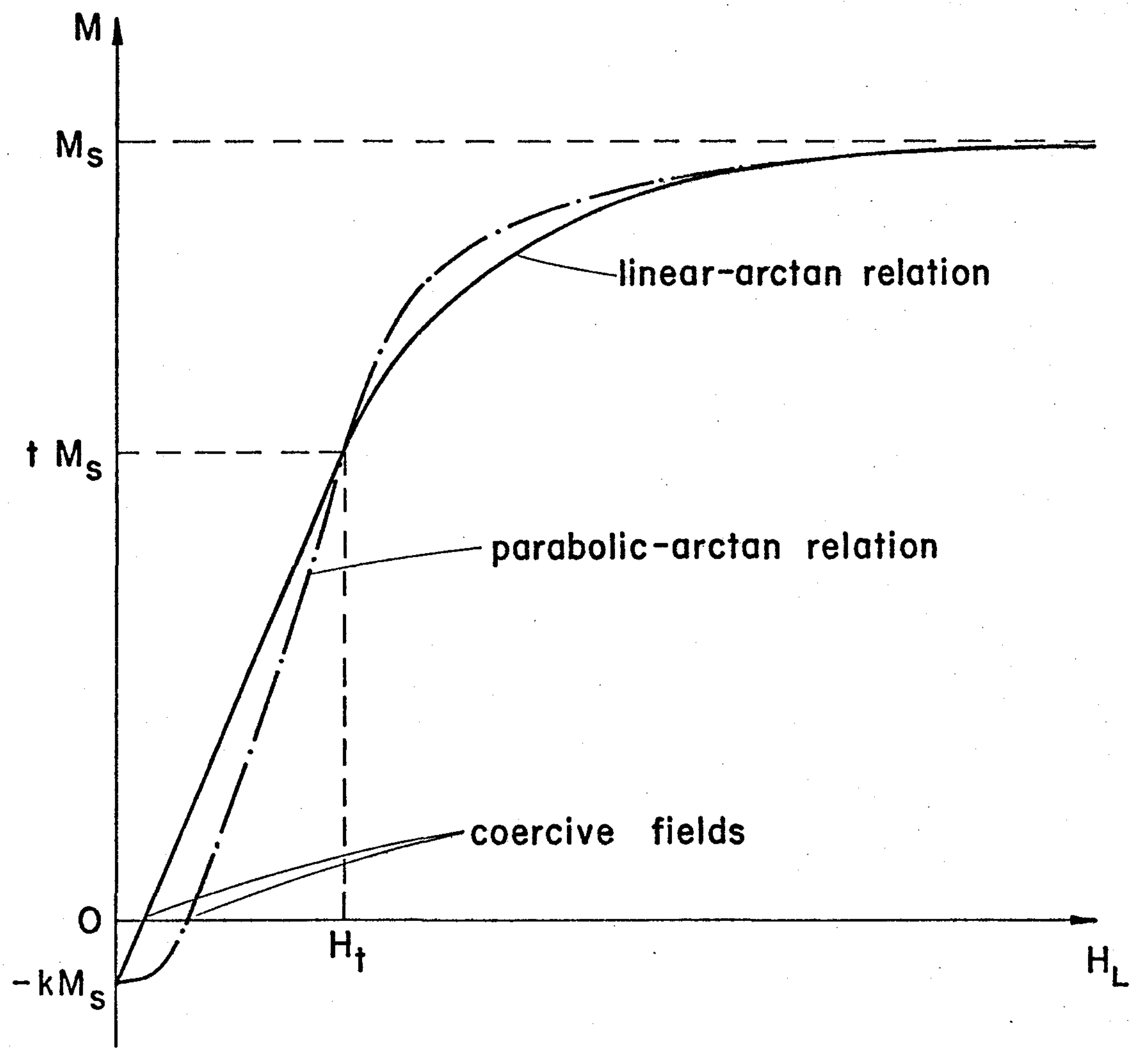

Figure D.2 Linear-arctan and parabolic-arctan M-H_L approximations.

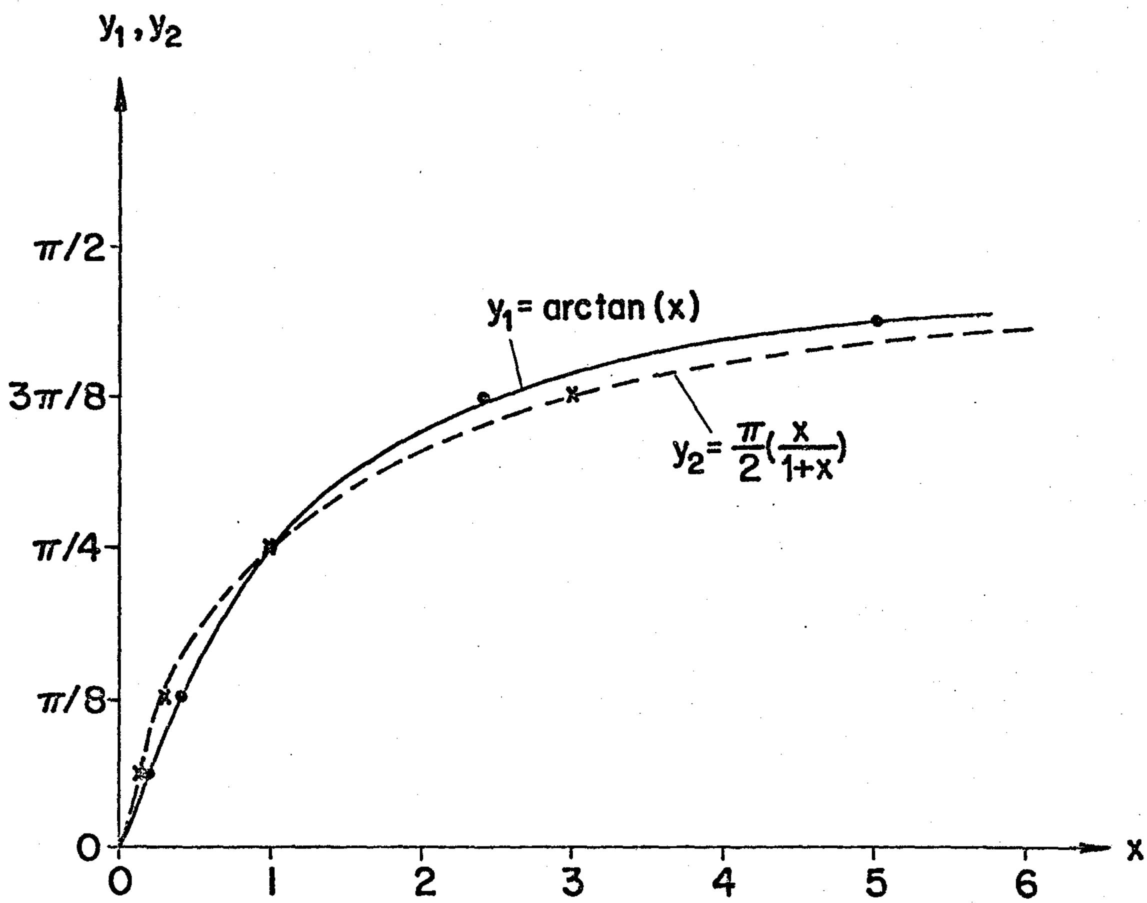

Figure D.3 Approximating arctan (x) by a simpler function.

and the approximate susceptibility is given by

$$\chi \approx \frac{M_s}{(1+\pi)H_t} \tag{D.8}$$

which is about 300 for H_t= 650 A/m and M_s = 800,000 A/m.

The linear-arctan relation (3.55) and (3.56), shown in Fig. D.2, can also be used to represent the permalloy M-H_L characteristics.

In conclusion, it is noted that the M-H_L relation given by (D.3) and (D.4) represents a wide variety of curves with the required properties. A great deal of computer time can be saved, however, using

$$\tan^{-1}(x) \approx \frac{\pi}{2}\,\frac{x}{x+1} \quad , \tag{D.9}$$

as shown in Fig. D.3.

The computer program written for the magnetization algorithm of Chapter 3 accepts the specific M-H_L approximation in a separate subroutine. This allows using an experimentally determined permalloy characteristic.

REFERENCES

H.L. Abdel-Malek (1977), "A unified treatment of yield analysis, worst-case design and yield optimization", Faculty of Engineering, McMaster University, Hamilton, Canada, Report SOC-182.

H.L. Abdel-Malek and J.W. Bandler (1978a), "Yield optimization for arbitrary statistical distributions, Part I: Theory". Proc. IEEE Int. Symp. Circuits and Systems (New York).

H.L. Abdel-Malek and J.W. Bandler (1978b), "Subroutines for implementing quadratic models of surfaces in optimal design", Faculty of Engineering, McMaster University, Hamilton, Canada, Report SOC-191.

G.S. Almasi, G.E. Keefe, Y.S. Lin and D.A. Thompson (1971), "A magnetoresistive detector for bubble domains", J. Appl. Phys., vol. 42, pp. 1268-1269.

G.S. Almasi and Y.S. Lin (1976), "An analytical design theory for field-access bubble domain devices", IEEE Trans. Magn., vol. MAG-12, pp. 160-202.

G.S. Almasi, Y.S. Lin, E. Munro and M. Slusarczuk (1974), "Analytical model for bubble propagation", AIP Conf. Proc. Series, vol. 24, pp. 635-637.

J.L. Archer, L.R. Tocci, P.K. George and T.T. Chen (1972), "Magnetic bubble domain devices", IEEE Trans. Magn., vol. MAG-8, pp. 696-700.

J.W. Bandler and C. Charalambous (1974), "Nonlinear programming using minimax techniques", J. Optimization Theory and Appl., vol. 13, pp. 607-619.

J.W. Bandler and D. Sinha (1977), "FLOPT4 - a program for least pth optimization with extrapolation to minimax solutions", Faculty of Engineering, McMaster University, Hamilton, Canada, Report SOC-151.

S.L. Blank and J.W. Nielsen (1972), "The growth of magnetic garnets by liquid phase epitaxy", J. Crystal Growth, vol. 17, pp. 302-311.

A.H. Bobeck (1967), "Properties and device applications of magnetic domains in orthoferrites", BSTJ, vol. 46, pp. 1901-1925.

A.H. Bobeck, P.I. Bonyhard and J.E. Geusic (1975), "Magnetic bubbles - an emerging new memory technology", Proc. IEEE, vol. 63, pp. 1176-1195.

A.H. Bobeck and I. Danylchuk (1977), "Characterization and test results for a 272 K bubble memory package", IEEE Trans. Magn., vol. MAG-13, pp. 1370-1372.

A.H. Bobeck and E. Della Torre (1975), Magnetic Bubbles. Amsterdam: North-Holland.

A.H. Bobeck, R.F. Fischer and J.L. Smith (1972), "An overview of magnetic bubble-domain-material-device interface", AIP Conf. Proc. Series, vol. 5, pp. 45-55.

P.I. Bonyhard (1977), "A true swap gate for magnetic bubble memory chips", IEEE Trans. Magn., vol. MAG-13, pp. 1785-1786.

P.I. Bonyhard, Y.S. Chen and J.L. Smith (1977), "High performance magnetic bubble replicate gate design", IEEE Trans. Magn., vol. MAG-13, pp. 1258-1260.

P.I. Bonyhard and J.L. Smith (1976), "68 k bit capacity 16 μm-period magnetic bubble memory chip design with 2 μm minimum features", IEEE Trans. Magn., vol. MAG-12, pp. 614-617.

M.A. Boyarchenkov, V.K. Raev, M.I. Samarin, A.M. Balbashov and A.Y. Chervonenkis (1971), "Magnetostatic interactions in some bubble-domain propagation circuits", IEEE Trans. Magn., vol. MAG-7, pp. 352-355.

W.F. Brown, Jr. (1963), Micromagnetics. New York: John Wiley.

W.F. Brown, Jr. (1977), private communications, September.

R. Bulirsch (1969), "Numerical calculations of elliptic integrals and elliptic functions III", Numer. Math., vol. 13, pp. 305-315.

H. Chang (1975), Magnetic Bubble Technology: Integrated-Circuit Magnetics for Digital Storage and Processing. New York: IEEE Press.

P. Chaudhari, J.J. Cuomo and R.J. Gambino (1973), "Amorphous metallic films for bubble domain applications", IBM J. of Res. and Development, vol. 17, pp. 66-68.

M.S. Cohen (1970), "Ferromagnetic properties of films", Handbook of Thin Film Technology, L.I. Maissel and R. Glang, Eds. New York: McGraw Hill.

J.A. Copeland (1972), "Magnetization of small permalloy circuit elements", J. Appl. Phys., vol. 43, pp. 1905-1908.

B.D. Cullity (1972), Introduction to Magnetic Materials. Reading, Mass.: Addison-Wesley.

I. Danylchuk (1971), "Operational characteristics of 10^3-bit garnet Y-bar shift register", J. Appl. Phys., vol. 42, pp. 1358-1359.

W.J. DeBonte (1975), "Twisted domain wall structure for stripe domains in bubble films", IEEE Trans. Magn., vol. MAG-11, pp. 3-11.

E. Della Torre and W. Ishak (1978), "Magnetization distributions and potential well profiles for gap tolerant bubble circuits", INTERMAG Conf. (Florence, Italy), to be presented. Also submitted to IEEE Trans. Magn.

E. Della Torre and W. Kinsner (1973), "The parallel-bar bubble propagating circuit", IEEE Trans. Magn., vol. MAG-9, pp. 298-303.

E. Della Torre and W. Kinsner (1975), "Channel-bar bubble propgating circuit", INTERMAG Conf. (London, England), paper #21-9.

E. Della Torre and C.V. Longo (1969), The Electromagnetic Field. Boston: Allyn and Bacon.

D.B. Dove, J.K. Watson, E. Huijer and H. Ma (1975), "A simplified Fourier series method for the calculation of magnetostatic interactions in bubble circuits", AIP Conf. Proc. Series, vol. 29, pp. 44-45.

D.B. Dove, J.K. Watson, H.R. Ma and E. Huijer (1976), "Permeability effects on the magnetization of thin permalloy I bars", J. Appl. Phys., vol. 47, pp. 2237-2238.

W.D. Doyle and M. Casey (1972), "The hysteretic properties of small soft magnetic bars", AIP Conf. Proc. Series, vol. 10, pp. 227-231.

W.F. Druyvesteyn, D.L.A. Tjaden and J.W.F. Dorleijn (1972), "Calculation of the stray field of a magnetic bubble, with application to some bubble problems", Philips Res. Repts., vol. 27, pp. 7-27.

J.S.Y. Feng and D.A. Thompson (1977), "Permeability of narrow permalloy stripes", IEEE Trans. Magn., vol. MAG-13, pp. 1521-1523.

W. Fleming (1978), private communications, January.

R. Fletcher (1972), "FORTRAN subroutines for minimization by quasi-Newton methods", Atomic Energy Research Establishment, Harwell, Berkshire, England, Report AERE-R7125.

P.K. George and J.L. Archer (1973a), "Magnetization distributions, magnetostatic energy barriers and drive fields for permalloy bars", J. Appl. Phys., vol. 44, pp. 444-448.

P.K. George and J.L. Archer (1973b), "Experimental confirmation of field access device modeling", AIP Conf. Proc. Series, vol. 18, pp. 116-120.

P.K. George and A.J. Hughes (1976a), "Bubble domain field access device modeling - Part I: the magnetization problem", IEEE Trans. Magn., vol. MAG-12, pp. 137-147.

P.K. George and A.J. Hughes (1976b), "Bubble domain field access device modeling - Part II: device modeling", IEEE Trans. Magn., vol. MAG-12, pp. 148-159.

P.K. George, A.J. Hughes and J.L. Archer (1974), "Submicron bubble domain device design", IEEE Trans. Magn., vol. MAG-10, pp. 821-824.

I.S. Gergis, P.K. George and T. Kobayashi (1976), "Gap tolerant bubble propagation circuit", IEEE Trans. Magn., vol. MAG-12, pp. 651-653.

T.N.E. Greville (1969), "Spline functions, interpolation and numerical quadrature", Mathematical Methods for Digital Computers, A. Ralston and H.S. Wilf, Eds. New York: John Wiley.

C.J. Hegedus and E. Della Torre (1977), "Efficient calculation of bubble functions", J. Apply. Phys., accepted for publication.

International Mathematics and Statistics Libraries (1977), Subroutines: IBCIEU, ICSEVU and DBCQDU, Houston, Texas.

W. Ishak (1975), "Magnetostrictive-piezoelectric detector for bubble domains", Faculty of Engineering, McMaster University, Hamilton, Canada, Report SOC-77.

W. Ishak and E. Della Torre (1976), "Algorithms for the computation of the complete and the generalized elliptical integrals of the first, second and third kinds", Faculty of Engineering, McMaster University, Hamilton, Canada, Report SOC-116.

W. Ishak and E. Della Torre (1977a), "BUBMAT - to compute various strip domain and bubble domain parameters in bubble-type materials", IEEE Trans. Magn., vol. MAG-13, pp. 964-965.

W. Ishak and E. Della Torre (1977b), "BUBMAT2 - a package for bubble material parameters calculation", Faculty of Engineering, McMaster University, Hamilton, Canada, Report SOC-181.

W. Ishak and E. Della Torre (1978a), "Nonlinear modeling of field access bubble devices", submitted to IEEE Trans. Magn.

W. Ishak and E. Della Torre (1978b), "MOFAB - A FORTRAN program for modeling of field access bubble devices", accepted for publication in IEEE Trans. Magn.

W. Ishak and E. Della Torre (1978c), "Micromagnetic modeling of submicron bubble circuits", Faculty of Engineering, McMaster University, Hamilton, Canada, Report SOC-189.

W. Ishak, W. Kinsner and E. Della Torre (1975), "Magnetostrictive-piezoelectric bubble detectors", AIP Conf. Proc. Series, vol. 24, pp. 558-559.

M.E. Jones and R.D. Enoch (1974), "An experimental investigation of potential wells and drive fields in bubble domain circuits", IEEE Trans. Magn., vol. MAG-10, pp. 832-835.

R.I. Joseph and E. Schlomann (1965), "Demagnetizing field in non-ellipsoidal bodies", J. Appl. Phys., vol. 36, pp. 1579-1593.

I. Khaiyer (1975), "Models for I and T pattern permalloy bars based upon Bitter pattern observation of domain wall movements", IEEE Trans. Magn., vol. MAG-12, pp. 114-118.

W. Kinsner (1973), private communication.

W. Kinsner (1974), "Convergence acceleration in the numerical solution of field problems", Faculty of Engineering, McMaster University, Hamilton, Canada, Report SOC-43.

W. Kinsner and E. Della Torre (1972), "Numerical calculations of three dimensional magnetic fields using SER", AIP Conf. Proc. Series, vol. 10, pp. 232-236.

W. Kinsner and E. Della Torre (1974), "Magnetostrictive-piezoelectric bubble detector", Faculty of Engineering, McMaster University, Hamilton, Canada, Report SOC-53.

W. Kinsner and E. Della Torre (1975), "Acoustic bubble detector", Faculty of Engineering, McMaster University, Hamilton, Canada, Report SOC-81.

W. Kinsner and E. Della Torre (1975), "Magnetic field distributions due to bubble propagation circuits", J. Appl. Phys., vol. 46, pp. 933-935.

G.S. Krinchik, E.E. Chepurova, U.N. Shamatov, V.K. Raev and A.K. Andreev (1975), "Magnetization reversal study in permalloy bubble-propagation circuits with magneto-optical equipment of micron resolution", AIP Conf. Proc. Series, vol. 24, pp. 649-650.

M.H. Kryder, K.Y. Ahn and J.V. Powers (1975), "Amorphous film magnetic bubble domain devices", IEEE Trans. Magn., vol. MAG-11, pp.

1145-1147.

Y.S. Lin (1972), "Analysis of permalloy circuits for bubble domain propagation", IEEE Trans. Magn., vol. MAG-8, pp. 375-377.

H. Ma (1976), "Magnetostatic fields in thin film permalloy bar arrays". Ph.D. Dissertation, University of Florida, Gainesville, Florida.

T.J. Nelson, Y.S. Chen and J.E. Geusic (1973), "Field nucleation of magnetic bubbles", IEEE Trans. Magn., vol. MAG-9, pp. 289-293.

J.W. Nielsen (1971), "Properties and preparation of magnetic materials for bubble domains", Metallurgical Trans., vol. 2, pp. 625-633.

T.H. O'Dell (1974), Magnetic Bubbles. London: Macmillan.

I.B. Ortenburger (1977), private communications, November.

I.B. Ortenburger, R.W. Cole and R.I. Potter (1977), "Improvements to a self-consistent model for the magnetic recording properties of non-particulate media", IEEE Trans. Magn., vol. MAG-13, pp. 1278-1283.

F. Parzefall, B. Littwin and W. Metzdorf (1973), "X-bar, a new propagation pattern for magnetic bubbles", IEEE Trans. Magn., vol. MAG-9, pp. 293-297.

A.J. Perneski (1969), "Propagation of cylindrical magnetic domains in orthoferrites", IEEE Trans. Magn., vol. MAG-5, pp. 554-557.

A.B. Smith (1974), Bubble-Domain Memory Devices. Dedham, Mass.: Artech House.

W. Strauss (1971), "Detection of cylindrical magnetic domains", J. Appl. Phys., vol. 42, pp. 1251-1257.

W. Strauss and G.E. Smith (1970), "Hall-effect domain detector", J. Appl. Phys., vol. 41, pp. 1169-1170.

A.A. Thiele (1969), "The theory of cylindrical magnetic domains", BSTJ, vol. 48, pp. 3287-3335.

J.H. Wilkinson (1963), Rounding Errors in Algebraic Processes. Englewood Cliffs, N.J.: Prentice-Hall.

AUTHOR INDEX

H.L. Abdel-Malek	4, 106, 107
K.Y. Ahn	xii, 4, 95, 110
G.S. Almasi	13, 25, 35, 66, 74, 102
A.K. Andreev	49, 134
J.L. Archer	24, 25, 67, 87, 112
A.M. Balbashov	23
J.W. Bandler	4, 106, 107, 109
S.L. Blank	10
A.H. Bobeck	ix, 2, 6, 7, 9, 11, 23, 120
P.I. Bonyhard	ix, xii, 2, 9, 14, 80, 83
M.A. Boyarchenkov	23
W.F. Brown, Jr.	32, 33, 128
R. Bulirsch	38
M. Casey	49, 134
H. Chang	2, 4, 6, 7, 14, 66
C. Charalambous	109
P. Chaudhari	10
T.T. Chen	24
Y.S. Chen	ix, xii, 11, 14, 83
E.E. Chepurova	49, 134
A.Y. Chervonenkis	23
M.S. Cohen	30, 32, 35
R.W. Cole	52
J.A. Copeland	23
B.D. Cullity	21, 35, 49, 128, 132
J.J. Cuomo	10

AUTHOR INDEX (continued)

I. Danylchuk	ix, 2
W.J. DeBonte	88, 117
E. Della Torre	ix, 2, 6, 7, 11, 13, 15, 21, 24, 31, 38, 40, 45, 50, 57, 74, 87, 88, 90, 120, 121
J.W.F. Dorleijn	38
D.B. Dove	24, 25
W.D. Doyle	49, 134
W.F. Druyvesteyn	38
R.D. Enoch	xii, 4, 67, 68, 95, 98
J.S.Y. Feng	24
R.F. Fischer	2
W. Fleming	64
R. Fletcher	109
R.J. Gambino	10
P.K. George	x, xi, xiii, 2, 24, 25, 47, 55, 57, 60, 64, 65, 66, 67, 70, 71, 87, 112
I.S. Gergis	2
J.E. Geusic	ix, 9, 11
T.N.E. Greville	123
C. Hegedus	90
E. Huijer	24, 25
A.J. Hughes	x, xi, xiii, 25, 47, 55, 57, 60, 64, 65, 66, 70, 71, 112
W. Ishak	ix, 13, 38, 45, 50, 57, 74, 87, 88

AUTHOR INDEX (continued)

M.E. Jones	xii, 4, 67, 68, 95, 98
R.I. Joseph	124
G.E. Keefe	13
I. Khaiyer	ix, 23
W. Kinsner	ix, 2, 13, 15, 21, 24, 67, 68
T. Kobayashi	2
G.S. Krinchik	49, 134
M.H. Kryder	xii, 4, 95, 110
Y.S. Lin	13, 23, 25, 36, 66, 74, 102
C.V. Longo	21, 31, 40, 121
B. Littwin	2
H. Ma	24, 25, 49, 52, 134
W. Metzdorf	2
E. Munro	25
T.J. Nelson	ix, 11
J.W. Nielsen	10
T.H. O'Dell	2, 6
I.B. Ortenburger	52
F. Parzefall	2
A.J. Perneski	ix, 2, 11
R.I. Potter	52
J.V. Powers	xii, 4, 95, 110
V.K. Raev	23, 49, 134

AUTHOR INDEX (continued)

M.I. Samarin	23
E. Schlomann	124
U.N. Shamatov	49, 134
D. Sinha	4, 109
M. Slusarczuk	25
A.B. Smith	2, 6
G.E. Smith	11
J.L. Smith	ix, xii, 2, 14, 80, 83
W. Strauss	ix, 11, 13
A.A. Thiele	9, 67, 86, 88, 89, 94, 101, 117
D.A. Thompson	13, 24
D.L.A. Tjaden	38
L.R. Tocci	24
J.K. Watson	24, 25
J.H. Wilkinson	25

SUBJECT INDEX

Acoustic-magnetostrictive detector, 13

Amorphous films, 10, 110

Anisotropy

- energy constants, 31, 33
- magnetocrystalline, 30, 31
- megnetoelastic, 30, 32
- shape, 31
- uniaxial, 32

Annealing, 11

Annihilation, 11, 14

Base points, 106, 107, 108

Bias field, 1, 8, 9, 28, 86, 87, 94

- margins, 3

Bubble

- annihilation, 11, 14
- aspect ratio, 89
- circuit analysis, 66, 68
- collapse field, 88, 91, 98
- detection, 11, 12, 13
- generation, 11
- mobility, 9, 10
- lattice file, 10
- materials, 7
- parameters, 7, 8, 102, 103
- propagation, 15, 17

SUBJECT INDEX (continued)

Bubble (continued)
- size fluctuations, 66, 83, 88
- stability, 88
- stray field, 28
- velocity, 101, 102, 115

Characteristic length, 9, 80

Chevron circuits, 74
- asymmetric, 74, 75
- symmetric, 74, 76

Coercivity
- bubble, 101
- permalloy, 134

Constraints, 100, 105, 109

Continuum models, 1, 23

Critical points, 3, 102

Demagnetizing
- energy, 30, 31
- factors, 54, 55, 121, 127
- field, 30, 31, 34, 35, 37, 40, 41, 54, 59

Deposition field, 47

Detection
- acoustic-magnetostrictive, 13
- Hall-effect, 11, 12
- magnetoresistive, 13
- magnetostrictive-piezoelectric, 12, 13

SUBJECT INDEX (continued)

Domain
closure, 21, 22
models, 1, 21
wall, 21

Energy
anisotropy, 30
magnetocrystalline, 30, 31, 33
magnetoelastic, 30, 32
shape, 31
applied field, 30
exchange, 30, 32
demagnetizing, 30, 31
minimization, 30

Epitaxial films, 10

Exchange
constants, 9, 32, 128
energy, 30, 32
field, 34, 35

Ferromagnetic films
magnetostrictive, 12, 13
nonmagnetostrictive, 19
permalloy, 19, 23

Field access circuits, 2

Force function, 90

Fourier series expansions, 24, 25

Gap tolerant circuits, 5, 15

SUBJECT INDEX (continued)

Garnets, 9

gadolinium galium, 10

Generation

disk, 11

nucleation, 11

Half-disk circuits, 77-82

Hall-effect detectors, 11, 12

Magnetization

algorithm, 50

distributions, 30

saturation, 7, 19

Magnetocrystalline anistropy (see Anisotropy)

Magnetoelastic anisotropy (see Anisotropy)

Magnetoresistance (see Detection)

Magnetostriction (see Detection)

M-H approximations, 132-137

Micromagnetic

algorithm, 43

models, 19

Minimax objective, 109

Nondestructive read-out, 11

SUBJECT INDEX (continued)

Optimization
    bubble circuits, 9, 100-116
    procedure, 110

Over-relaxation factor, 93

Permalloy (see Ferromagnetic films)

Polynomial approximation, 100, 106, 107

Potential well, 66, 67
    depth, 67
    distributions, 68

Propagation
    field access, 2
    circuits, 15, 17
        asymmetric chevrons, 2, 74-76
        asymmetric half-disks, 2, 77-83
        channel-bars, 2
        gap tolerant, 2
        parallel-bars, 2
        optimization, 5, 100-116
        T-I, 2, 95-97
        symmetric chevrons, 2, 74-76
        symmetric half-disks, 2, 77-83
        Y-I, 2
    track, 101

Quality factor, 9

Replicators, 5, 14
    sideways, 14, 83-85

Stability functions, 90

SUBJECT INDEX (continued)

Susceptibility, 132

Under-relaxation factor, 44, 45, 51-53

Uniaxial anisotropy (see Anisotropy)